A New Digital Data Acquisition System for Neutron Metrology

Chloé Sole

Master of Science
Department of Physics
University of Cape Town
2022

Abstract

Within the neutron metrology and spectrometry community digital pulse processing systems are being developed for measurements of Fast neutron fields in a wide variety of contexts, for example at accelerator and medical radiation facilities, around nuclear power plants, in airplanes in flight and space stations. These fields often vary widely with respect to both energy and intensity, which complicates measurements of energy dependent fluence.

Investigations have been completed into the suitability of a CAEN DT5730 digitiser unit as a viable alternative to a traditional analogue system for data acquisition for fast neutron metrology. Experiments were completed at the fast neutron facilities of AMANDE (IRSN, Cadarache) using a BC501A scintillation detector and both the DT5730 digitiser and an analogue system based on NIM electronics and an MPA-3 multichannel analyser acquisition unit. Follow-up measurements were made at the n-lab facility at the University of Cape Town. The measurements covered an energy range from 0.5 MeV to 20 MeV, over a large range of intensities. The energy and intensity response for both systems and digital configurations were investigated based on the unfolding of measured light output spectra using an existing neutron response matrix for the detectors. Dead-time behaviour, rate dependent losses and linearity over the energy range were explored. The quality of the measured neutron spectra was compared through both uncertainty budgets and shape comparison analyses.

Factors to consider when migrating from analogue signal processing to digital signal processing are discussed for the measured energy and intensity range, including advantages and disadvantages using digital pulse processing for metrology both in the laboratory and in the field.
While there is more research required for a thorough bench-marking, the present results indicate that digital data acquisition technology has matured to the point where it can now be considered for use within neutron metrology.

Acknowledgements

Firstly, I'd like to thank my supervisors Andy Buffler, Tanya Hutton and Tom Leadbeater for their continued support and guidance throughout my masters. Further I would like to thank Vincent Gressier and the staff of the IRSN AMANDE facility in France for their wonderful hospitality and support during the measurement campaign in April 2019 and for hosting me for three months. A special thanks to Richard Babut from the IRSN for making me feel like an integral part of the team and ensuring my happiness during my stay.

Many thanks to the IRSN and NRF for the funding support of this research as well as the additional financial support from UCT Physics.

Thanks to my friends and family who supported me through the ups and downs during this time. Thanks to my parents for their unconditional love and support, my sisters for all the late night calls.

Table of Contents

1. Introduction

1.1 Neutron Metrology

Metrology is the science of measurement, and fundamentally has as its focus the activity of counting with reference to a set of standards. Neutron metrology may be understood as the process of counting free neutrons, with the two main quantities of interest being the number of neutrons (either crossing a region of interest or emitted by a source), and the energy distribution of the counted neutrons. The measurement result is often presented as a fluence rate (number of neutrons per unit of surface per unit of time), which can further be presented as a function of the neutron energy. This process is often complicated by the measured fluence distribution as a function of energy being influenced by the directionality of the neutron source [1].

Neutron fields of interest can vary widely with respect to context, energy and fluence [2], with each of these aspects introducing an additional degree of complexity. The energy of neutron fields can range from cold neutrons produced at some facilities, below the meV range, to very high energy (on the order of GeV) neutrons produced in accelerator facilities or by cosmic rays interacting with the atmosphere. Similarly, the possible intensities span from a few neutrons cm^{-2} s^{-1} to 10^{15} neutrons cm^{-2} s^{-1} occurring at the core of high intensity nuclear fission reactors.

The distributions of the neutron fluence per logarithmic energy interval (fluence per unit lethargy) for moderated fission neutrons and cosmic rays can be seen in figure 1.1 [1]. In this figure, fluence in a specific energy region is calculated as the area under the curve within that region. Neutrons produced as products of fission have a maximum energy limit of around 10 MeV, while the energy of neutrons produced in the atmosphere by cosmic rays can extend above 10 GeV. Fusion reactions such as those in a D-T neutron generator can reach up to 20 MeV in neutron energy.

The ways in which neutrons are detected vary greatly with energy and intensity. Neutron interaction cross-sections are highly dependent on the material type and the energy of the irradiating neutrons [3, 4]. On the higher end of the intensity range, detecting individual neutron events becomes more difficult and estimating the number of neutrons interacting with the material often relies on a calculation rather than direct measurement [1].

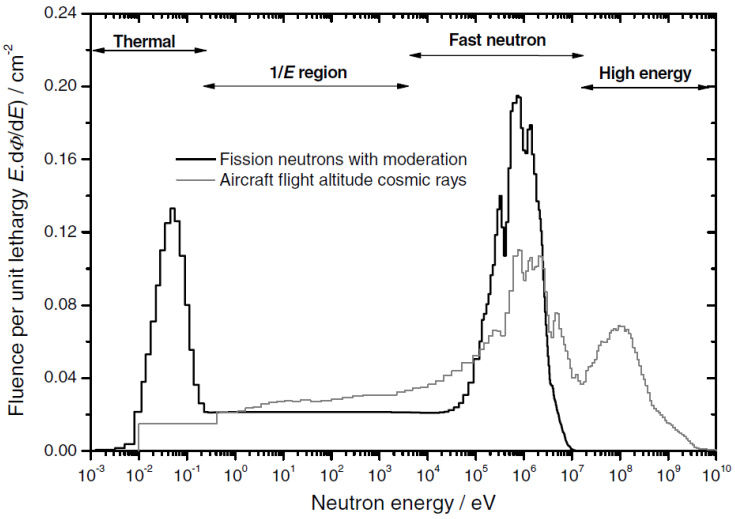

Figure 1.1: Distributions of fluence per unit lethargy for two neutron fields (fission neutrons with moderation, and neutrons produced at flight altitude by cosmic rays) [1].

Detectors deployed for neutron metrology have traceability to the interaction cross-sections of relevance which provide the reference standards for each detector type, which in turn underpin the response of the detector when exposed to different neutron fields. A detector response function is defined as being the output of the detector when exposed to a mono-energetic neutron field [5]. Response functions can either be measured directly or simulated through standard Monte Carlo codes, such as NRESP [6] or MCNP [7].

The fast-neutron region requires the greatest number of reference standards [1]. This energy region is responsible for neutrons produced from many different reactions, including the neutrons produced from D-D and D-T fusion reactions. With the present interest in fusion as an energy source this energy range and its neutrons are increasingly more important [8–11].

The detectors typically used in the field of fast neutron metrology are reliant on neutron induced reactions, such as n-p elastic scattering and fast fission, while capture reactions are used for detection of thermal or moderated fast neutrons. These interactions produce secondary charged particles which then can be used to determine information about the neutrons incident on the detector. Most neutron fields measured will be coupled with a gamma-ray field introducing another consideration when designing these detection systems: either the detector needs to be unable to detect gamma-rays due to the medium or detection technique used, or the detector needs to have a difference in the response to the different radiation types interacting with the detection medium [5].

There are two main broad measurement technique categories, the one being a direct measurement and the other being a measurement of the neutron flight time over a known distance. The direct measurement requires a very well characterised set of response functions for the detector and relies on convolving the response functions to fit the measurement to determine the fluence distribution

as a function of energy, commonly completed through unfolding analyses (appendix A). Time-of-flight (ToF) measurements require a pulsed beam, of the order of nanoseconds, and are typically used for detector characterisation and the empirical determination of the response functions for the detector. The measured or calculated response functions then allow for neutron metrology measurements to be made for unknown fields, within or outside of a laboratory environment.

For measurements without time-of-flight information the ability to differentiate between the gamma-ray induced events and the neutron events (pulse shape discrimination, section 2.2) is crucial for neutron metrology. The detectors typically used for their pulse shape discrimination (PSD) capabilities are organic scintillators, though recent developments have seen PSD capabilities in doped plastic scintillators [12]. Organic liquid scintillators are well characterised within the fast neutron range and specifically the hydrocarbon-based liquid are the preferred type of detector due to their high efficiency, fast response, excellent energy resolution, and dependence on the very well-known n-p elastic scattering cross section [5]. The response functions for this detector can be reliably calculated by a number of codes which require only the resolution function of the detector.

Several metrology laboratories around the world (IRSN, PTB, NPL, iThemba LABS, etc.) use a BC501A organic liquid scintillator coupled to an analogue pulse processing acquisition system as the reference system for in-laboratory fast neutron metrology. The analogue acquisition systems in these reference systems are based on NIM-standard pulse processing modules, analogue-to-digital converters (ADCs) and multi-parameter analyser (MPA). These systems are expensive and difficult to use outside of the laboratory.

The advent of digital data acquisition systems (dDAQs) for nuclear radiation measurements brought several new approaches to the acquisition and analysis of data. The systems used in the community vary from digitization of the raw anode pulse, after a pre-amplifier [13] to later in the analogue electronics chain such as after an amplifier. Early digitisation of the waveforms have introduced the ability to optimise analysis and the flexibility to extract more information from a single data set with simple digital signal analysis.

1.2 Digital Data Acquisition Systems

There is a large range of accessible digitisers for nuclear physics applications produced by several manufacturers, such as CAEN [14], XIA [15], NI PXI's [16] and Teledyne SP devices [17]. The capabilities of such digitisers range from 10 bit resolution at 4 Gs/s for a maximum of 2 channels to 14 bit resolution at 500 Ms/s for up to 16 channels. Generally the increased bit resolution results in a decrease in sampling rate. The large variety in the technical capabilities of the digitisers on the market make them versatile for many in-field or in-laboratory applications, as demonstrated in the examples presented below.

On the software side, there is available proprietary software available for the commercial digitisers, additionally the libraries used to communicate with the digitiser are also available making it possible to develop customised data acquisition software. The software is responsible for the programmable triggering schemes and certain parameters that cannot be adapted post processing, like the number of samples which constitute one event. Furthermore, the software used for post acquisition analysis can affect produced results through factors like the timing resolution of a digital constant fraction discriminator (CFD), pulse pile up handling and pulse height saturation. Examples of custom software developed using different bases such as LabVIEW and ROOT can be found in references [18] and [19].

There is a significant movement from analogue DAQs to digital DAQs across a large variety of contexts, despite this there is little to no literature on dDAQs specifically within the context of neutron metrology. Several data acquisition systems, for neutron measurements, are based on early digitisation immediately at the anode output, with applications ranging from fusion diagnostics, to cross-section measurements.

The dDAQs developed for fusion diagnostics include systems based on custom designed digital systems [8, 18, 20–22] and off-the-shelf digital solutions such as PXI modules [11, 16]. These systems need to manage extremely high intensity measurements and since digital systems acquire events with no dead time (if the buffer size is appropriate) a dDAQs is preferred in these applications. The neutron spectrometer for the Joint European Torus (JET) [8, 21, 22] is a EJ-301 (NE213) organic liquid scintillator coupled with a custom ENEA [20] developed dDAQ based on two ADCs interleaved to obtain a sampling rate of 200 Ms/s with 14-bit resolution for a 2.8 V input range. The ADCs are controlled by an field programmable gate array (FPGA). The dDAQ is programmable through custom-developed LabVIEW [18] set up to have a dynamic acquisition window, minimising data rates and buffer saturation. The dDAQ developed for JET not only provided better acquisition rate performance to its predecessor, it allowed for the addition of PSD measurements where the analogue DAQ only provided discrimination through time-of-flight.

Several systems have been developed as a dedicated detection setup for improving neutron cross-section measurements. A system based on four dDAQ AP-240 [23] boards with custom C++ software, coupled with an array of EJ-301 detectors are used for neutron scattering measurements at RPI LINAC [24]. At CERN's neutron Time-of-Flight facility (n_TOF) [25] a general purpose data acquisition system was developed for neutron cross section measurement for sub-critical reactor studies. In this case large neutron fluxes are expected and due to the large number of expected pile up events the data acquisition system was designed to mitigate these affects. The dDAQ is based on fast flash ADC's to digitise and on-board store the full waveform for each channel and beam burst. The ADC modules used are the DC270 and DC240 8 bit resolution Acqiris digitisers, with sampling rates up to 1 and 2 Gs/s respectively.

A similar dDAQ used coupled with the Detector for Advanced Neutron Capture Experiments (DANCE) [26] at Los Alamos Neutron Science Center (LANSCE), but using an on-board computer controlling 24 digitisers executing waveform analysis in order to only store the timing information and peak area.

Digital DAQs have been implemented within the context of nuclear material identification for security reasons [27, 28]. Within the context of identification of shielded neutron sources, a BC501A liquid scintillator detector was used coupled to a 1-GHz digital oscilloscope Tektronix TDS-5104 which digitised the raw waveforms to be processed post-acquisition [27]. Measurement of prompt neutrons from photofission have been demonstrated to be useful for actinide detection [29]. The measurements were made using phenylxylylethane (PXE) liquid scintillator detectors whose raw signals were digitised using a 12-bit digitiser and then analysed digitally. A Medipix (CMOS pixel detector) imaging detector has also been repurposed for neutron detection and can be used in the context of security measurements [30].

A low budget dDAQ can be created simply using low cost oscilloscopes [31, 32]. A comparison was carried out between two CAEN digitisers and two low cost oscilloscopes. The CAEN digitisers produced better results for a neutron spectroscopy measurement due to better timing resolution and PSD quality. One of the oscilloscopes had an equivalent energy resolution to the digitisers, showing for a low budget experiment a low cost oscilloscope with custom analysis software can be used for a dDAQ [31].

In the context of space weather, a neutron monitor network [33] is extremely useful in the detection of secondary or tertiary neutrons produced by relativistic cosmic rays interacting with the earths atmosphere. These measurements are the basis to forecasting space weather and the potential prediction of super storms which can cause considerable damage to infrastructure on the earth. To further increase the accessibility of detectors able to contribute to this network a mini-neutron monitor [34] has been developed consisting of an outer thick cylindrical tube of polyethylene reflector layer surrounding a smaller cylinder of lead with a smaller core of neutron moderator in the centre. This is then coupled to a BF_3 tube which is supplied with a low current high voltage power supply. Post a pre-amplifier, the raw pulses are digitized using a PIC32 micro-controller which is then processed and stored using a Raspberry Pi [35].

Digital data acquisition systems provide several advantages over the standard analogue electronics; zero dead time acquisition with appropriate buffer sizes, compact, increasing technological support, greater control over the analysis of the raw traces allowing for more analysis parameters to be extracted easily, cheaper and very easily applied to a large range of contexts [36]. The wide range of applications where dDAQs are already being used calls for metrology standards to be developed for them.

1.3 Key objectives of Present Work

This thesis presents progress towards the development of a new digital data acquisition system for fast neutron metrology. The equivalence of analogue and digitally produced parameters are explored and the uncertainties around the different systems and configurations are presented.

- Make measurements at the IRSN AMANDE facility using a BC501A scintillation detector coupled to the reference standard analogue and new digital based acquisition system for neutron fields with energies between 0.5 MeV and 20.0 MeV and intensities between 10^3 cm^{-2} s^{-1} and 10^4 cm^{-2} s^{-1}.
- Investigate the equivalence of the analogue and digital pulse shape (S) and light output (L) parameters.
- Use unfolding techniques to investigate the energy and intensity response of both systems.
- Determine dead-time behaviour along with rate dependent losses and linearity across the energies and intensities measured.
- Compare the measurements made with the two acquisition systems through a shape analysis.
- Determine an uncertainty budget for the two acquisition systems for measurements without time-of-flight information.

The structure of this thesis has been adjusted to suit the presentation of the data. The methods and facilities used are presented with the associated data for readability.

2. Fast Neutron Spectroscopy

This chapter discusses the physics which underpins neutron metrology, with a focus on measurement techniques with organic scintillator detectors.

2.1 Neutron Detection with Liquid Scintillators

Neutrons are chargeless and thus cannot interact through the Coulomb force and will only interact with a medium through its nuclei. Interactions between neutrons and matter produce heavy charged particles by neutron absorption and subsequent emission of p, α and others, and recoil of the target nucleus after a collision with a neutron [37].

The way a neutron interacts with atoms within a medium strongly depends on the energy of the neutron and the composition of the medium. Detectors developed for specific radiation fields need to be designed taking advantage of the interactions with neutrons of the desired energy.

The probability of a specific interaction occurring between a fixed energy neutron and a volume is constant per unit volume, represented by the macroscopic cross-section (Σ). This is specific to the number of nuclei per unit length and the microscopic cross-section. The microscopic cross-section (σ) is presented in units of area (barn $= 10^{-28}\text{m}^2$) and can be interpreted as the effective target area within which an interaction will occur. This quantity is specific to the neutron energy and the target nucleus. For a given interaction, Σ is then related to σ through the following relation:

$$\Sigma(E) = N\sigma(E), \tag{2.1}$$

where N is the number of nuclei per unit volume. These quantities are responsible for the way neutrons of given energies interact with nuclei and the resultant products produced from the interaction. Detectors are developed to make use of specific interactions through the changing likelihoods of the different interactions with energy and target nuclei.

The main interaction utilised for fast neutron ($E_n > 1$ keV) detection is elastic scattering [38]. The secondary radiation, in this case, are the recoiling nuclei.

The amount of energy transferred to the recoil nucleus (E_R) is dependent on the mass of the target nucleus (A), the scattering angle of the neutron in the centre of mass reference frame (Θ) and the kinetic energy of the incident neutron (E_n) [39], see equation 2.2. Complete energy transfer from a neutron can occur with hydrogen ($A = 1$), resulting in a recoil proton. For this reason light elements are preferable for detectors reliant on elastic scattering for neutron detection.

$$E_R = \frac{2A}{(1+A)^2}(1-\cos\Theta)E_n \tag{2.2}$$

Through each neutron scatter in the medium, the kinetic energy of the neutron is moderated until the full energy is deposited in the medium, the neutron is captured or the neutron escapes with a portion of its kinetic energy remaining. Inelastic scattering can occur if the energy of the incident neutrons is high enough, reducing the kinetic energy of the neutron by a greater proportion than the equivalent elastic scattering interaction.

2.1.1 Liquid Scintillator Detectors

There are several types of detectors used for fast neutron detection, broadly grouped into: detection through moderation, fast neutron-induced reactions and fast neutron scattering [37]. The most common detectors for fast neutrons are those reliant on elastic scattering.

Scintillator detectors are widely used for neutron detection for energies above 1 keV [38]. The organic liquid scintillators such as BC501A and EJ-301 are popular detectors due to their excellent timing resolution, energy resolution, high efficiency and pulse shape discrimination abilities. Many metrology institutes around the world (such as IRSN, PTB and iThemba LABS) include a standardized measurement system consisting of a BC501A organic liquid scintillator and a series of analogue NIM signal processing units. The response of these detector systems have been well characterised over a large range of energies for both neutron and gamma-ray radiation.

When radiation interacts in scintillator detectors, such as the BC501A detector used in this work, charged particles are produced which ionise the detection medium to produce scintillation photons which are then subsequently converted into an electrical pulse through a photomultiplier tube (PMT). These detectors are often sensitive to both neutron and gamma-ray interactions and therefore require additional techniques in order to separate out the events considered important for a measurement of neutron fluence and energy. It is important to understand how the different types of radiation interact with a detector in order to differentiate between the neutron and gamma-ray induced events and to understand the shape of the detectors response to the different types of sources over a range of energies.

For gamma-rays, the incident photons deposit energy in the detector through Compton scattering from electrons. The energy deposited in the detector (ΔE) can then be determined by the energy of the incident photons, as indicated in equation 2.3 [40].

$$\Delta E = E_\gamma \left[1 - \frac{1}{1 + (E_\gamma / m_e c^2)(1 - \cos\theta)} \right], \tag{2.3}$$

where E_γ is the energy of the incident photon, the angle by which the photon was scattered off the incident path θ, m_e is the mass of the electron and c being the speed of light. The maximum fraction of energy deposited is then for a scattering angle of 180°.

In the case of the incident photons having an energy exceeding that of double the rest mass of the electron production of an electron-positron pair, with the excess energy of the photon being shared between the pair as additional kinetic energy. This process requires the Coulomb field of an atom to be present and only becomes a significant process at high energies (above 10 MeV). With the electron-positron pair, the positron annihilates shortly after production resulting in two annihilation photons [41].

The photoelectric cross-section is proportional to Z^{4-5} [42] cross-section dependent, where Z is the atomic number, so the probability of full energy deposition is low since organic liquid scintillators are predominantly $Z = 1$.

For incident fast neutrons, the primary interaction in organic liquid scintillators is elastic scattering with the hydrogen in the detector [39]. Organic scintillators typically are comprised of hydrocarbon chains making them desirable for fast neutron detection via elastic scattering. Through elastic scattering with a hydrogen atom the neutrons impart a fraction of their energy to the proton.

Considering the kinetics of an elastic scatter between a neutron and proton in the centre-of-mass frame, figure 2.1, the energy of the scattered neutron and recoil proton must sum to the kinetic energy of the incoming neutron. The recoil proton can therefore have any kinetic energy from zero to the total energy of the incident neutron prior to the collision, as shown by equation 2.2.

The energy distribution of the recoil proton is continuous within the bounds of zero to the maximum defined in equation 2.2 since there are no angles which are not possible. To determine this distribution consider the probability that a neutron will be scattered with a given scattering angle Θ in the centre-of-mass frame ($P(\Theta)d\Theta$). This probability is defined by the differential cross-section ($\sigma(\Theta)$) and the total cross-section for scattering interactions (σ_s), in the form:

$$P(\Theta)d\Theta = 2\pi \sin\Theta d\Theta \frac{\sigma(\Theta)}{\sigma_s}. \tag{2.4}$$

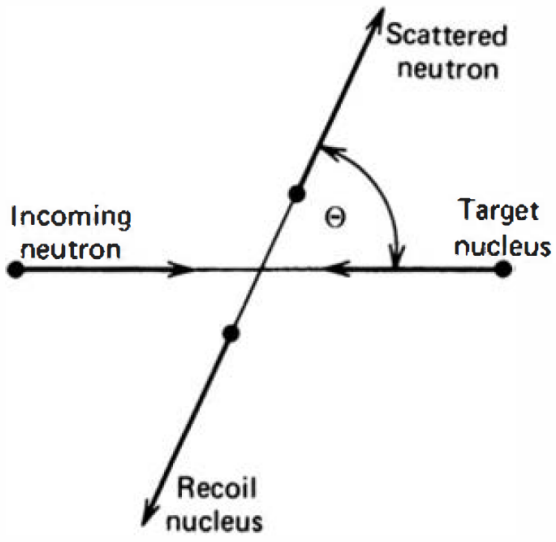

Figure 2.1: Diagram for neutron elastic scattering in the centre-of-mass frame with scattering angle Θ [39].

The probability that a neutron will be scattered with a given scattering angle Θ is equivalent to the probability of a recoil proton being created with energy dE_R at all the possible energies E_R, hence equation 2.4 can be rewritten as:

$$P(E_R) = 2\pi \sin\Theta \frac{\sigma(\Theta)}{\sigma_s} \frac{d\Theta}{dE_R}. \tag{2.5}$$

Using the expression in equation 2.2, $d\Theta/dE_R$ can be written as:

$$P(E_R) = \frac{(1+A)^2}{A} \frac{\sigma(\Theta)}{\sigma_s} \frac{\pi}{E_n}. \tag{2.6}$$

Equation 2.6 indicates that the energy distribution of the recoil protons takes the form of the differential cross-section which may have angular dependence. In the case of hydrogen, $\sigma(\Theta)$ is constant for all Θ which results in a simple continuous rectangular distribution. The response function for a detector reliant on proton recoils to detect neutrons is then a rectangular distribution for a monoenergetic neutron beam.

The recoil proton then interacts with the electrons in the detector through the Coulomb force. Due to the large number of electrons the recoil proton interacts with, its path within the detector is shorter than that of a neutron and the total energy of the recoil proton is deposited within the detector [41]. Each of the excited atoms along the protons path then de-excite through electron transitions producing a scintillation.

The exact length of this path in the detector is energy dependent and at higher energies the protons have a higher chance of escaping the detector before full energy deposition.

Certain excited states of the electrons have a short decay constant (on the order of nanoseconds) which produces a prompt emission of photons in the visible spectrum. If the atom is excited into a states which has vibrational energy, this energy is lost quickly and dissipated through the neighbours, heating up the scintillator. These states result in a loss of detectable energy and quench the scintillation efficiency reducing the light output with respect to the total energy deposited in the detector. There are additional states which produce scintillations but with a slower decay constant (on the order of milliseconds) which contribute to a delayed portion of the pulse [38, 43]. There are many suggestions to the functional form of the scintillator pulses with the simplest being the summation of two exponential functions with decay constants to describe the prompt and delayed fluorescence [43, 44].

The linearity of the light response of the detector to both gamma-rays and neutrons is well-understood. The response to gamma-rays is linear with respect to energy, similarly the light output response to neutrons above 3 MeV is linear [45]. At energies below around 3 MeV the response to neutrons is non-linear, in a similar way as shown for protons, deuterons and alpha particles in figure 2.2 [46, 47] due to increased localised energy deposition resulting in interactions with the detector which do not produce scintillations (quenching interactions). The lower light output for heavy charged particles seen in figure 2.2 is due to quenching, but at higher energies the proportion of energy that is deposited at the end of the path is less prominent with regards to the total energy deposited. This was first presented by Birks where he described the light emission per unit distance along the path of an ion as being related to the specific energy loss of the ion [46].

The non-linearity in scintillator light output response is scintillator specific and encoded in the response matrix which allows the measured response to different types of radiation to be related back to a scale defined by 1 MeV of deposited energy by a fast electron being 1 MeV_{ee}. The response matrix of a detector describes the light output distribution produced by mono-energetic sources over a range of energies. This matrix can be determined through simulation or through empirical measurement, the simulated responses need to be calibrated to replicate the detectors light output resolution and scale. The measured and FLUKA simulated response of a EJ-301 detector for several neutron energies [48] can be seen in figure 2.3 showing a good agreement between measured and simulated response functions on a MeV_{ee} scale. Response matrices are made up of these response line shapes over the energy range of interest for the incident particles of interest.

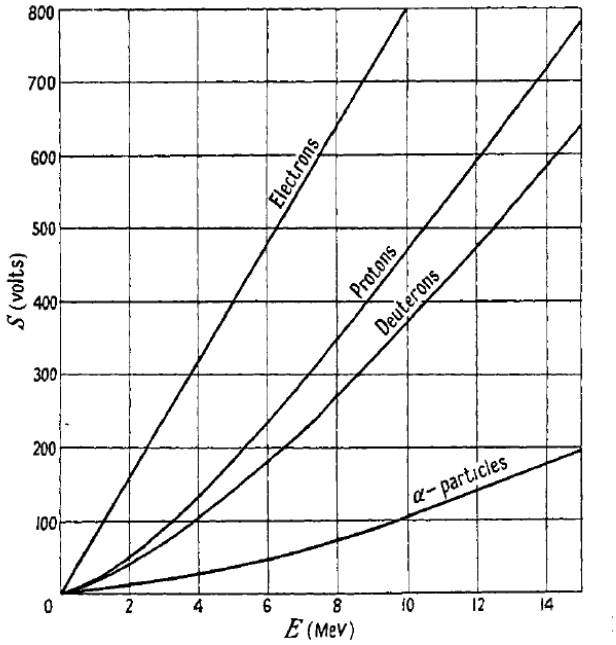

Figure 2.2: Relative light output S (volts) of anthracene to different interacting particles as a function of energy E [46, 47, 49].

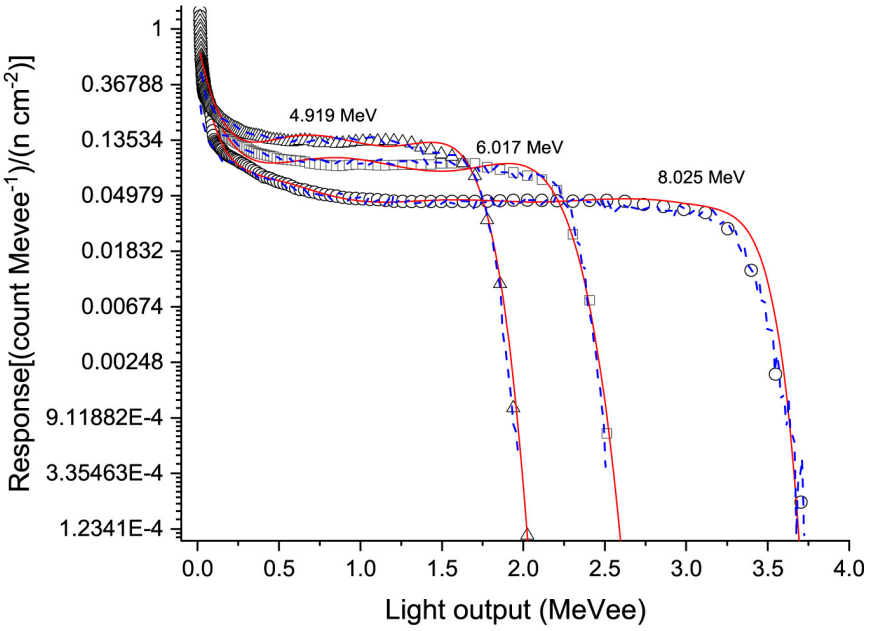

Figure 2.3: An analytical model (continuous lines), FLUKA simulated (dash), and measured response (symbol) to mono-energetic neutrons [48].

2.2 Pulse Shape Discrimination

Pulse shape characterisation of different types of radiation interacting with a scintillator detector was first developed in the 1950s [50], measuring the scintillation decay time of the excitation of electrons and alpha particles within a scintillator. The ability to measure scintillation decay time was then applied across many different scintillator detectors, such as organic liquid scintillators [38], and resulted in the development of pulse shape discrimination (PSD) techniques [51]. These techniques allowed for detectors sensitive to multiple types of radiation to separate the events induced by a specific radiation type.

As mentioned in section 2.1.1 pulses acquired from organic scintillator detectors have two decay components [38, 43, 44]. The prompt and delayed components and the underlying physics of these components are the basis for pulse shape discrimination. Different incident particles have distinct proportions of these components due to their mode of interaction with the detector.

Analogue signal processing PSD techniques commonly used are the charge comparison (CC) [43, 52] and zero crossing method (ZCM) [53–56]. The charge comparison method relies on the ratio of an integral over a short time interval to a total integral of the fast anode pulse. The zero crossing method measures the rise time of a pulse. Traditionally calculated using an analogue differentiator-integrator-integrator applied to the anode pulse. The detailed electronics for a ZCM applied to the dynode pulse are outlined in reference [53]. Figure 2.4 shows a result from early pulse shape discrimination techniques through charge comparison observed with a stilbene detector when irradiated with mono-energetic neutrons [43].

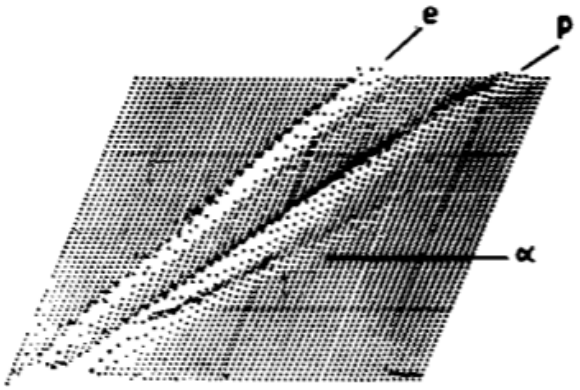

Figure 2.4: Separation of particles as measured by a stilbene detector for 15 MeV neutrons [43].

A simple PSD circuit [55] can be seen in figure 2.5, which is the underlying basis for the 2106A FAST ComTec analogue PSD module [56]. The fast anode output from the PMT undergoes RC shaping (A1) to produce a bipolar pulse, as seen in figure 2.6, after which the signal is fed to a high gain limiting amplifier (A2).

This sequence increases the quality of the ZCM as it reduces the slope of the detected pulse crossing zero. The gate (G) and strobe produced from the constant fraction trigger (CFT) of the full signal can then be delayed (D) to only allow for neutron events to produce an output pulse. The output pulses at different stages in the circuit (fig. 2.5) are detailed in figure 2.6. The pulse formation is represented by the block PF.

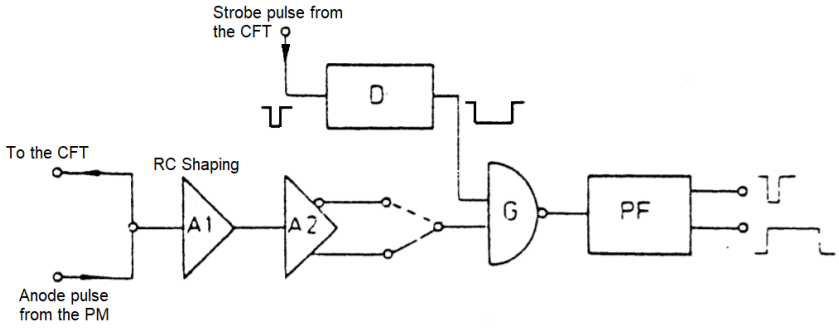

Figure 2.5: A schematic of the circuitry which form the basis for 2106a FAST ComTec analogue PSD module reliant on a ZCM [55, 56]. The RC shaping is done using a preamplifier (A1) and enhanced using a high-gain limiting amplifier (A2). The gate (G) which is controlled by the overlap in a delayed (D) strobe pulse and the signal from A2 allows for certain events to be selected for, as shown in figure 2.6. The pulse formation is represented by the block PF.

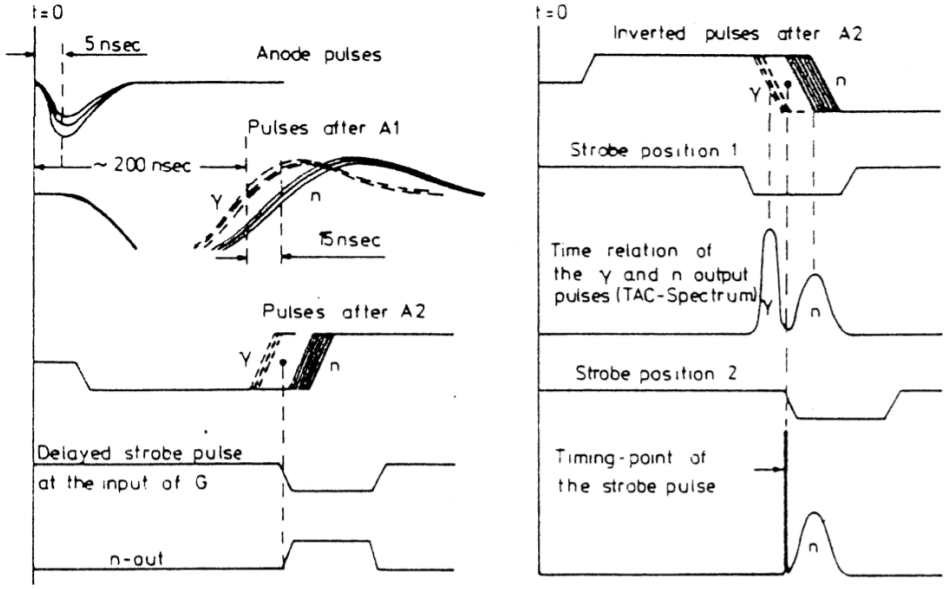

Figure 2.6: The pulses at different stages (A1 left and A2, right) of the PSD circuit outlined in figure 2.5, including the time relationships between each stage [55, 56].

The advent of digital data acquisition systems, allowing for full waveforms to be digitised in list mode, has introduced several new algorithms to analyse pulse shape. The first exploration into digital PSD included two integrating analogue-to-digital converters (ADCs) with different starting gates, allowing for a digital charge comparison (CC) to be implemented [57]. The commonly used algorithms include the digital equivalent of CC [58–60] and ZCM [61–63]. Digital CC is favoured due to the ease of implementation, small computational complexity and excellent performance [62, 63]. Although, considerations of how digitiser time and voltage resolution affect PSD quality are required to understand the consequences of choosing certain PSD methods and digitisers [59, 64].

More recently algorithms related to fitting the waveform, Fourier decomposition, gradient analysis and the Laplace transform have been implemented [44, 65–69]. Some of these algorithms are computationally expensive and would limit the data rate acquirable if implemented for live analysis, but can rather be implemented post acquisition for better low energy discrimination results [65] than CC and ZCM. Additionally, with the current machine learning explosion, there increasing interest to explore the application of machine learning to improve n-γ PSD [70, 71].

The CC method relies on measuring the relative proportions of the prompt and delayed components of the pulse. This is easily implemented on the unamplified digitized anode signals with two digital integration windows [68], with the start defined with reference to a digital CFD (see section 3.1.4) and two upper limits t_s and t_l (see section 5.1 and chapter 6). Figure 2.7 shows a sample pulse from a BC501A detector with the chosen integration bounds.

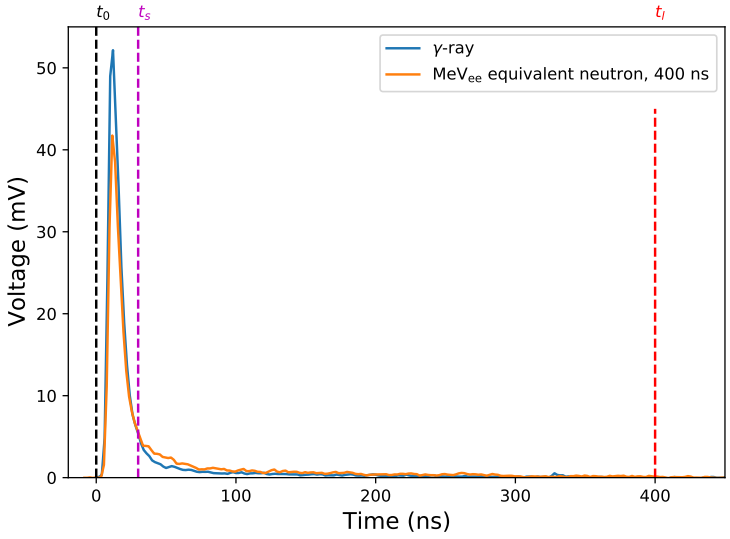

Figure 2.7: Original sample pulses for gamma-ray and neutron induced events, measured with a BC501A detector captured by the CAEN DT5730 digitiser for this thesis. The plot includes the digital integration gates (t_0, t_s and t_l) for the analysed parameters S and L.

The short integral (Q_s) and long integral (Q_l) are then used to determine the pulse shape parameter S (equation 2.7) along with the light output parameter L which is taken as equal to Q_l:

$$S = k\left(1 - \frac{Q_s}{Q_l}\right) + C, \qquad L = Q_l, \tag{2.7}$$

where k and C are scaling factors. Although the digital CC method is easy to implement and computationally inexpensive, it performs poorly at low energies ($<$0.6 MeV_{ee}) [68].

There have been a few comparisons between the digital and analogue PSD methods. For low resolution digitisers, the PSD performance was below that of the analogue ZCM [64]. In more recent work digital algorithms have been shown to produce better separation in PSD techniques [36, 63].

In the case of neutron metrology pulse shape discrimination is an important technique required to isolate the events which correspond to neutron interactions, allowing detectors to be used in mixed radiation fields. Using these techniques one can determine the measured response (light output spectrum) to gamma-rays and and neutrons separately. These light output spectra can then be used to determine the energy spectrum of the desired radiation type by a process of unfolding.

2.3 Neutron Energy Spectra

Neutron energy spectra can be obtained through two commonly used techniques. One requiring the neutron light output spectrum (unfolding) and the other relying on timing information obtained from a pulsed beam (time-of-flight).

2.3.1 Unfolding

Unfolding is the process by which a measured neutron light output spectrum is deconvolved with the mono-energetic response functions of the detector to produce an energy spectrum. The measured light output spectrum (dN/dL) can be described as a convolution of the responses of the detector to several mono-energetic sources combined as indicated by equation 2.8, where $R(L,E)$ is the response function for energy E given as a function of light output L and $S(E)$ is the energy distribution of the source [72].

$$\frac{dN}{dL} = \int R(L,E)S(E)dE \tag{2.8}$$

In order to determine the neutron energy spectrum using equation 2.8 the response matrix $R(L,E)$ need to be well defined over the measurable energy range, a default spectrum $S_{def}(E)$ to take the place of $S(E)$ and the measured neutron light output spectrum are required. The response matrix contains information about the shape and scale of detectors response to mono-energetic neutron sources. The default spectrum is an initial approximation of the energy distribution of the source, the accuracy required for this spectrum is dependent on the algorithm used to complete the unfolding process. The measured neutron light output spectrum needs to be well defined, requiring a large number of events measured, and calibrated to the scale used in the response functions. Commonly the required scale is the $\mathrm{MeV_{ee}}$ scale (1 MeV of deposited energy by a fast electron being 1 $\mathrm{MeV_{ee}}$).

There are many code packages [73], such as; UMG [74, 75], FERDOR [76], FORIST [77], RADAK [78], FLYSPEC [79] and STAY'SL [80], which implement different algorithms to determine $S(E)$ through different deconvolutional algorithms. Some of the codes rely on a least squares formalism, while others implement newer techniques such as through maximum likelihood expectation minimization (MLEM) [81]. Additionally, there are a few codes which are exploring the use of neural networks within this context [82–85].

The package *Unfolding with MAXED and GRAVEL* (UMG) produced by PTB implements a maximum entropy algorithm requiring some *a priori* information. This algorithm uses entropy to introduce a probability density which is defined over the space of all the functions defined in the response matrix [74, 75]. For the mathematics of this algorithm refer to appendix A.

The process of unfolding with the UMG package requires unfolding the spectrum with both GRAVEL and MAXED. GRAVEL is an iterative algorithm which adjusts the default spectrum to converge on a $S(E)$ which produces a neutron light output spectrum which, when compared with the supplied measured neutron light output spectrum, has the desired $\chi^2/ddof$. The choice of the desired $\chi^2/ddof$ is usually one, however in some cases the solution will over converge if this parameter is set too low. Since the solution is determined iteratively there is no closed form solution limiting the ability to do sensitivity analysis for quantifying uncertainty. Since GRAVEL is an iterative algorithm, the solution is not sensitive to the default spectrum.

MAXED is based on a maximum entropy algorithm (appendix A). This algorithm allows for the solution to be written in a closed form, allowing for uncertainty to be calculated from the sensitivity of the solution. Theoretically this solution is stable and unique, however the solution is easily affected by the choice of the default spectrum. Thus in cases where the solution is ill defined, the neutron energy spectrum calculated from unfolding with GRAVEL can be used as input for the default spectrum for MAXED.

The uncertainty propagation code used to calculate the uncertainties from the process of unfolding with MAXED is IQU and included in the UMG package. The uncertainties are calculated through the sensitivity of the solution to slight changes in the parameters. This is done through calculating the matrix $dS(E)/dS_{def}(E)$.

2.3.2 Time-Of-Flight

Neutron energy spectra are also obtainable through event time information [86]. This method requires a ns-pulsed beam to define start (or stop) times. The time-of-flight parameter T is then defined as the time difference between when the neutron production at the target (t_{start}) and the time at which an event occurs in the detector ($t_{n/\gamma}$).

The flight time for a neutron (t_n) can be expressed as:

$$t_n = \frac{d}{\beta c}, \tag{2.9}$$

where d is the distance traveled, $\beta = v/c$ with v being the velocity of the neutron and c is the speed of light. Similarly, the flight time for a gamma-ray is $t_\gamma = d/c$. Considering the difference in t_n and t_γ, β can then be expressed as:

$$\beta = \frac{d}{c(t_n - t_\gamma) + d}. \tag{2.10}$$

The measured relativistic kinetic energy of the neutron is determined through:

$$E = mc^2 \left[\frac{1}{\sqrt{1-\beta^2}} - 1 \right], \tag{2.11}$$

where m is the neutron mass [86]. Neutrons above 10 MeV are considered relativistic [87]. In the non-relativistic case, the kinetic energy of the neutron can be determined as $E = \frac{1}{2}mv^2$.

An example time-of-flight spectrum for a 2.8 MeV mono-energetic neutron field measured at 2.5 m distance from the target can be seen in figure 2.8 [86].

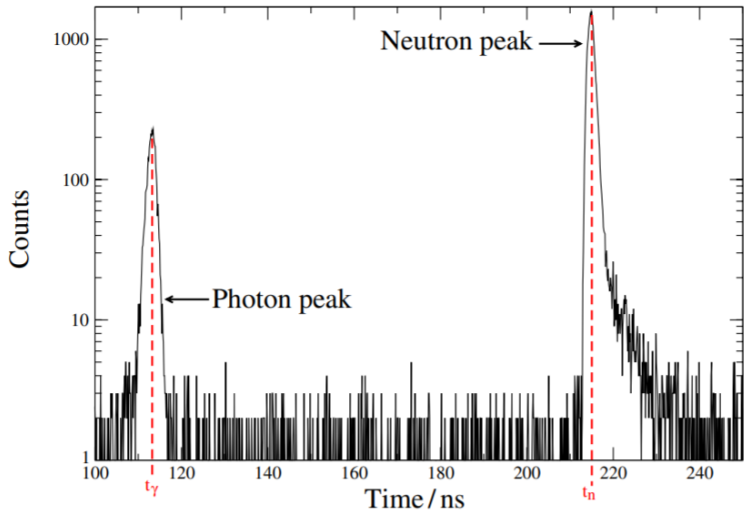

Figure 2.8: Counts as a function of time-of-flight parameter (ns) for a 2.8 MeV mono-energetic neutron field measured at 2.5 m distance from the target. The neutron and gamma-ray peaks have been indicated on the plot along with their centroid times, annotated as t_n and t_γ respectively. The difference between these two peaks is used to determine the neutron energy spectrum [86] according to eqn. 2.10 or 2.11.

3. Experimental Details

3.1 AMANDE

3.1.1 The Facility

Accelerator for Metrology and Neutron Applications for External Dosimetry (AMANDE) is a facility of the Institut de Radioprotection et de Sûreté Nucléaire (IRSN) based at Cadarche in the South of France [88] which provides monoenergetic neutron fields between 2 keV and 20 MeV [89] for metrology and calibrations of detectors. The neutrons are produced by accelerating either protons or deuterons onto deuterated and tritiated titanium targets of various thicknesses. The ions are accelerated to energies between 100 keV and 4.0 MeV using a 2 MV HVEE Tandetron [89] which operates in either a continuous (DC) or pulsed current mode with energy resolutions of < 500 eV and 4 keV respectively. Pulsed beams can be produced with frequencies between 62.50 kHz and 2.00 MHz, allowing for time-of-flight measurements.

In order to accurately measure the neutron emission rate several high efficiency neutron monitor detectors are used. For fluence measurements there are two "long counters" based on ^{3}He proportional counters inside De Pangher polyethylene shells [90, 91] (M20 and M100) placed at 6.0 m from the target at 20° and 100° relative to the ion beam. Additionally AMANDE has a current integrator (CC) which measures the charge collected on the target due to the ion beam [90]. The reference mean neutron energy is then determined through nuclear kinematics using beam characteristics in combination with the TARGET code [92], or by time-of-flight measurements with a BC501A organic liquid scintillator detector.

The 400 m^2 experimental hall (figure 3.1) was designed to minimize back-scattering and to allow for versatility and repeatability in detector positioning. Detectors can be placed between 0.5 m to 6.0 m away from the incident target within a range of $[-150°, 150°]$ relative to the incident beam line. The detector positions can be controlled remotely in the three spatial dimensions to sub-millimeter precision.

Additionally, there is a temperature and hygrometry control system to ensure the facility maintains environmental conditions as specified by international standards. These aspects result in neutron fluence and energy measurements with a relative accuracy of 3% and 1.5% respectively [93].

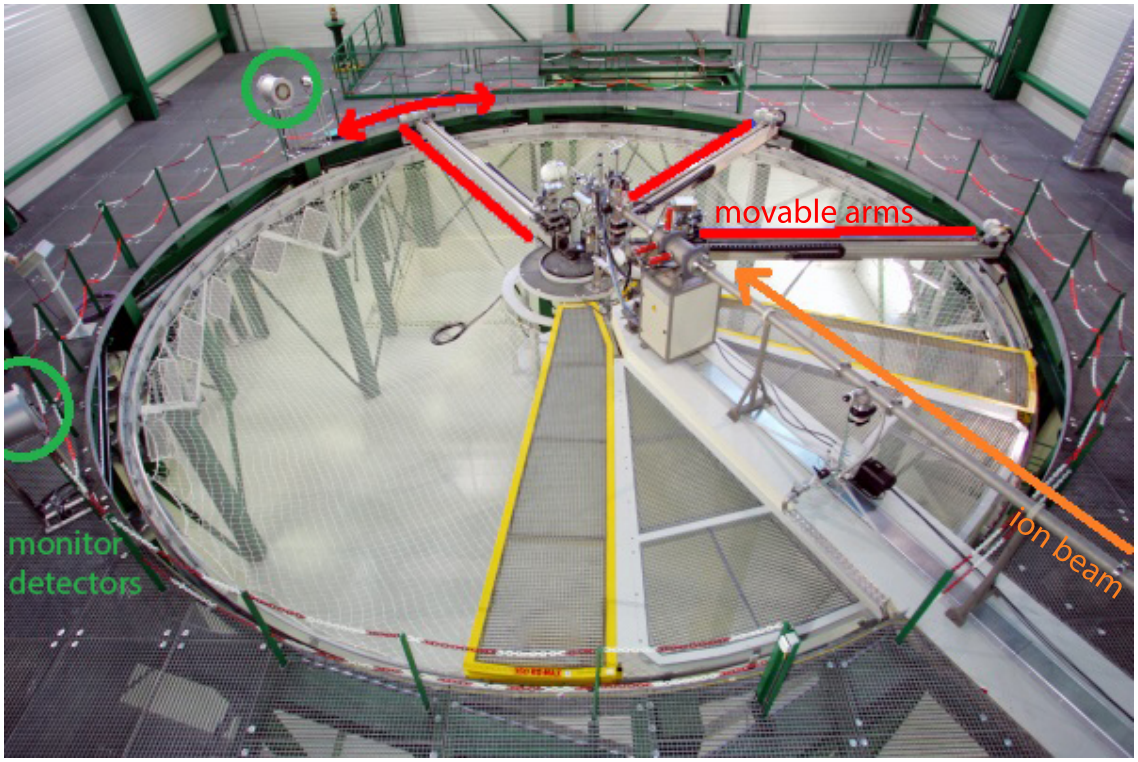

Figure 3.1: The experimental hall at AMANDE showing the three movable arms, indicated by the red lines. The beam line has been labeled in orange. The two monitor counters can also be seen on the left-hand side circled in green [94].

3.1.2 The Detector

For neutron energy and fluence measurements above 0.5 MeV the metrology standard detector used is a 2"x2" BC501A organic liquid scintillator [95] optically coupled to a XP2020 photomultiplier tube (PMT). This detector operates linearly at a high voltage (HV) of -1700 V. To ensure consistency in the detector response an internal LED is used for HV stabilization. The outputs of the detector are then directed through either the NIM-based metrology standard analogue acquisition system, or the new digital acquisition system.

The typical voltage pulses which are produced corresponding to radiation interacting with the detector (events) have peak voltages on the order of 100 mV and have durations less than 500 ns. These pulses feature a fast rise with a slow decay to the zero baseline. The decay consists of two exponential functions related to the detector chemistry and the different interaction types. Refer to chapter 2 for a thorough discussion on pulse formation and pulse shape discrimination. A digitised sample neutron and gamma-ray anode pulse can be seen in figure 3.2.

The general time dependence of this pulse is also determined by the impedance in the system, mainly associated with the PMT in series with the internal resistance combined circuitry.

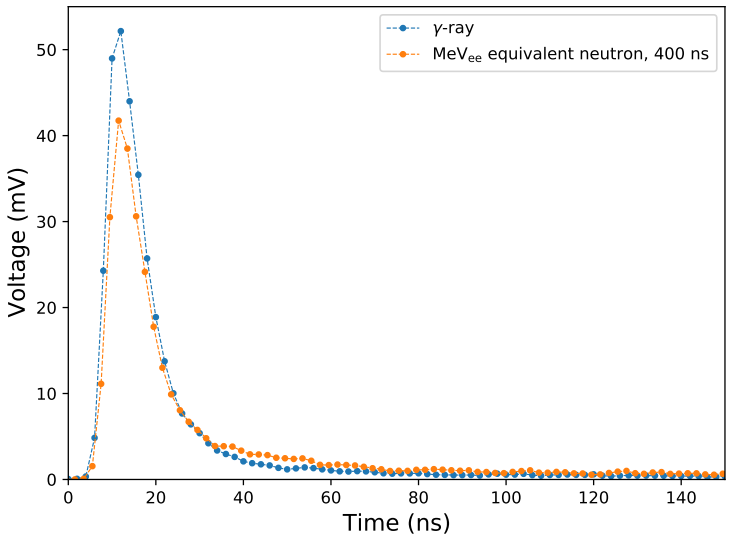

Figure 3.2: Sample pulses for gamma-ray and neutron induced events of equivalent MeV_{ee} value, measured with a BC501A detector coupled with the CAEN DT5730 digitiser. The dashed lines are only included for visual guidance.

For neutron energy spectra measured without time-of-flight information, the light output spectra need to be unfolded using a carefully calibrated set of detector response lineshapes. The response matrix describes the response of a detector to gamma-rays and neutrons over a wide energy range, and can be either determined empirically or through simulation using NRESP [6]. Figure 3.3 shows a selection of the normalised neutron response lineshapes for an energy range of 2 MeV to 20 MeV for the AMANDE BC501A detector.

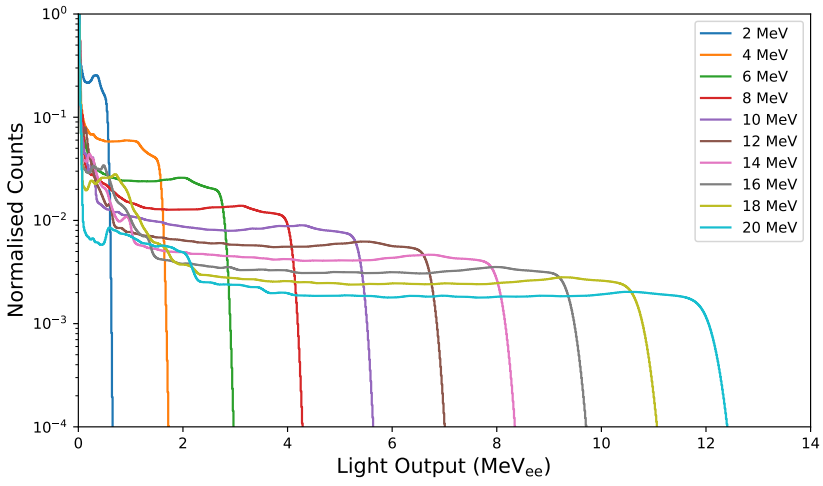

Figure 3.3: Response functions for the 2" × 2" BC501A detector produced by NRESP [6] and normalised to a fluence of 1 neutron cm^{-2} at the centre of the detector volume.

3.1.3 Analogue Pulse Processing

The neutron metrology standard acquisition system at AMANDE is a NIM-based analogue system as shown in figure 3.4. The slow output (dynode) is used to calculate the integral of the pulse for the light-output parameter (L). This is achieved by taking the pulse height of the amplified, and shaped dynode output. The pulse shape parameter (S) is determined using the zero cross over method and implemented using a FAST Comtec 2160A PSD unit [56]. Time-of-flight spectrometry requires the time interval between the rising edge of the anode pulse and a reference pulse(T) to be measured. This is typically measured using a time to amplitude converter (TAC) this is applied to the fast anode pulse. The analysed parameters L, S and T are recorded in list mode using a FAST Comtec MPA-3 multichannel analyser [96].

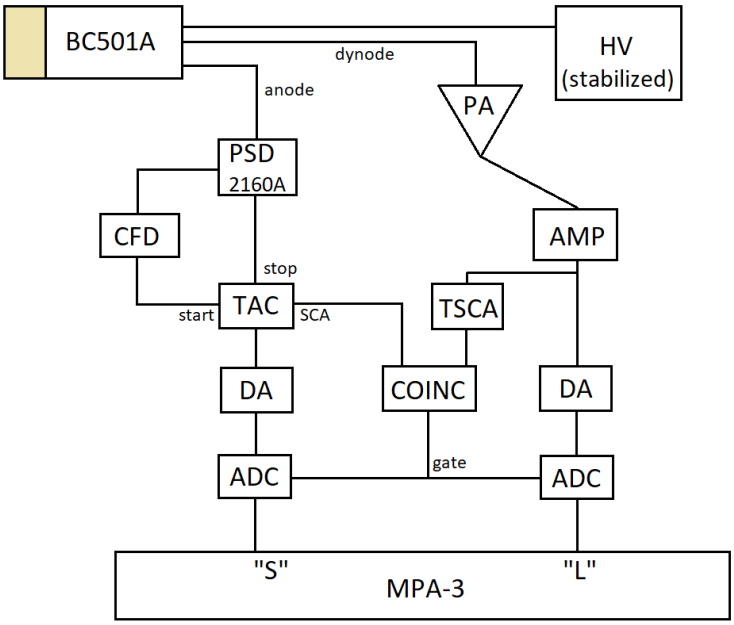

Figure 3.4: Schematic of the NIM-based analogue acquisition system at AMANDE. The dynode (slow) output producing light output parameter L, and anode (fast) output is used to calculate pulse shape parameter S. The high voltage (HV) is stabilised using the pulser signal from the detector.

3.1.4 Digital Pulse Processing

3.1.4.1 Parameter Definition

The following terms are used throughout:

- **Waveform** - Digitized analogue signal produced by the anode of the PMT.
- **(Analogue) Pulse** - A typical variation in output voltage by the detector directly corresponding with the deposition of energy in the detector by radiation.
- **Sample** - A single digital 14-bit measurement of the analogue pulse, can occur every 2 ns and is measured over the ranges of either 0.5 V_{pp} or 2.0 V_{pp}.
- **Event** - A set of sequential samples which contain one or more pulses. The set of samples is started by a trigger condition which indicates the presence of at least one pulse corresponding to radiation depositing energy in the detector.
- **Event sample time** - The duration (ns) of the acquisition window around the trigger, including the pre-trigger samples and post-trigger samples. The position of the trigger condition within this window is software selectable.
- **Waveform sample rate** - Rate at which a pulse is sampled. This has a fixed value of 500 MS/s (a sample every 2 ns) for the digitiser used.
- **Event sample rate** - Rate at which the triggering occurs. Limited by the reciprocal of the **event sample time** due to the trigger handling of the digitiser in conjunction with the custom developed software used. This is not the case for all CAEN digitiser control software.
- **Event data size** - Size of an event in bytes. This is given by the number of samples in an event and the size of the header.
- **Buffer size** - Size of the memory buffer that events can be written to without loss.
- **Readout rate** - Rate at which the buffers can be emptied by transferring events from the digitiser board to the controlling computer. This is limited by the data transfer speed defined by the mode of communication between the digitiser and the computer.

3.1.4.2 The DT5730 digitiser

The digital data acquisition system used in this work is a combination of an off-the-shelf CAEN DT5730 digitiser [97] and open-source UCT developed software, QtDAQ [98–100]. The DT5730 is an 8-channel, 14-bit digitiser with a sampling frequency of 500 MS/s.

The digitiser was used to acquire raw waveforms in list mode through a USB-2 (30 MB/s) connection to a laptop. For measurements requiring a faster readout rate the digitiser can use an optical link (80 MB/s) to communicate with a PC with the appropriate hardware.

Figure 3.5 shows a circuit diagram of the digitiser. The DT5730 digitiser features fast flash ADCs which are read out by a FPGA, which can be programmed to do any desired on-board real time analysis. The input voltage range of the digitiser is not limited to a single range through the use of a Programmable Gain Amplifier (PGA) allowing for a voltage range of either 0.5 V_{pp} or 2.0 V_{pp}. This makes the digitser versatile and able to acquire a large range of pulses without sacrificing voltage or timing resolution. The software programmable DC offset ($\pm$1.0 V, 16-bit resolution) allows for positive, negative going and bi-polar signals as input. This is implemented in the digitiser using operational amplifier to change the reference voltage.

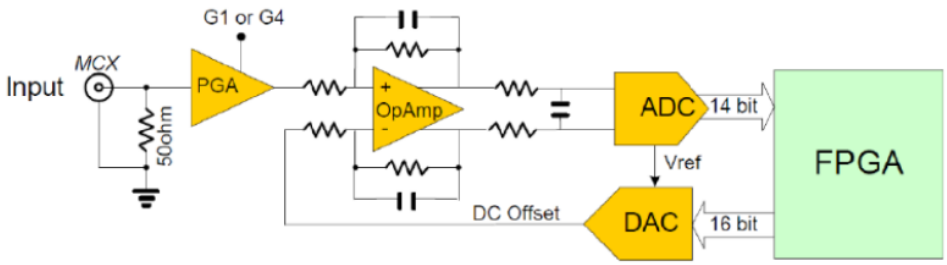

Figure 3.5: Schematic of the internal electronics of the CAEN DT5730 desktop digitiser from the analogue input stage to the signal read-out done by the FPGA [97].

The DT5730 digitser can perform the analysis of the waveform on-board and only acquire the analysed parameters in list mode, similar to the NIM-based analogue system. This limits the replay to re-analyse capabilities of the digital system. Acquiring the full raw waveform allows one to fully re-analyse the data to optimise the analysis parameters post-acquisition. The sampling rate of the DT5730 and bit resolution makes it suitable for measurements of low voltage amplitude, fast signals, making it possible to directly acquire the anode signal and eliminating the entire NIM-based signal processing chain on the anode.

For the measurement campaign at AMANDE the DT5730 was used to acquire list mode raw anode waveforms of the BC501A detector for the same beam conditions as the analogue measurements, at the maximum sampling rate of 500 MS/s. In this mode the digitiser samples the waveforms continuously using the 14-bit flash ADCs. These samples are read into an ADC and Memory Controller (AMC) FPGA which then stores the samples in a series of circular buffers. The DT5730 digitiser has two AMCs, one for the management of four channels. Sampling can occur simultaneously on all channels for any programmable or external trigger condition.

This allows for a wide variety of easy trigger setups using the digitiser. The trigger scheme implemented for these data was an absolute voltage threshold crossing.

Once a trigger condition is met the time consecutive samples within the chosen event sample time, prior to and after the trigger, are bunched together as an event. The event includes information on the trigger time to 16 ns resolution, the active channels, the trigger source and the time consecutive samples.

The size of the acquisition window (number of samples), percentage of this acquisition window which occurs post-trigger and number of events in a block transfer is programmable allowing this digitiser to be adaptable with respect to the event rates. The continuous sampling of the waveform, regardless of trigger condition, allows for the digitiser to include the desired amount of pre-trigger waveform. When a trigger condition is met the event buffer locks for read out and no additional triggers can occur during this time. This means that other pulses that occur during the acquisition window of a different pulse are effectively lost. This component adds to the event losses attributed to pile up. These losses can be minimised through optimised choices of event size or through pile up reconstruction algorithms. The proprietary CAEN software includes additional sophisticated trigger and pile up management schemes, minimising these effects through varying event size [101].

The UCT digital acquisition software, QtDAQ [98–100], was developed in C++ in conjunction with the Qt5 libraries [102] and the CAEN digitiser libraries [103]. The QtDAQ software produces event statistics for each event such as the long and short integrals, pulse shape, the constant fraction discriminator (CFD) and baseline of the individual pulses. These analysed parameters are then histogrammed and plotted accordingly. This is done through the flexible user interface which allows one to plot any of the event statistics as a 1D or 2D histogram in real time or in post-processing. User interfaces, configurations for acquisition and analysis can all be saved for reproducibility. An example of a user interface can be seen in figure 3.6.

All event statistics are calculated post acquisition of the event allowing the parameters to be reanalysed post acquisition. This ability is one of the main advantages that digital acquisition provides over analogue acquisition. All optimization can be achieved post acquisition, the only parameters which cannot be changed post acquisition are settings which affect the recording of the raw pulse such as trigger schemes and acquisition windows. For efficient acquisition QtDAQ implements a multi-threaded and double-buffered approach. There are three threads dedicated to the acquisition and processing of the events. One thread handles acquisition and can be locked by the processing thread. The acquisition thread is responsible for acquiring and writing events to memory where they are stored in one of the two buffers. When one buffer becomes full the acquisition thread moves to the next buffer. The full buffer is locked by the processing thread, preventing event overwrite. This thread is responsible for processing and execution of the user-defined Java-script.

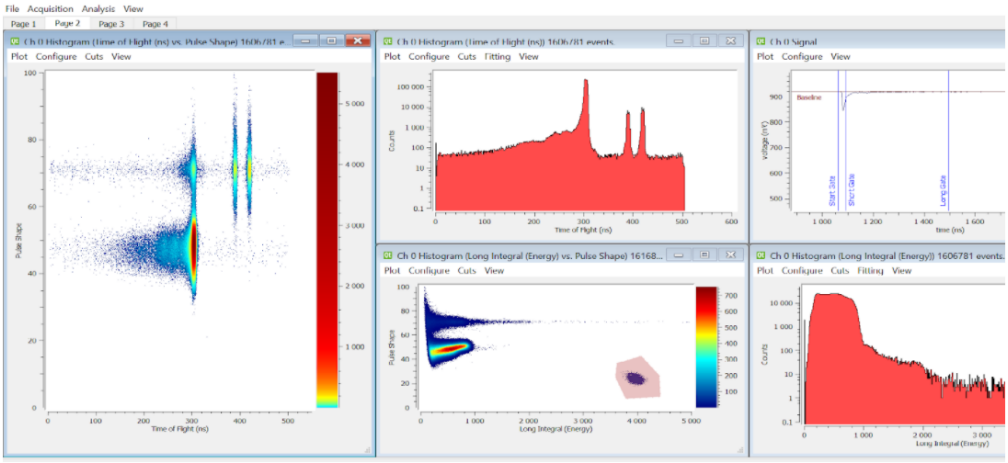

Figure 3.6: Screenshot of the multi-window user interface of the QtDAQ acquisition software. The windows shown include time-of-flight and light output parameters as 1D histograms in log scale, time-of-flight vs pulse shape and light output vs pulse shape as 2D histograms and the raw signal plots.

Only after the processing thread has emptied the buffer does it unlock for acquisition again. Events can be read out on an event by event basis or as a desired number of events packaged together for a block transfer. However, should the buffers be saturated all events after saturation will not be acquired until a read out occurs and space has been created for acquisition to continue. This saturation effect occurs when the event rate is higher than then combined read out rate. This is minimized through the selection of event size, number of events in one block transfer and the communication protocol between the digitiser and the acquisition computer. The remaining thread handles the user interface, updating of plots and the user interactions. This implementation allows for the maximum supported event rate to be significantly higher than a single threaded approach.

The storage of raw signals requires significant bandwidth and limits the maximum event rate supported. Acquiring analysed parameters only would increase the maximum measurable event rate. A typical full raw two channel event requires approximately 25 kB, uncompressed. For a measurable event rate of 4000 events/s the bandwidth required is then 100 MB/s. This bandwidth is reduced by QtDAQ which compresses the events when writing them to the desired storage device. The different dead time factors are explored in chapter 5.

Additionally, QtDAQ allows for user-defined analysis parameters. This provides versatility which is not obtainable in the analogue signal processing space. The pulse shape parameter used for these analyses is defined through the charge comparison method. This is the default pulse shape parameter in QtDAQ. For further flexibility the raw pulses can be analysed outside of QtDAQ.

3.1.5 Light Output Calibration

Acquired light output spectra require a calibration to provide a reference scale for unfolding. The neutron light output spectra were calibrated using the gamma-ray emissions from radioisotopic sources: ^{137}Cs (662 keV), ^{22}Na (511 keV and 1275 keV), ^{207}Bi (570 keV, 1064 keV and 1770 keV) and the ^{241}Am-^{9}Be associated gamma ray (4400 keV) [104]. The calibration consists of a linear fit relating the calculated light output parameter (L) to the known gamma-ray energy by:

$$L_{\mathrm{ch/LI}} = M(E_{\mathrm{c}} - 5\ \mathrm{keV}) + C, \tag{3.1}$$

where L is the light output parameter as either the digital long integral, or the analogue pulse height channel and E_{c} is the maximum energy in MeV of the Compton edge for each of the gamma-ray emissions associated with the calibration sources. The constants M and C are the linear regression factors determined through using a weighted Levenberg-Marquardt [105] linear fit optimization, where C is expected to be zero. The 5 keV is subtracted to account for the slight nonlinear behaviour of the light output for electrons at low L [106]. This calibration allows for the representation L in units of MeV for recoil electrons, by convention this is the same scale used to describe the neutron events, denoted as MeV electron equivalent, MeV$_{\mathrm{ee}}$. A typical calibration for the digital system with a 2.0 V input range is shown in figure 3.7. The light output spectra for a selection of gamma-ray sources are shown in figure 3.7 (a), and the calculated Compton edge energy against the digital light output parameter, the long integral, in figure 3.7 (b).

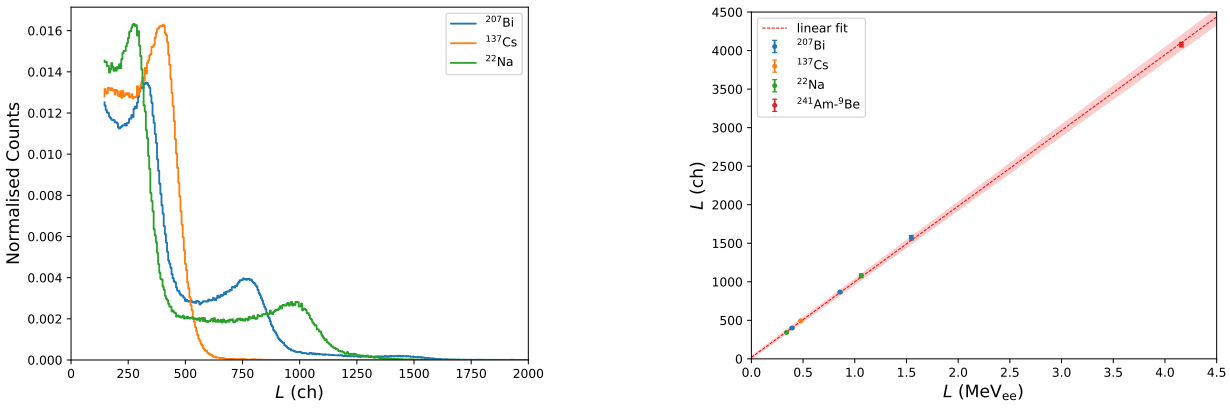

(a) **(b)**

Figure 3.7: (a) The uncalibrated light output spectra measured for the radioisotopic calibration sources. (b) The light output parameter of the Compton edge plotted against the known recoil electron energy for that edge in MeV$_{\mathrm{ee}}$ for the CAEN DT5730 digitiser with the input voltage being 2.0 V$_{\mathrm{pp}}$. The resultant refine fit being $M = 981.9(75)$ ch MeV^{-1} and $C = 18.2(62)$ ch.

The light output value of the Compton edge is taken as the inflection point of the edge of the gamma-ray distributions and can be refined to better match the detectors response functions by unfolding the calibration spectra and adjusting the calibration parameters to produce the expected full energy values associated with the decay of ^{137}Cs, ^{22}Na, ^{207}Bi and ^{241}Am-^{9}Be.

The resultant refined fit for the digital system with the 2.0 V_{pp} gain setting, figure 3.7, produces $M = 981.9(75)$ ch MeV^{-1} and $C = 18.2(62)$ ch.

3.1.6 Summary of Measurements

Measurements for Unfolding Analyses

Measurements, without time-of-flight information, were taken using the BC501A detector with each acquisition system, described in sections 3.1.3 and 3.1.4, independently for the same beam conditions. The detector was placed at 1.00 m from the target and at 0° to the incident ion beam for all measurements. Table 3.1 provides a summary of the beam conditions for the measurements made, where E_{ion} is the energy of the ion beam and $E_{\text{n, peak}}^{\text{calculated}}$ is the energy calculated with the known beam conditions using the TARGET code [92].

Table 3.1: Summary of beam conditions for the different measurements made with both acquisition systems. The beam intensities in bold are the AMANDE standard operating intensities.

Beam Type	E_{ion} [MeV]	Target	Thickness [μg cm^{-2}]	Reaction	$E_{n,peak}^{calculated}$ [MeV]	Beam Intensity [μA]			
proton	2.037	TiT	776	^{3}H(p,n)^{3}He	1.200±0.003		**4.5**		
proton	3.310	TiT	776	^{3}H(p,n)^{3}He	2.500±0.004	0.1	**0.5**	1.0	2.7
deuteron	1.841	TiD	793	^{2}H(d,n)^{3}He	5.000±0.003	0.1	**0.6**	2.6	5.1
deuteron	3.777	TiD	793	^{2}H(d,n)^{3}He	7.000±0.006	0.1	**0.6**	1.2	2.5
deuteron	0.432	TiT	776	^{3}H(d,n)^{4}He	15.060±0.010		**1.0**	1.5	2.5
deuteron	3.777	TiT	2045	^{3}H(d,n)^{4}He	20.480±0.008		**0.5**		2.1

The uncertainties quoted for the calculated neutron energy, as provided by the IRSN AMANDE team, have several contributing factors but is dominated by the spread in energy loss of the incident charged particles in the target.

Time-of-flight Measurements

The reference method for determining neutron energies at AMANDE relies on the use of a pulsed beam and the measurement of a time-of-flight (ToF) spectrum [86]. A pick-up ring at 1.00 m before the target provides the start signal.

When the beam reaches the target a portion of the produced neutrons and gamma-rays interact with the BC501A detector and create an event signal. The acquisition system then records the time from the start signal to when an event occurs in the detector. The difference between the time that the gamma-rays and neutrons arrive can be used to determine the time-of-flight parameter (T) defined as

$$T = t_n - t_\gamma + d/c, \tag{3.2}$$

where t_n and t_γ are the times in which the neutrons and gammas reach the detector respectively. Here d is the distance from the target to the detector and c is the speed of light. From T the neutron energy (E_n) can then be determined using the equation 2.11, detailed in section 2.3.2.

Time-of-flight measurements were used to validate the calculated neutron energy. The time-of-flight spectra were acquired by the MPA-3 analogue system with the BC501A detector for a range of distances from the target, 0° relative to the incident neutron beam. The neutrons were produced with a 2.00 MHz pulsed proton or deuteron beam incident on a TiT target. The calibrated time-of-flight parameter was determined to being 2.23 channel ns^{-1}. A summary of all the measurements can be found in table 3.2.

Table 3.2: Summary of the measurements made with a pulsed beam, including time-of-flight information. All measurements were made with a beam current of 2.8 μA and with a stop pulse frequency of 2.00 MHz.

Beam Type	E_{ion} [MeV]	Target	Thickness [μg cm^{-2}]	$E_{n,peak}^{calculated}$ [MeV]	Distance from Target [m]			
proton	3.310	TiT	2000	2.500		2.007		
deuterons	1.380	TiT	2450	17.000	1.752	2.750	3.750	4.750

Figure 3.8 shows the neutron energy spectra as determined via time-of-flight information for the measurement with the 3.310 MeV proton beam incident on a TiT producing 2.500(30) MeV neutrons. The counts have been normalised to an area of one. The measured result with an uncertainty, produced by fitting a Gaussian function to the peak, is 2.5020(24) MeV. This result agrees within one standard uncertainty to the expected value.

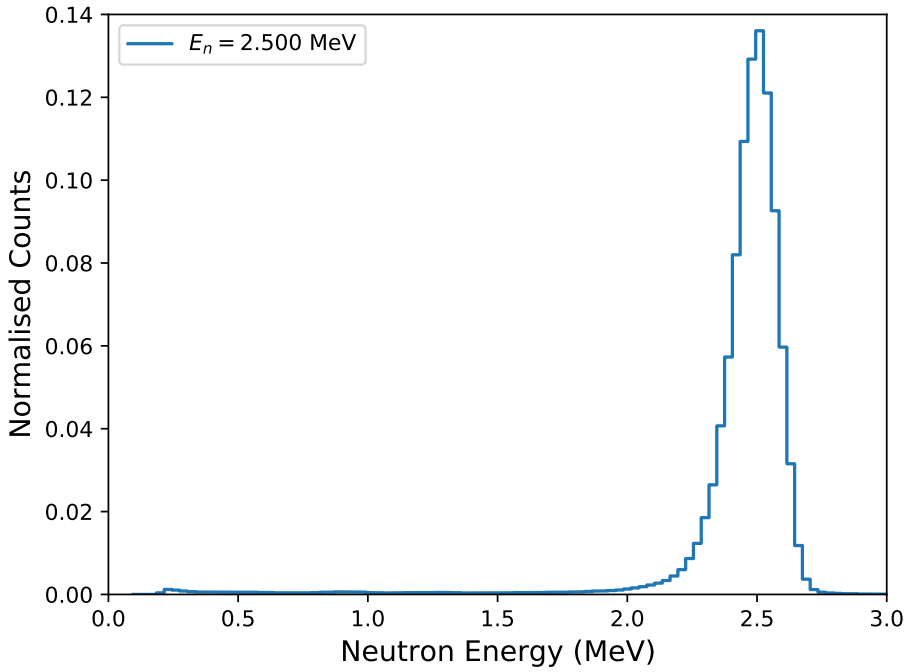

Figure 3.8: Neutron energy spectrum determined through time-of-flight measurements with the MPA-3 for the BC501A detector placed at 0° and 2.007 m from a 2000 µg cm^{-2} TiT target irradiated by a 3.31 MeV proton beam.

Monitor Measurements

Since measurements with the two different acquisition systems were not taken at the same time, monitor detectors are required to be able to compare fluence measurements across different acquisition systems, energy and intensity measurements. The two De Pangher long counters, M20 and M100, have been assumed to have negligible dead time [107]. The behaviour of the monitors are compared to ensure their effectiveness in relating the different measurements.

The ratios of the scalars are presented in figure 3.9 and are expected to remain constant over all beam conditions. The monitor ratios have been scaled by the first run in each batch of measurements for a given energy. The ratios are predominantly well behaved and consistent among each other. The inconsistencies seen in the run series with beam current 0.1 µA at both 5.000 MeV and 7.000 MeV is attributed to an incorrect range setting of the current integrator. Additionally, the behaviour seen in the run series for a beam current of 1.2 µA at 2.500MeV is likely due to an ill-aligned beam.

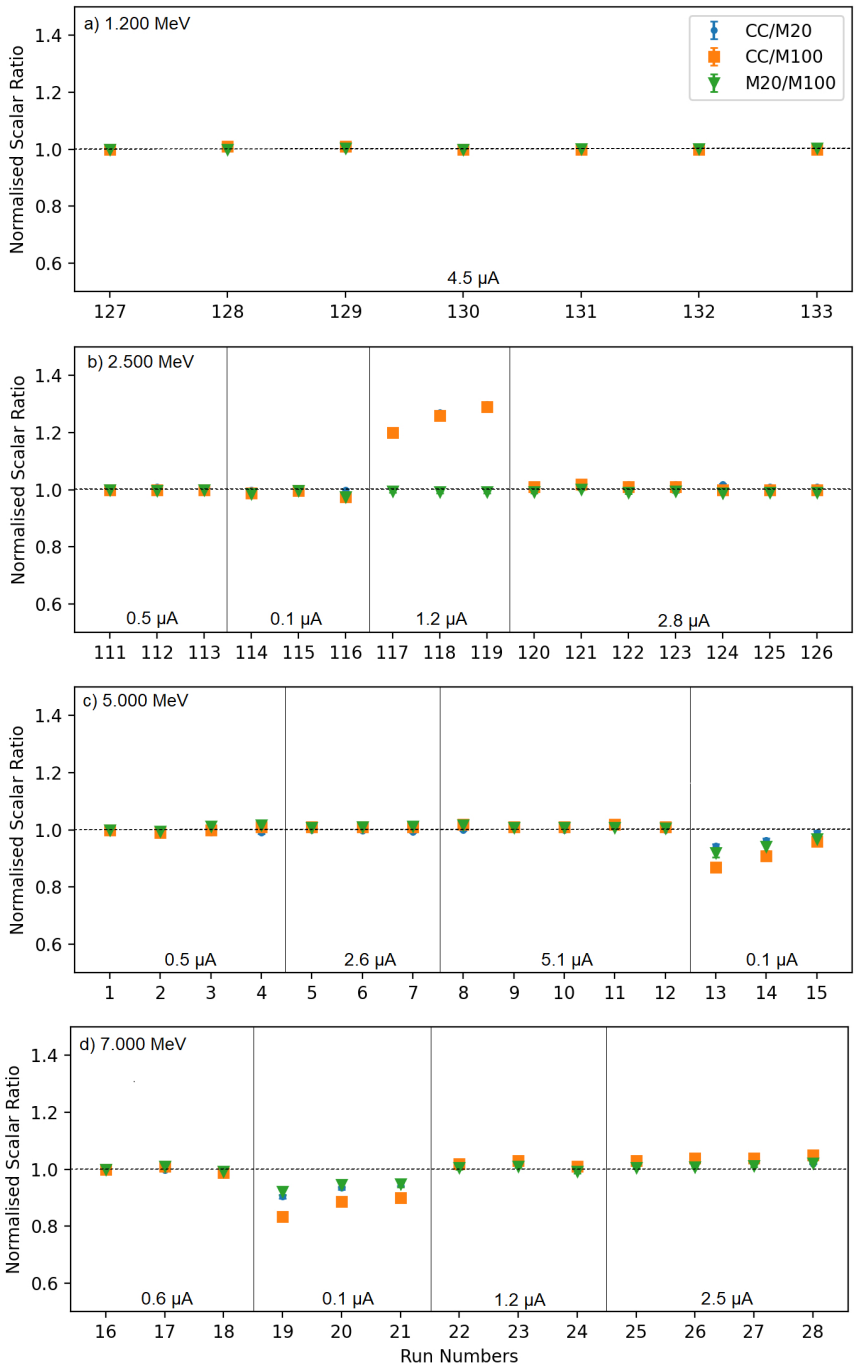

Figure 3.9: The ratio of the three monitors: current collector (CC); monitor M20 and monitor M100, for the four run series associated with radiation fields with nominal neutron energies of (a) 1.200 MeV; (b) 2.500 MeV; (c) 5.000 MeV and (d) 7.000 MeV. The monitor ratios have been scaled by the first run in each batch of measurements for a given energy.

4. Analogue Reference Standard

The measurements for a neutron beam of 1.200 MeV, 2.500 MeV, 5.000 MeV and 7.000 MeV (table 3.1), taken with a BC501A organic liquid scintillator detector with an analogue data acquisition system, detailed in section 3.1.3, are analysed in this chapter. Uncertainty budgets are constructed and presented along with correction factors for pile up and dead time.

4.1 Measurements

The analogue pulse processing chain, described in section 3.1.3 and figure 3.4, produces a light output parameter L from the dynode pulse height and a pulse shape parameter S through a standard zero crossing method (detailed in section 2.2). These parameters are then digitised with ADC's then acquired with a multi-parameter analyser (MPA-3) module in list mode. A sample plot of S vs the MeV_{ee} calibrated L for 15.100 MeV neutrons measured with the BC501A detector with the analogue standard acquisition system, can be seen in figure 4.1. The loci associated with the detection of recoiling electrons, protons, deuterons and alpha particles are labeled. Events due to protons escaping before full energy deposition can be seen in between the two loci. Pile up are also evident, occurring scattered for higher L and S values.

Measurements were made for the four different energies at the standard intensities. The scaled counts, for these measurements, as a function of S vs calibrated L can be seen in figure 4.2. The counts have been scaled by the monitor at 20° and then normalised to a unity integral. This has been done to be able to compare between the distributions. The measurements made at 15.100 MeV and 20.490 MeV, figure 4.2 (e) and (f) respectively, required a reduction in gain, relative to the measurements made below 10 MeV, to prevent light output saturation. The cut applied to isolate the neutron events as a function of S and L are show as a red line in the plots.

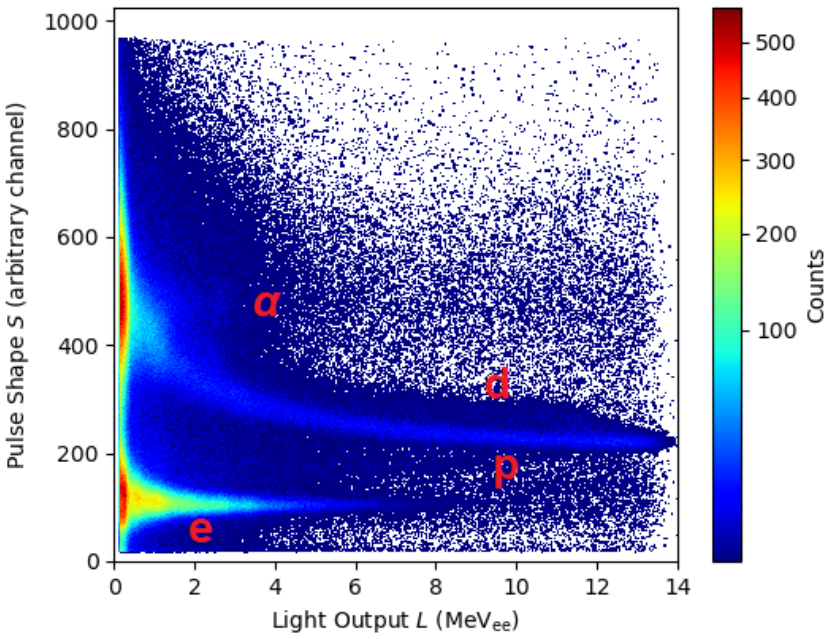

Figure 4.1: Counts as a function of L and S measured with the analogue metrology standard acquisition system for the BC501A scintillator detector exposed to both gamma-ray and neutron radiation. The neutrons were produced by irradiating a 2000 µg cm^{-2} TiT target with 3.78 MeV deuterons. The loci associated with the recoiling (α) alpha particles, (d) deuterons, (p) protons and (e) electrons are labeled on the plot. The escaping proton events are those occurring between the proton and electron loci. Pile up are also evident, occurring scattered for higher L and S values.

As discussed in section 2.1 the neutrons interacting with the detection medium predominantly interact through n-p elastic scattering. Other interactions such as n-^{12}C, producing protons, deuterons and alpha particles within the detector, become more probable with an increase in neutron energy. This can be seen through the development of the different features with increasing neutron energy in figure 4.2. The deuteron ridge, with a larger S value than the proton recoil locus, can be seen from the 5.000 MeV radiation field. With increasing energy the likelihood of the recoil proton escaping before depositing its full energy in the detector increases and the events occurring between the proton and electron loci increase. The pile up events, the events scattered to higher light output values and to higher pulse shape values, are also evident through all six radiation fields.

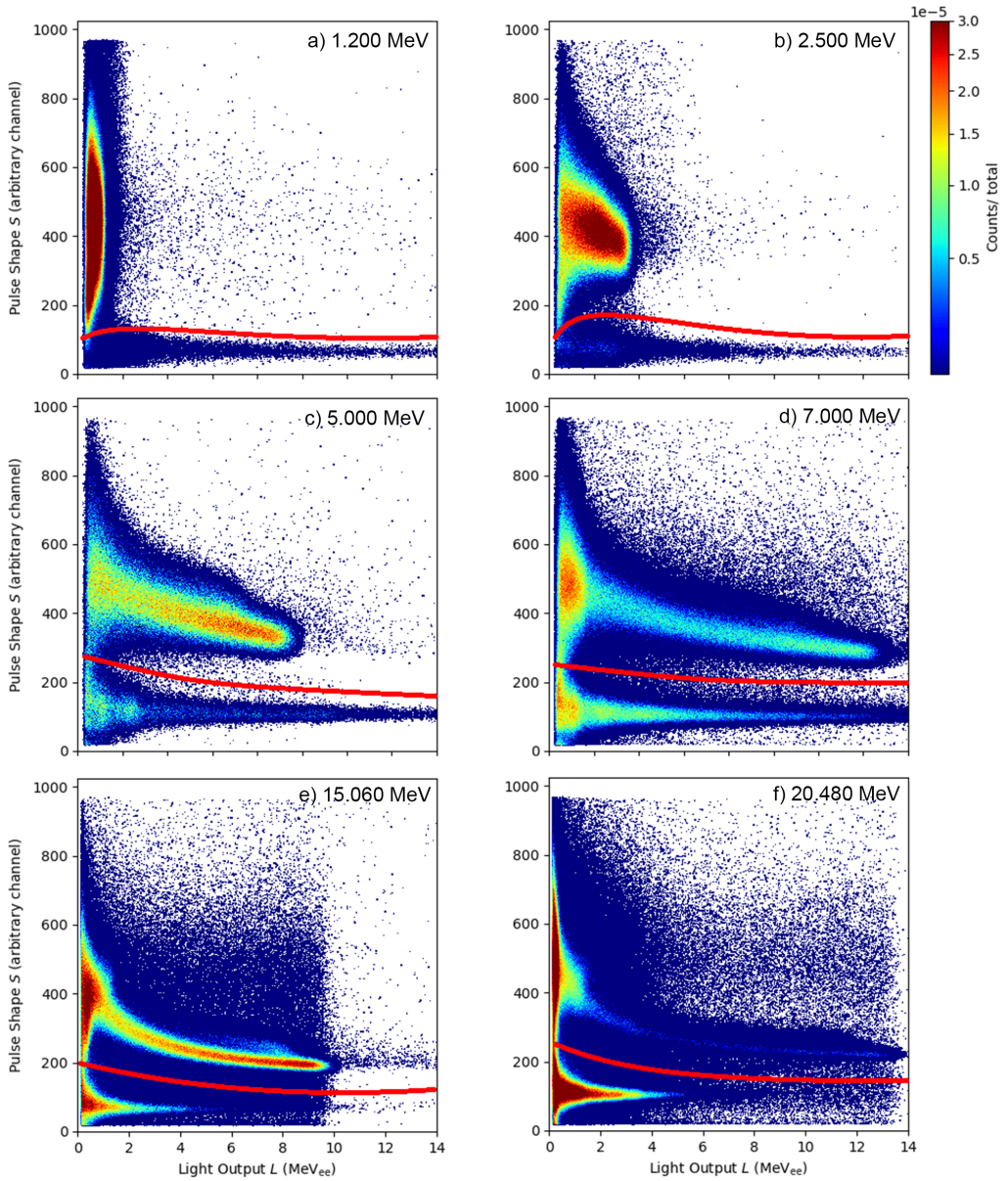

Figure 4.2: Scaled counts as a function of L and S for the standard intensity measurements as summarised in table 3.1 for (a) 1.200 MeV; (b) 2.500 MeV; (c) 5.000 MeV; (d) 7.000 MeV; (e) 15.100 MeV and (f) 20.490 MeV. The red line indicates the cut applied to this data to select for the neutron induced events.

The cuts applied to separate neutron and gamma-ray induced events were produced by slicing the data in figure 4.2 along the L axis, the two S loci centroid and their variance were calculated for each slice. This process is demonstrated in figure 4.3. The local minimum between the two loci is taken as the best cut location for a given slice. Another two cuts, closer to the base of each of the proton and electron loci, were taken to estimate the uncertainty in the neutron light output spectra obtained due to the choice of cut, represented by the red shaded region in figure 4.3(a). The upper and lower limit for the neutron cuts were placed at 2σ from the peak of the two loci as shown in figure 4.3(b).

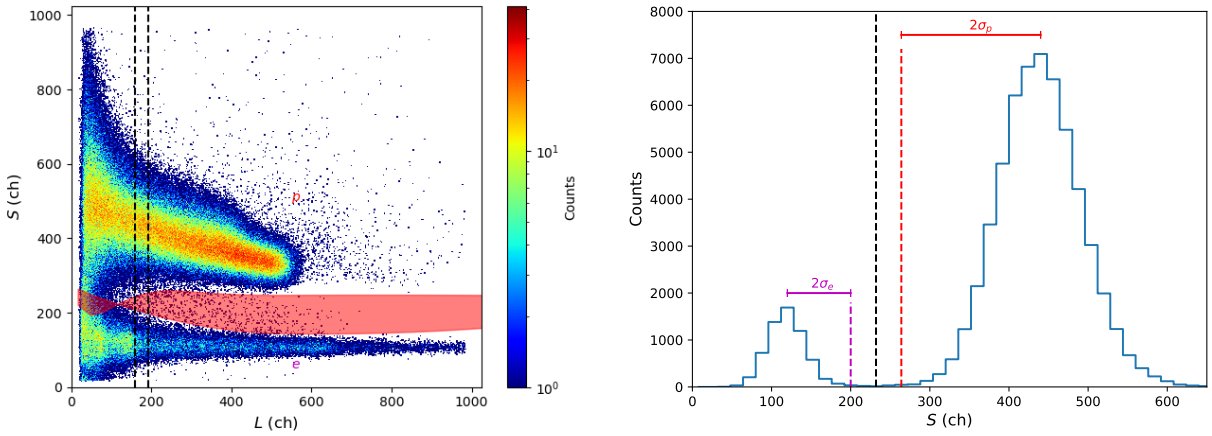

(a) **(b)**

Figure 4.3: (a) Sample *SL* plot of the 5.000 MeV neutron beam at a current of 0.5 µA where the red shaded regions indicates upper and lower limits used for the neutron cut. The dashed lines indicate the slice used to demonstrate the calculation of these limits as shown in (b). The limits were determined by 2σ from the peak with the minimum between the two distributions being chosen as the optimal cut position for that slice.

Figure 4.4 presents the neutron light output spectra normalised after being corrected for detector efficiency at a threshold of 0.25 MeV_{ee} for the standard intensities of these energies. The neutron light output spectra for the calculated neutron energy of 1.200 MeV, 2.500 MeV, 5.000 MeV and 7.000 MeV were unfolded and analysed further with respect to effects of beam intensity on the quality of the measurements.

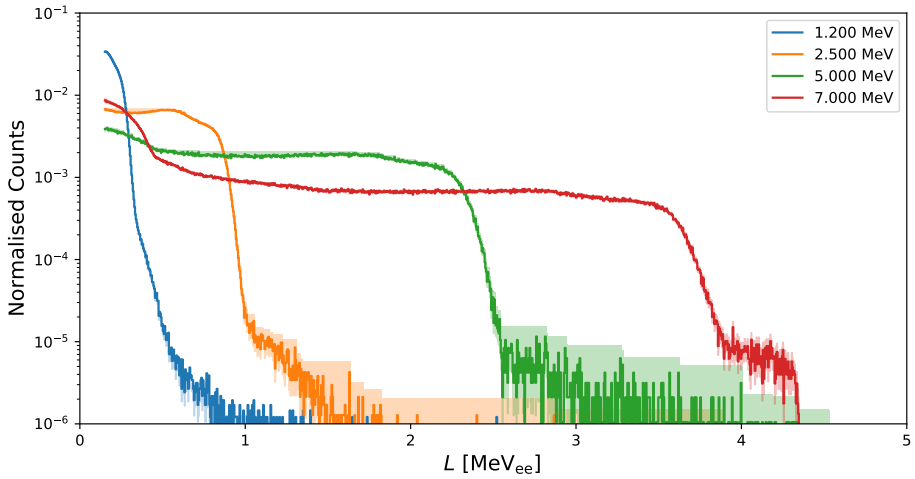

Figure 4.4: Neutron light output spectra for the measurements made at standard beam intensities for the four measured neutron energies: 1.200 MeV; 2.500 MeV; 5.000 MeV and 7.000 MeV, as selected by the cuts illustrated in figure 4.2. The spectra are scaled to an integral of unity. The uncertainties due to the cuts and Poisson statistics have been included for each light output spectrum as the lighter shading.

The neutron light output spectra were calibrated using gamma-ray sources as mentioned in section 3.1.5, with energies between 0.5 MeV and 4.4 MeV. The spectra have been normalised to have an area of one for shape comparison. The line shapes of the measured neutron light output spectra behave as expected with increasing energy, with an increasing edge. All spectra plotted show the effects of pulse pile up in the events occurring at higher MeV_{ee} values than the edge.

4.2 Unfolding

Using the UMG unfolding package developed by the PTB, the neutron energy spectra were unfolded from the light output spectra plotted in figure 4.4 using the response functions shown in figure 3.3. The spectra were first unfolded using GRAVEL with a flat default spectrum, the output from GRAVEL was used as the default spectra supplied to MAXED for the final unfolding. Unfolding with both GRAVEL and MAXED are completed due to the different stability of the solution, dependent on the default spectrum. GRAVEL converges with little dependence the default spectrum whereas MAXED relies on a reasonable default spectrum for stable convergence. The uncertainty propagation package IQCU [74] relies on the output of MAXED. The results from GRAVEL were also used to determine a reasonable χ^2 for MAXED.

All solutions had a final χ^2 per degree of freedom value of 4.0 or below, iterating between 200 to 400 times, with the exception of some of the MAXED solutions not iterating more than 4 times. The refolded light output spectra of the final MAXED solution from the unfolding process plotted along with their associated measurements, for the four standard intensity radiation fields can be seen in figure 4.5. The refolded light output spectra agree within uncertainty to the measurements. The measured spectra plotted in figure 4.5 have not been scaled, these are the raw light output spectra. The refolded spectrum for the 2.500 MeV (figure 4.5(b)) has a small bump at around 0.3 MeV which then produces a small peak in the unfolded spectrum which is an artefact.

Figure 4.6 shows the final MAXED unfolded neutron energy spectra for the standard intensities of the four neutron energy measurements. The neutron energy spectra plotted here have been scaled by to fluence per micro-amp of charged particle beam (Φ_E/Q). Presenting the measurements in these units require scaling by the monitor value, followed by the correction factors for dead time and pulse pile up. The correction factors are discussed in detail in section 4.4. The neutron energy spectra have a primary peak near to the expected energies and additional lower energy peaks in figure 4.6 (c) and (d). These lower energy peaks are associated with secondary reaction channels in the target from the ions interacting with oxygen and carbon [108].

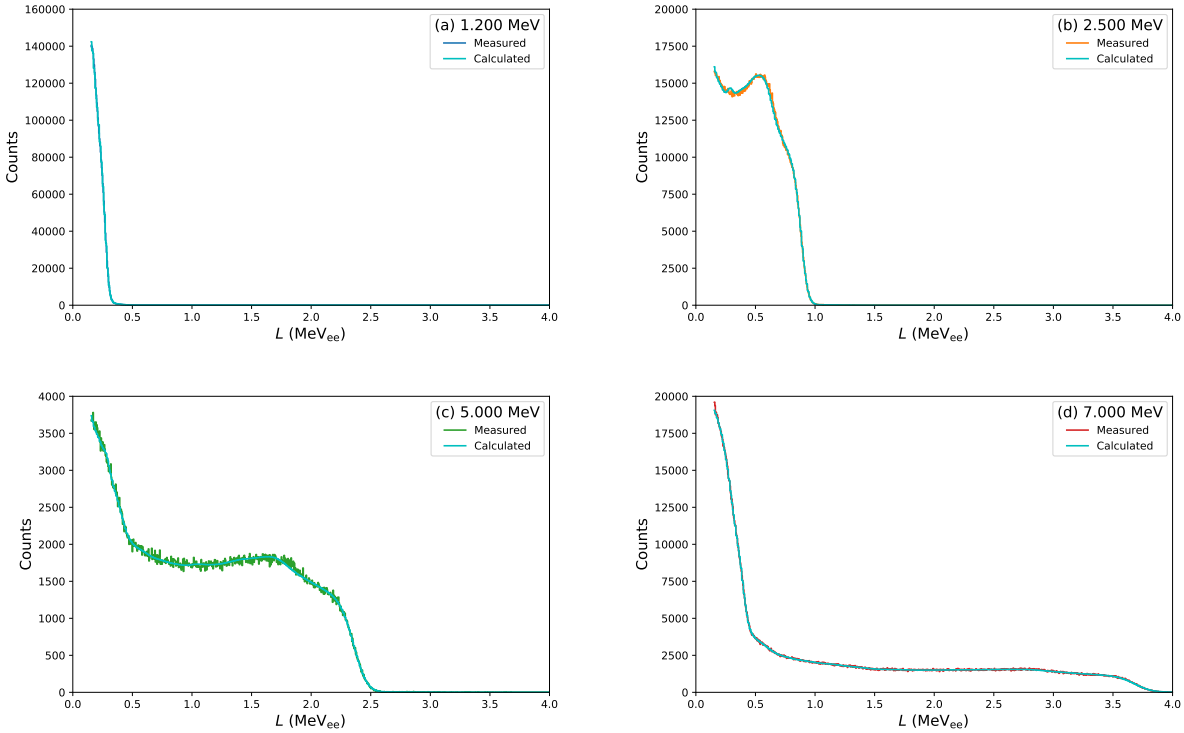

Figure 4.5: Neutron light output spectra measured with the BC501A detector coupled with the analogue acquisition system for four neutron fields with nominal energies of (a) 1.200 MeV; (b) 2.500 MeV; (c) 5.000 MeV and (d) 7.000 MeV for the standard intensities. The refolded light output spectra from the unfolding calculations have been included as the light blue line in each of the plots.

In figure 4.6 (c) and (d) there is a small peak occurring at a higher MeV value than that of the primary peak, this is attributed to pile up events. Evidence for this being due to pile up is presented in section 4.5 where the effect of increasing intensity is investigated. The width of the primary peak is predominately due to the thickness of the target. The asymmetry in the peak is due to additional dispersion to the lower energies of the peak due to energy loss within the target.

The higher energy tail in figure 4.6 (a), for the 1.200 MeV neutron measurement, is an artefact of unfolding due to the applied threshold being on the edge of the proton recoil in the light output spectrum shown in figure 4.4. The small peaks occurring just above 1 MeV in figure 4.6 (b) and (c) are unlikely to be an artefact of the unfolding as they are also seen in the varying intensity measurements for these energies in section 4.5.

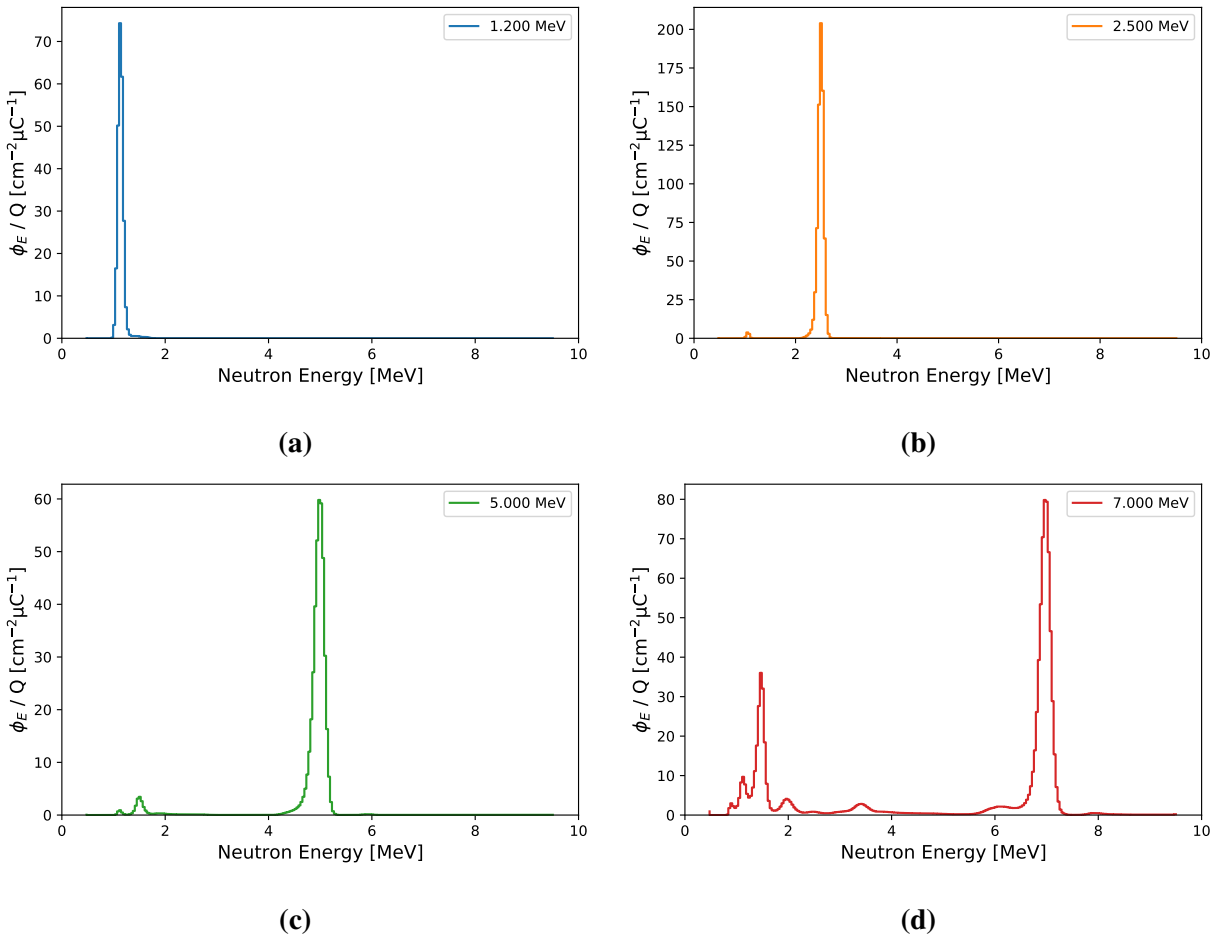

Figure 4.6: MAXED unfolded neutron energy spectra measured with the analogue acquisition system for four neutron fields with nominal energies of (a) 1.200 MeV; (b) 2.500 MeV; (c) 5.000 MeV and (d) 7.000 MeV for the standard intensities. Affects of pile up are visible in (d) by the peak at 8.5 MeV.

4.3 Peak Neutron Energy Uncertainty Analysis

The uncertainty analysis presented here follows an ISO-GUM approach [109]. The quoted measured values of the primary peak for the neutron energy measurements, $E^{obs}_{n,peak}$, were determined by fitting a Gaussian distribution to the primary peak. The uncertainty in this value has contributions from the fitting and unfolding but is effectively determined by the MeV_{ee} calibration described in section 3.1.5. This is because the unfolding process is highly dependent on an accurate MeV_{ee} scale. For more information on the UMG unfolding package and its uncertainty calculations refer to Appendix A.

The uncertainty in the unfolded peak value, $u\left(E^{obs}_{n,peak}\right)$, is determined by unfolding spectra with the upper and lower limits of the MeV_{ee} scale ($\pm\sigma$) and determining the limits of the peak position. The uncertainty in the unfolded peak value is then half of the difference of those limits.

The upper and lower limits of the scale determined by the uncertainty on the fit parameters M and C in equation 3.1, the limits on the scale would therefore have parameters $M \pm u(M)$ and $C \pm u(C)$. These uncertainties were determined through the co-variance matrix of the fit parameters.

The measured values for the primary energy peaks and their associated uncertainties are shown in table 4.1 with the calculated values for the same data sets. The calculated values have been validated through time-of-flight measurements and the kinematic calculations with the TARGET code [92] are well understood and documented. Uncertainties for these values have been previously documented [90].

Table 4.1: Calculated (calc) and measured (obs) values for the peak neutron energy.

$E^{calc}_{n,peak}$ (MeV)	$E^{obs}_{n,peak}$ (MeV)
1.200 ± 0.003	1.200 ± 0.020
2.500 ± 0.004	2.636 ± 0.016
5.000 ± 0.003	5.235 ± 0.025
7.000 ± 0.006	7.320 ± 0.032

Evidently there is a problem with the measured peak neutron energy values where they are consistently greater than the expected neutron energy values, this is further demonstrated in figure 4.7. The measured peak neutron energy has been plotted against the expected values indicating linear behaviour between them. These data were fitted using a weighted linear least squares fit, with the resultant slope taking the value m = 1.048(17) and the intercept being zero within uncertainty.

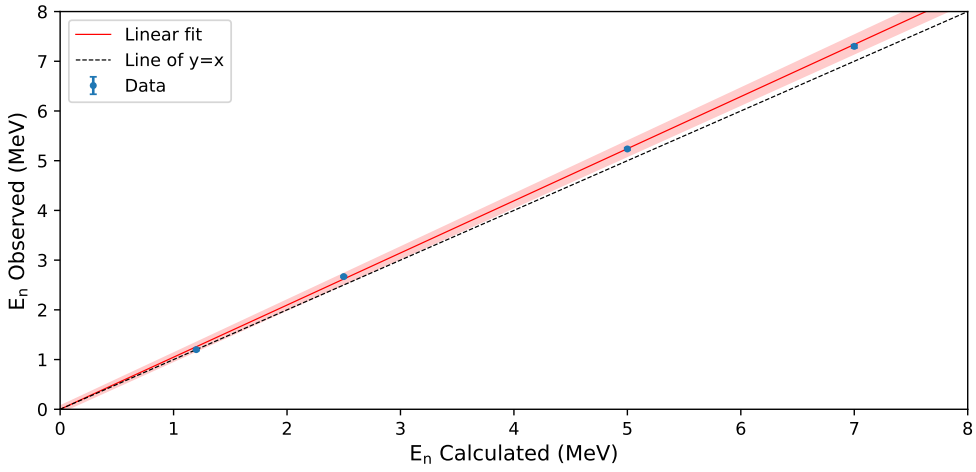

Figure 4.7: The observed neutron peak energies (MeV) vs the calculated neutron peak energies (MeV). The weighted linear least square fit has a slope value of 1.048(17).

The difference in the observed and the calculated neutron peaks is attributed to the ageing scintillator changing the light transport and production in the detector resulting in the response matrix no longer matching the light output function of the detector, seen in figure 4.8. There is a clear degradation in the resolution of the detector. It is recommended that the response functions be updated to account for these differences, but goes beyond the scope of this work.

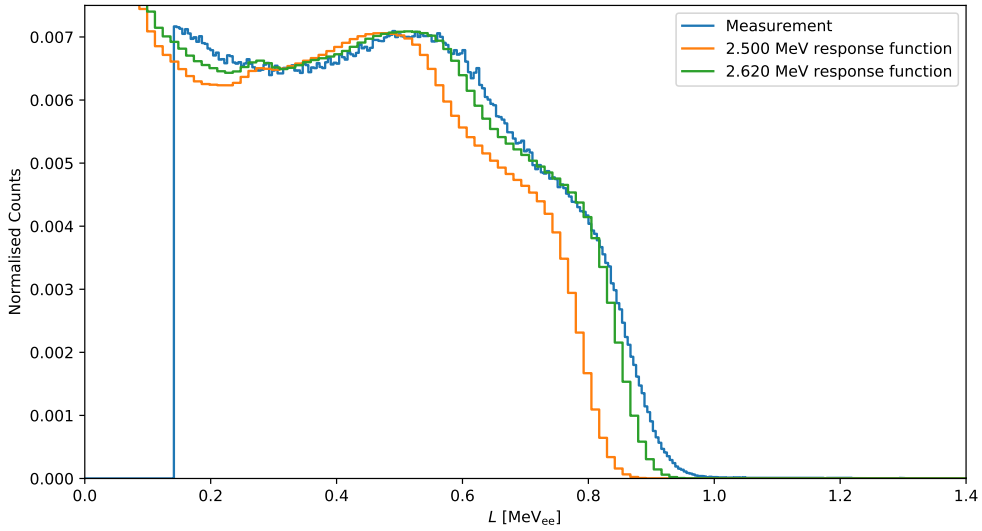

Figure 4.8: The measured light output spectrum for a 2.500 MeV neutron field together with the detectors response lineshapes for 2.500 MeV and 2.620 MeV neutron fields obtained from the response matrix.

To account for the difference between the observed and calculated values, without updating the response functions, a scaling factor k_{RM} is introduced. This factor is defined to being the inverse of the gradient (m) determined in figure 4.7, equation 4.1.

$$k_{RM} := \frac{1}{m} = 0.954. \tag{4.1}$$

The uncertainty in k_{RM} is then:

$$u(k_{RM}) = k_{RM}\frac{u(m)}{m} = 0.015. \tag{4.2}$$

The new best estimate for the neutron energy, $E^{meas}_{n,peak}$, is defined as the observed peak value scaled by k_{RM}, equation 4.3.

$$E^{meas}_{n,peak} := k_{RM}E^{obs}_{n,peak} \tag{4.3}$$

The uncertainty associated with this new estimate for the neutron peak energy is then the combination of the uncertainty in original energy estimate and the uncertainty in the scaling factor k_{RM}, refer to equation 4.4.

$$u\left(E_{n,peak}^{meas}\right) = E_{n,peak}^{meas}\sqrt{\left[\frac{u\left(E_{n,peak}^{obs}\right)}{E_{n,peak}^{obs}}\right]^2 + \left[\frac{u(k_{RM})}{k_{RM}}\right]^2} \tag{4.4}$$

The results of applying this scaling factor is shown in table 4.2. The final $E_{n,peak}^{meas}$ results agree with the calculated values to within one standard uncertainty except for the 1.200 MeV measurement.

Table 4.2: Calculated and measured final values for the standard intensity neutron energy measurements made with the analogue MPA-3 acquisition system.

$E_{n,peak}^{calc}$	(MeV)	1.200(3)	2.500(4)	5.000(3)	7.000(6)
$E_{n,peak}^{obs}$	(MeV)	1.200(20)	2.636(16)	5.235(25)	7.320(32)
$E_{n,peak}^{meas}$	(MeV)	1.145(26)	2.515(42)	4.994(82)	6.98(11)

4.4 Peak Fluence Intensity Uncertainty Analysis

The peak neutron fluence is taken to be the integral of the channels associated with the primary peak, refer to equation 4.5.

$$\Phi_{E,peak}^{obs} = \sum_{j=i-6\sigma}^{i+3\sigma} \phi_j, \tag{4.5}$$

where ϕ_j is the jth channel of the raw unfolded neutron energy spectrum ϕ, i is the centroid channel of the primary peak and σ is the standard deviation of the peak in channels. The sum is then a sum of the counts in the channels starting from 6σ to lower E of the primary peak and ending at 3σ to the higher E of the peak. The summation needs to capture the asymmetry of the peak.

The uncertainty in $\Phi_{E,peak}^{obs}$ is then defined by the uncertainties in each channel, $u(\phi_j)$. These are obtained from the outputted parameter file from MAXED unfolding via the code ICQU, appendix A, which propagates the uncertainties provided in the neutron light output spectra through the unfolding process.

The uncertainties in the counts in each $\mathrm{MeV_{ee}}$ channel of the neutron light output spectra, $u(L_j)$, is the quadrature sum of the uncertainty due Poisson statistics and the uncertainty associated with the neutron cuts, as seen in equation 4.6.

$$u(L_j) = \sqrt{u\left(L_{j,Poisson}\right)^2 + u\left(L_{j,cut}\right)^2}, \tag{4.6}$$

where $u\left(L_{j,Poisson}\right)$ is equal to the square root of the counts in channel j and $u\left(L_{j,cut}\right)$ takes on the value of half of the counts in between the upper and lower limits of the neutron cut for that channel. Figure 4.9 demonstrates the value of $u\left(L_{j,cut}\right)$.

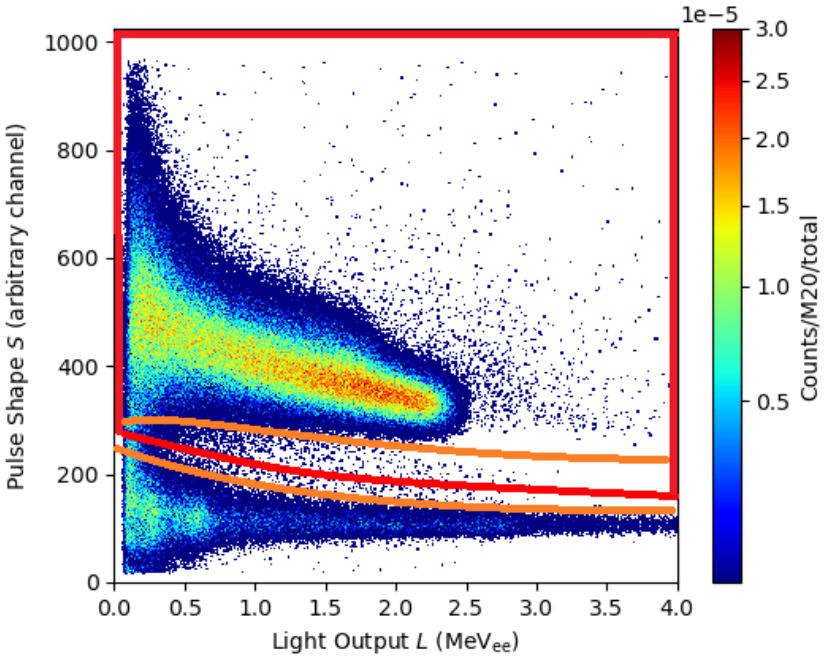

Figure 4.9: Sample PSD neutron cut with the upper and lower limits included in orange with the main cut in red, for a 5.000 MeV data set. The counts that occur between the orange limits are the uncertainty on the counts in the channels of the cut neutron light output spectrum.

Figure 4.10 shows the uncertainties; $u\left(L_{j,Poisson}\right)$, $u\left(L_{j,cut}\right)$ and $u(L_j)$, plotted for the same data set in figure 4.9. This plot shows how the two uncertainties are dominant at different points through the spectrum and the cut uncertainty mainly affects the light output spectra at low $\mathrm{MeV_{ee}}$.

The uncertainty $u(L_j)$ is dominated by $u\left(L_{j,cut}\right)$ below 0.27 $\mathrm{MeV_{ee}}$, above this $u\left(L_{j,Poisson}\right)$ is the main source of uncertainty. The uncertainty in the cuts increase dramatically at low L and goes to zero quickly past 0.5 $\mathrm{MeV_{ee}}$, while $u\left(L_{j,Poisson}\right)$ has the same distribution as the neutron light output spectrum.

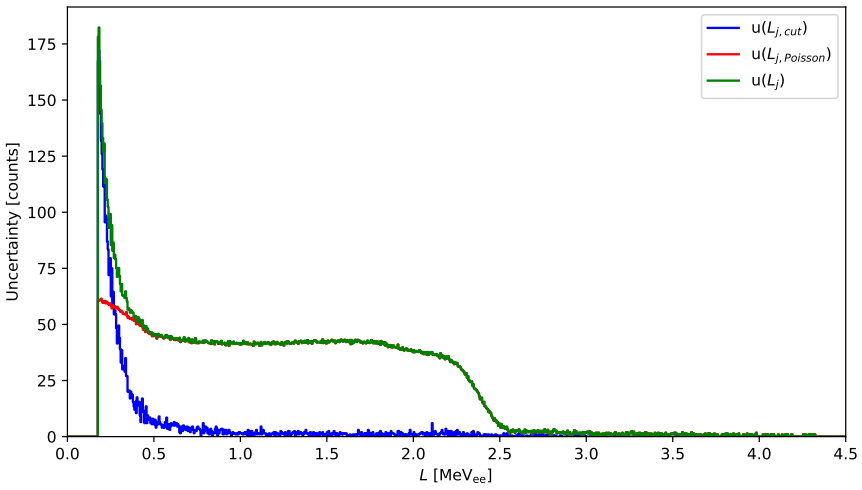

Figure 4.10: For the same sample data set shown in figure 4.9 the uncertainties $u\left(L_{j,Poisson}\right)$, $u\left(L_{j,cut}\right)$ and $u(L_j)$ have been plotted for each channel j.

These uncertainties were then propagated through the unfolding calculation using the output parameter files from MAXED and the ICQU package to produce $u(\phi_j)$. The final uncertainty in the measure peak fluence, $u\left(\Phi^{obs}_{E,peak}\right)$, is then determined by:

$$u\left(\Phi^{obs}_{E,peak}\right) = \sqrt{\sum_{j=i-6\sigma}^{i+3\sigma} u(\phi_j)^2}. \tag{4.7}$$

In order to obtain the fluence measurement in neutrons cm^{-2} μC^{-1}, the unfolded neutron energy spectra need to be scaled by a monitor value and corrected for dead time and other missing events. Thus $\Phi^{meas}_{E,peak}$ is defined as:

$$\Phi^{meas}_{E,peak} := k_{DT} \frac{\Phi^{obs}_{E,peak}}{Q}, \tag{4.8}$$

where Q is the charge integrator count and k_{DT} is the dead time correction factor. This dead time correction factor is made up of three factors; the quoted dead time on the MPA-3 (k_{MPA}) and the pulse pile up correction (k_{PU}). These three correction factors multiplied together produce k_{DT} as shown in equation 4.9.

$$k_{DT} = k_{MPA}\, k_{PU} \tag{4.9}$$

The correction for pile up, k_{PU}, is calculated from the proportion of events that occur beyond the edge of the light output spectrum and the uncertainty in this value is predominantly due to Poisson statistics, and should increase with beam current. The uncertainty equation for $\Phi^{\text{measured}}_{\text{E, peak}}$ can now be defined as:

$$u\left(\Phi^{meas}_{E,peak}\right) = \Phi^{meas}_{E,peak}\sqrt{\left[\frac{u\left(\Phi^{obs}_{E,peak}\right)}{\Phi^{obs}_{E,peak}}\right]^2 + \left[\frac{u(Q)}{Q}\right]^2 + \left[\frac{u(k_{DT})}{k_{DT}}\right]^2}, \tag{4.10}$$

where $u(Q)$ is equal to the square root of Q and k_{DT} is given by:

$$k_{DT} = k_{DT}\sqrt{\left[\frac{u(k_{MPA})}{k_{MPA}}\right]^2 + \left[\frac{u(k_{PU})}{k_{PU}}\right]^2}. \tag{4.11}$$

The scaling factors for the peak neutron fluence calculations for the standard intensity measurements have been tabulated with their associated uncertainties in table 4.3.

Table 4.3: The calculated scaling factors with their associated uncertainties for the peak neutron fluence calculations for the standard intensity measurements. *The starred values are estimated

$E^{calc}_{n,peak}$ (MeV)	1.200(3)	2.500(4)	5.000(3)	7.000(6)
Q (μC)	2427.98(16)	423.231(21)	369.793(19)	416.161(20)
k_{MPA}	1.02(1)*	1.011(29)	1.0053(61)	1.0164(48)
k_{PU}	1.00183(94)	1.00108(73)	1.0009(32)	1.0009(27)

The resultant fluence measurements for the standard intensities are presented in table 4.4 along with their associated uncertainties.

Table 4.4: The calculated neutron fluence measurements for the peak neutron fluence calculations for the standard intensity measurements with and without the correction factors,along with their associated uncertainties. *The starred values have uncertainties produced through ICQU that were very small.

$E^{calc}_{n,peak}$ (MeV)	1.200(3)	2.500(4)	5.000(3)	7.000(6)
$\Phi^{obs}_{E,peak}$ ($\times 10^4 \text{cm}^{-2}$)	59.26(23)	*303.11	*14.69	23.5953(36)
$\Phi^{meas}_{E,peak}$ (cm^{-2} μC^{-1})	244.5(12)	720(21)	398.6(28)	576.8(32)

4.5 Varying Intensity Measurements

The affects of varying intensity in the neutron fields were investigated at the nominal neutron energies of 2.500 MeV, 5.000 MeV and 7.000 MeV (1.2 MeV data not included in this section due to only having one intensity measurement at that energy). The measurements were run to statistically equivalent numbers of neutron events. The intensity ranges investigated included the minimum and maximum stable beam conditions for each nominal energy.

Exemplar data for the 7.000 MeV measurement are shown in figure 4.11, the figures for the nominal energies of 2.500 MeV and 5.000 MeV can be found in appendix B. The counts as a function of S and L for have been normalised by area to aid in comparison.

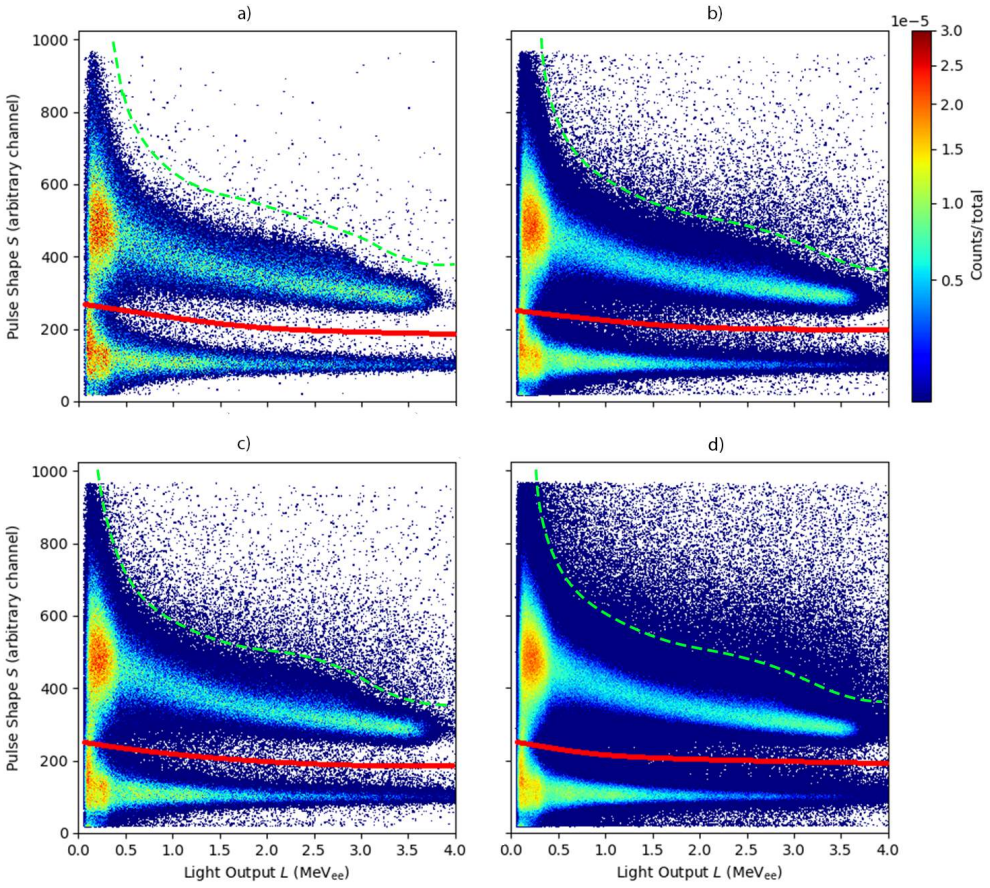

Figure 4.11: Counts as a function of S and L measured with the analogue acquisition system for four neutron fields with a nominal energy of 7.000 MeV for beam currents of (a) 0.120 µA; (b) 0.574 µA; (c) 1.130 µA and (d) 2.500 µA. The cut applied used to separate the gamma-ray and neutron induced events is indicated by the red line. Pile up events are those considered above the green dashed line.

At each nominal energy it is clear that the overall distribution of the measurements remain the same, but an increasing proportion of pile up events (events occurring above the green dashed line in figure 4.11) is seen with the increasing intensity.

The neutron light output spectra for the different beam conditions for all three nominal neutron energies have been plotted in figure 4.12.

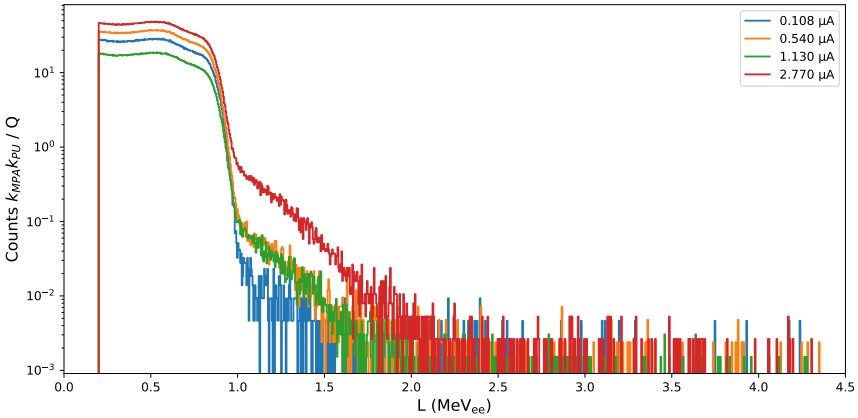

(a)

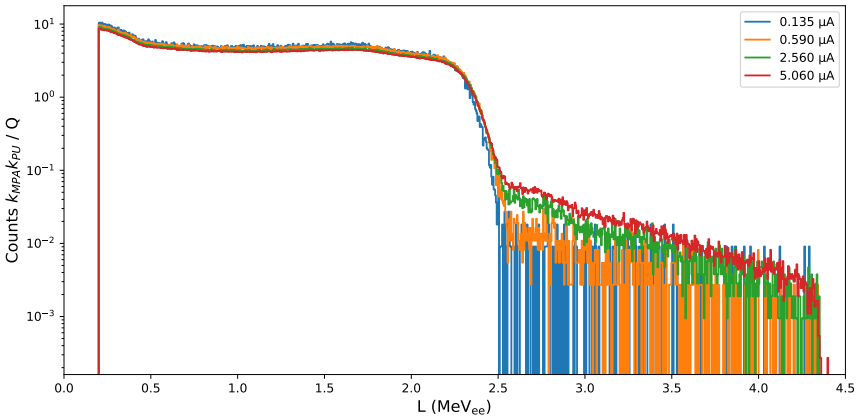

(b)

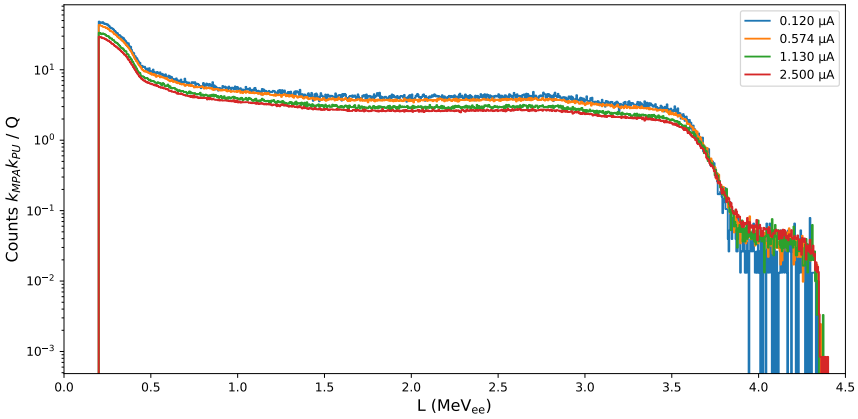

(c)

Figure 4.12: Neutron light output spectra for three different nominal neutron energies (a) 2.500 MeV, (b) 5.000 MeV and (c) 7.000 MeV. At each energy four different beam intensities were measured. The spectra have all been scaled by the charge integrator monitor value and corrected for by k_{DT}.

The unfolded absolute fluence spectra scaled accordingly have been plotted in figure 4.13. As a result of the difference in the neutron light output spectra shown in figure 4.12(a) and (c), the unfolded neutron energy spectra for the different beam intensities do not align in amplitude. The 5.000 MeV unfolded spectra behaves as expected. All unfolded spectra align in energy and resolution. The affects of pulse pile up only being evident at the higher intensities at each energy in the form of a low intensity contribution above the primary peak.

The primary peak neutron energy measurements quoted in table 4.5 have all been scaled appropriately using the same scaling factor determined in equation 4.1 in section 4.3. The raw peak neutron fluences, $\Phi^{obs}_{E,peak}$, for each of the beam conditions, along with the associated scaling factors k_{MPA}, k_{PU} and Q, can be found in tables B.1, B.2 and B.3 in appendix B. These fluences were calculated from the output of the ICQU UMG package.

Table 4.5: Measurements of the neutron energies and peak fluence for varying intensities of the nominal neutron energies of 2.500 MeV, 5.000 MeV and 7.000 MeV.

$E^{calc}_{n,peak}$ [MeV]	Beam Current [μA]	$E^{meas}_{n,peak}$ [MeV]	$\Phi^{meas}_{E,peak}$ [$cm^{-2}\mu C^{-1}$]
2.500(4)	0.108	2.515(42)	551.4(23)
	0.540	2.515(42)	720(21)
	1.130	2.514(42)	358.4(11)
	2.770	2.518(43)	924.4(29)
5.000(3)	0.135	4.953(81)	405.1(12)
	0.490	4.994(82)	398.6(28)
	2.560	4.998(82)	368.4(10)
	5.060	4.995(82)	353.51(45)
7.000(6)	0.120	6.97(11)	632.1(31)
	0.574	6.98(11)	576.8(32)
	1.130	7.00(11)	454.5(12)
	2.500	7.00(11)	405.32(60)

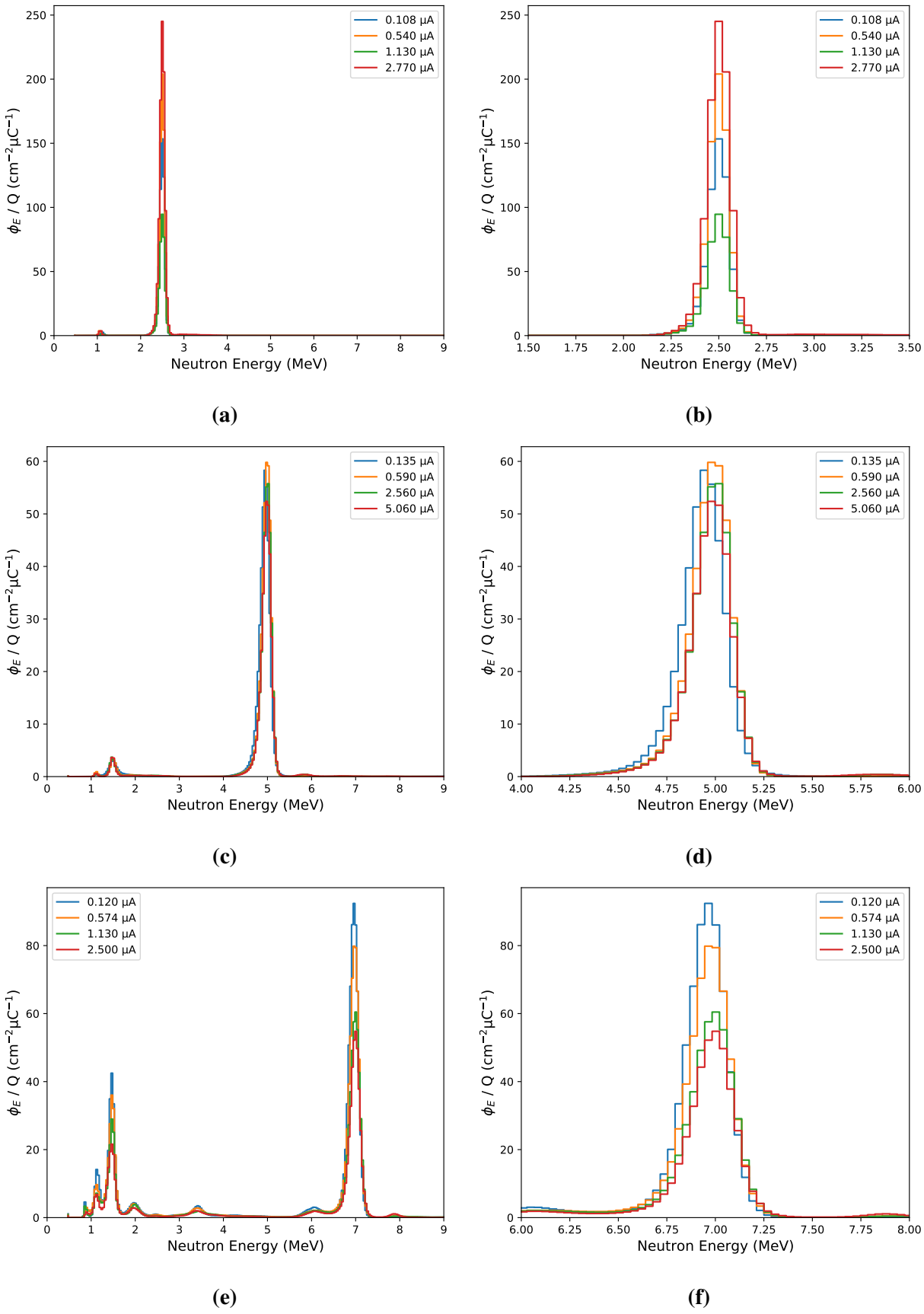

Figure 4.13: Unfolded fluence spectra, in cm^{-2}µC^{-1}, for the different intensity beams at the nominal energies of (a) 2.500 MeV, (c) 5.000 MeV and (e) 7.000 MeV, plots (b), (d) and (f) show only the nominal peaks of the same spectra respectively. All spectra are corrected for using k_{DT}.

5. Single Channel Digital Data Acquisition

For measurements made at AMANDE with the DT5730 digitiser the raw anode signal from the BC501A detector was acquired in listmode, as described in section 3.1.4. The measurements were made with the same beam conditions as the analogue acquisition system.

5.1 Analysis Parameter Optimisation

One of the advantages of digital data acquisition and post acquisition analysis is the optimization of analysis parameters post acquisition. Parameters such as the factors which define the digital constant fraction discriminator, the size of the windows used for the integral calculation (t_0, t_s and t_l), the pulse shape parameter (S) and light output parameter (L), along with other important corrections such as a digital pulser correction, are optimised within this section.

Since the trigger scheme is an absolute voltage crossing the events are not consistently aligned in time. This becomes an issue since the integration gates over the pulse are inconsistent among the pulses. Introducing additional uncertainty in L and S. The t_0 as defined by the trigger, moves as a function of pulse height. Due to the walking of t_0 with pulse height, each event is realigned in time using a digital CFD filter to provide a consistent t_0. This filter is defined in equation 5.1 where v_i is the CFD filtered event sample i, N is the filter length in samples for all events, f is the filter fraction, D is the filter offset and V is the voltage of the raw unfiltered signal, N and D are in either ns or samples as long as the units used are consistent throughout the calculation.

$$v_i = \sum_{j=1}^{N} \left(f V_{i-j} - V_{i-j-D} \right) \tag{5.1}$$

The parameters for the CFD filter were chosen to being:

$$N = 6 \text{ samples} \qquad D = 6 \text{ samples} \qquad f = 0.75 \tag{5.2}$$

These parameters were chosen as these produced a well-shaped bi-polar pulse and were not optimised further within this work. Optimisation of these parameters can be done through splitting a test signal across two channels [99]. A raw and CFD filtered sample pulse can be seen plotted in figure 5.1. The filtered signal is a bipolar pulse and where the zero crossing point provides a consistent way to define a t_0 where $t_0 = t_{cfd} - x_{ns}$, where x_{ns} is an offset in ns. The zero crossing point, t_{cfd}, is calculated through a weighted mean of a point on each side of the crossing. This method to determine t_0 ensures the integration limits, used to determine the parameters L and S, are consistent across events with varying pulse heights.

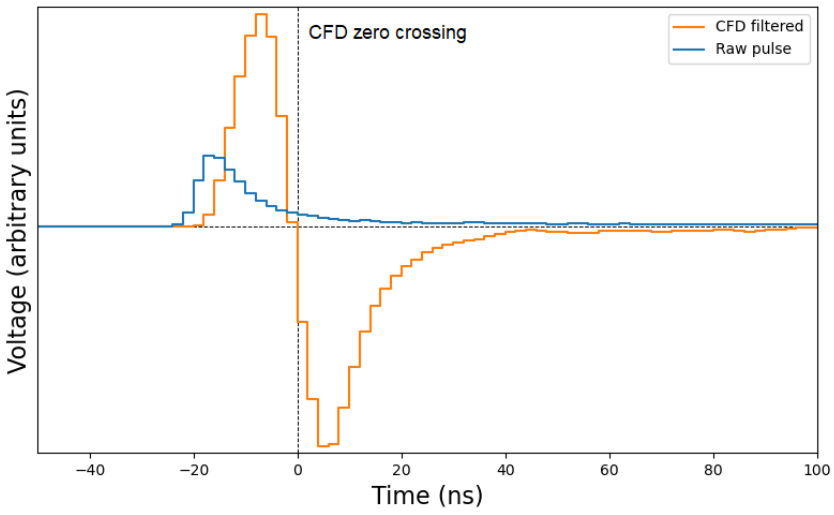

Figure 5.1: Plot of the digitized anode signal before and after the CFD filter has been applied. The zero crossing point t_{cfd}, which is used to align the pulses, is indicated by the dashed line.

5.1.1 Digital Pulser Correction

The digital measurements only utilised the raw anode output from the BC501A, however the dynode remained connected to an analogue pulser correction during acquisition. The analogue pulser correction directly affects the high voltage (HV) power supply to compensate for gain changes through the analogue dynode chain, responsible for producing the analogue light output parameter. With only the raw anode acquired, the HV changing due to the analogue pulser correction resulted in gain differences between measurements of the digital light output parameter. To allow for measurements to be compared, this gain difference was digitally corrected. The method described in this section can be used as a digital pulser correction for any detector that includes an internal LED or pulser requiring post acquisition stabilisation.

The changing gain scales through the different measurements has three main effects if left uncorrected: the edges of the Compton and proton recoil spectra are inconsistent across measurements;

an increase in uncertainty to the MeV_{ee} calibration; and a decrease in the measureable energy resolution.

Applying a single calibration to all the measurements will result in the scale being inconsistent among each other and with the response functions, unless an additional correction faction k_p is applied.

Figure 5.2 shows the digitally measured pulser distributions for the gamma-ray calibration measurements, demonstrating the effects of the dynode pulser correction on the digital light output spectra, as mentioned above. The centroids of the pulser distributions (fig. 5.2) were calculated through a fitted Gaussian function. The centroids occurring at different channels demonstrates the inconsistent gain scale among the calibration measurements.

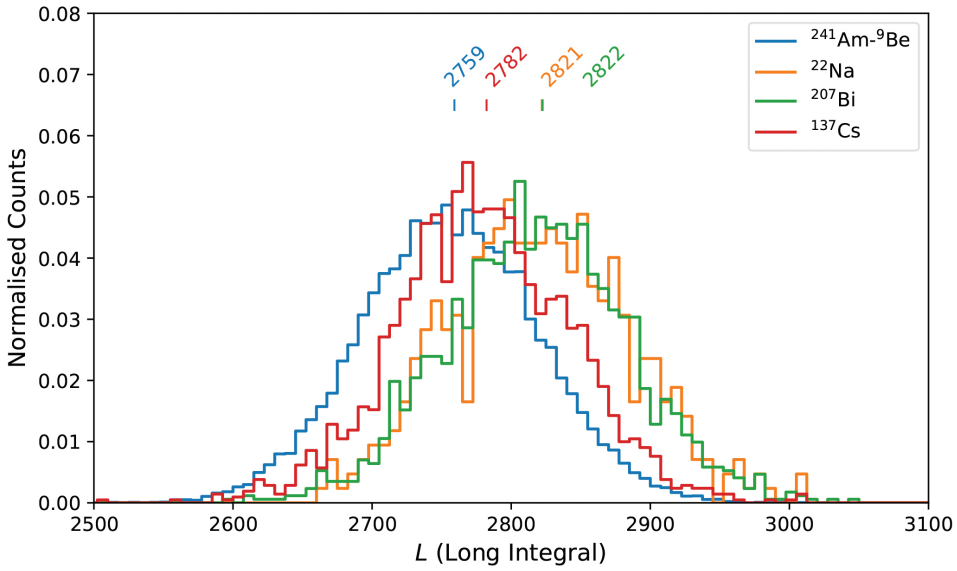

Figure 5.2: Uncalibrated sample light output spectra for the pulser events for different gamma-ray measurements with a long integration limit of 200 ns. The most active sources being the ^{22}Na and ^{207}Bi, with the weakest source being the ^{241}Am-^{9}Be source.

The effects mentioned above are proportional to the intensity of the incident radiation. Figure 5.3 shows the centroid of the pulse distribution as a function of intensity for measurements of a 20.490 MeV neutron field at different beam currents. The error-bars are proportional to $\sigma/\sqrt{N}$ determined from the FWHM and where N is the total number of pulser events. The FWHM was determined through fitting a Gaussian function to the respective distributions, and σ was then taken to being equal to $FWHM/2\sqrt{2\ln 2}$.

The digital gain correction, k_p, was used to align all the pulser distributions through a linear gain scaling factor applied each data set, however, this method does not correct for the decrease in energy resolution introduced into the data. The pulser distributions were matched to centroid value

of 3850, by applying a digital gain factor within the acquisition software, QtDAQ. The software had internal limits on the resolution of the gain factor of 0.01 fixing the precision gain correction through this method.

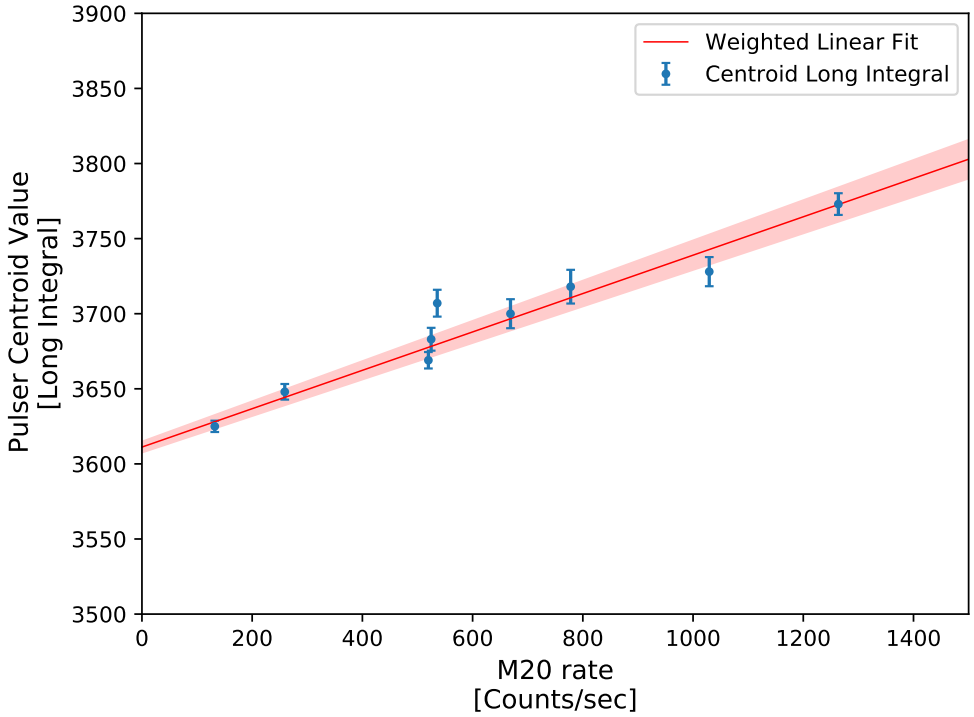

Figure 5.3: Centroid of the pulser distribution for the different intensity measurements made with the 20.490 MeV neutron field. The monitor (M20) rate has been used as being proportional to the intensity of the beam. The linear fit returned a gradient value of 0.1278(62) longint sec counts^{-1} with an intercept of 3611.2(35) longint.

The correction factors, the resultant centroid and FWHM values for the pulser distribution along with the uncorrected pulser centroid and FWHM values for the gamma-ray calibration sources are presented in table 5.1. The corrections applied to each of the digital data sets can be found in table C.1 in appendix C.

Table 5.1: The pulser centroid values along with the FWHM of the pulser distribution, before and after correction k_p is applied, for the gamma-ray calibration measurements.

Source	k_p	Uncorrected		Corrected	
		Centroid (ch)	FWHM (ch)	Centroid (ch)	FWHM (ch)
^{241}Am-^{9}Be	1.02(1)	3765(2)	196.0(1)	3840(2)	200.0(1)
^{207}Bi	0.99(1)	3877(3)	210.6(2)	3873(2)	211.3(2)
^{22}Na	0.99(1)	3875(3)	231.8(3)	3875(3)	231.8(4)
^{137}Cs	1.01(1)	3816(2)	205.1(2)	3819(2)	205.1(2)

5.1.2 Pulse Shape Parameter Optimisation

The digital light output and pulse shape parameters, L and S, have been defined in equation 2.7 in chapter 2 as a digital long integral and through a digitally implemented charge comparison respectively. The optimal short integration time t_s used to determine the pulse shape parameter, S, was found by maximising the separation in the gamma-ray and neutron loci in the distribution of S as a function of L. The separation of these Gaussian distributed loci is defined by the Figure-of-Merit (FoM). Equation 5.3 provides a definition for the FoM quantity where $\mu_{p/e}$ refers to the centroid value of the proton and electron loci respectively and $\text{FWHM}_{p/e}$ refers to the associated full width half maximum of the distribution. Loci with a FoM below one are considered inseparable and values above 2 are considered to have excellent separation.

$$FoM = \frac{|\mu_p - \mu_e|}{\text{FWHM}_p + \text{FWHM}_e} \tag{5.3}$$

The counts as a function of the digitally defined S and L for a 2000 µg cm^{-2} TiD target with 1.84 MeV protons have been plotted in figure 5.4a. A slice along the light output axis for values between 1.4 MeV$_{ee}$ $\leq L <$ 1.6 MeVee, as indicated on figure 5.4a, has been projected onto the pulse shape axis in figure 5.4b. The parameters used in the FoM calculation are indicated.

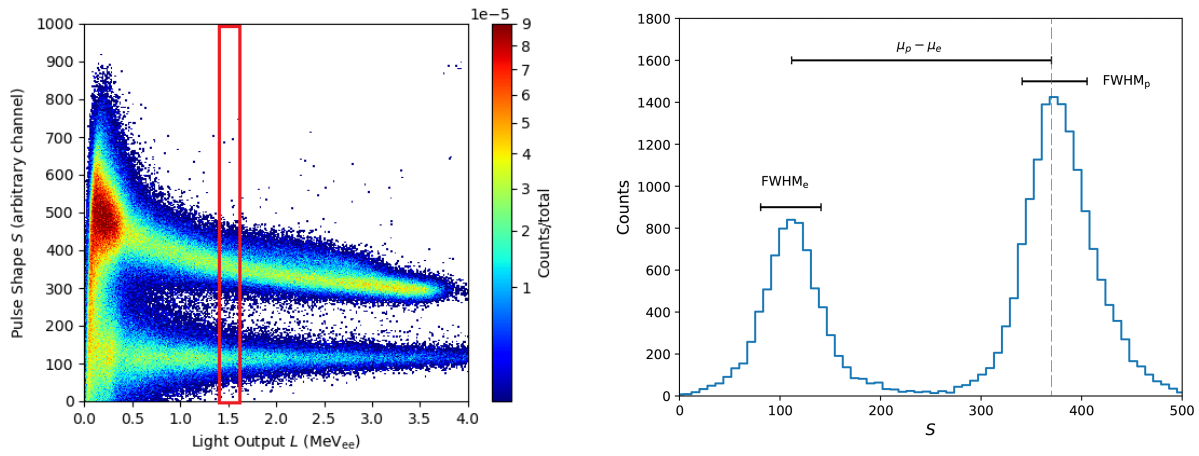

(a) **(b)**

Figure 5.4: (a) Events as a function of S and L as measured with a BC501A for the standard intensity, 7.000 MeV neutron field. The slice indicated by the red outline marks from $L = 1.4$ MeV$_{ee}$ to 1.6 MeV$_{ee}$ (b) The slice indicated in (a) projected onto the S-axis, with the indicated parameters used to calculate the FoM.

For a given long integration time, careful choice of short integration time can maximise separation between neutron and gamma-ray incident events. Consider the extremes of a choice of short integration time destroys the ability to separate pulses: a short integration time chosen within the rising edge of the pulse would not capture enough information about the pulse, loosing the ability to discern the particle type; for a short integration time close to that of the long integration time the short integral value would tend towards the long integral value and the charge comparison would return a value close to one for all events regardless of incident radiation type. Considering the value of the FoM as a function of short integration time is then a direct way to produce optimal separation through the charge comparison method. Figure 5.5 shows the FoM calculated for several intervals of light output for short integration times between 20 ns and 500 ns, for the 7.000 MeV neutron measurement and a given long integration value of 500 ns. The start of the integrals t_0 is defined as 25 ns prior to the CFD zero crossing point t_{cfd} ($x_{ns} = 25$ ns). From figure 5.5 the optimal integration time for the short integral is 30 ns for a long integration time of 500 ns. All further analyses were completed using the optimised short integration time of 30 ns.

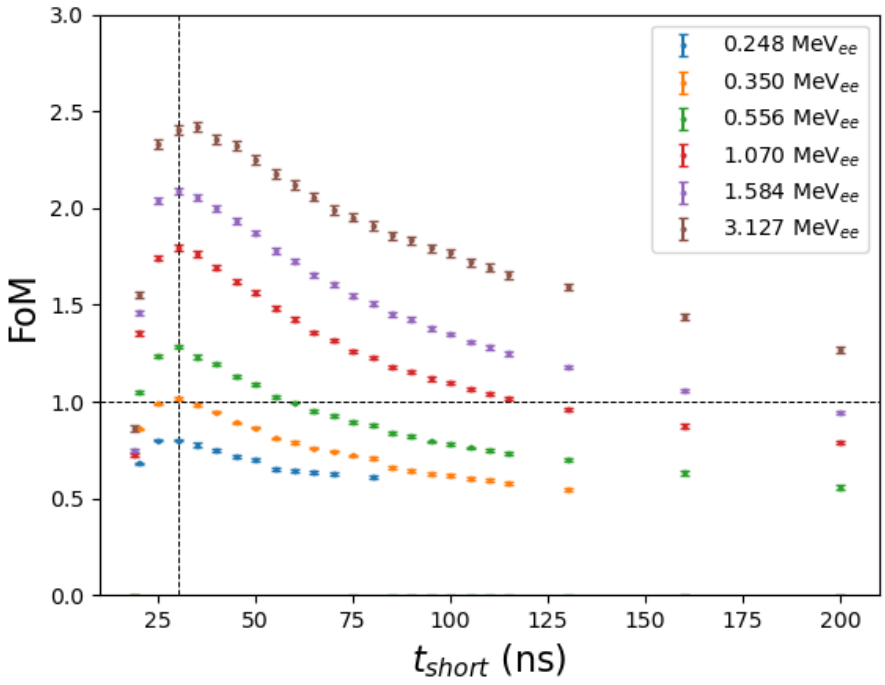

Figure 5.5: Figure-of-Merit values as a function of the length (ns) of the short integration time, for different intervals of light output, used in the digital charge comparison method to determine the pulse shape parameter S. The long integral bound was kept to 500 ns for all short integral optimisation. The maximum FoM, across the light output intervals plotted, is 30 ns. The light output values in the legend are the midpoint of an interval with a with of 0.102 MeV$_{ee}$.

5.1.3 The light output parameter

Acquiring only raw anode data from the BC501A introduces some effects which need to be taken into consideration. A subtle issue arises from the choice of the long integral in the definition of the digital light output parameter.

In traditional analogue electronics systems the analysis of the pulses to measure L typically use a charge sensitive pre-amplifier (CSP) in conjunction with an amplifier [13]. The CSP integrates the current pulse using a capacitor converting the collected charge into a voltage amplitude, to avoid charge saturation the capacitor is often discharged using a resistor. After this integration the information of the energy deposited in the detector is carried in the amplitude of the pulse. The critical parameter in these systems is the total capacitance in the system. The greater the capacitance the smaller the signal-to-noise ratio (SNR) [110].

The digital equivalent is to digitally integrate or sum the raw anode voltage samples over the determined lengths for the different integrals. The current pulse, sampled across a resistor, is digitally integrated. The integrated voltage pulse is still proportional to the energy deposited in the detector [13]. The longer the window of integration the greater percentage of pile up events and decreasing the SNR due to the portion of the window where the noise is dominant.

A consequence of the choice of the digital long gate arises due to the different pulse shapes produced by the interaction of neutrons and gamma-rays. Consider the pulses in figure 5.6.

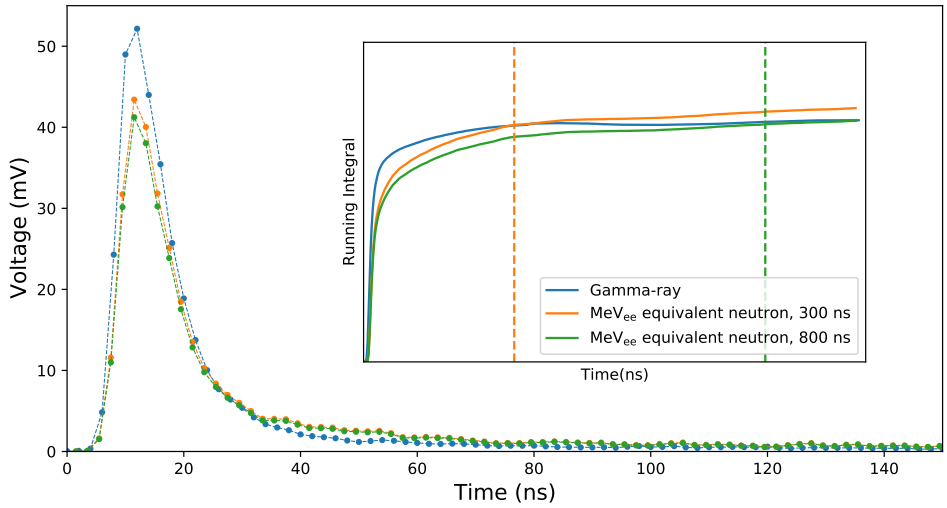

Figure 5.6: Sample pulses of a gamma-ray and two different neutrons as measured from the anode output from the BC501A detector with the DT5730 digitiser. The neutron pulses produce the same $\mathrm{MeV_{ee}}$ value as the gamma-ray pulse for two different long gate choices, 300 ns and 800 ns. The inset axis shows the cumulative integral for the different pulses. The dashed lines have been included to guide the eye.

The two neutron pulses shown plotted have the same calibrated MeV_{ee} value (shown in the inset axes in figure 5.6) as the gamma-ray pulse with the difference being the choice of long gate. The relationship between the gamma-ray and neutron L scales change as a function of long gate, which directly affects the results one would get from unfolding a MeV_{ee} calibrated neutron light output spectrum.

This presents an issue for the digital data taken at AMANDE in this measurement campaign since the only information acquired was for the raw anode of the BC501A detector. The MeV_{ee} calibration for the light output scale demonstrates this problem and is seen in figure 5.7. The proton recoil edge associated with the neutron events agree with the gamma-ray calibration line for the analogue system however for the digital measurements the proton recoil edge occurs below the gamma-ray calibration line.

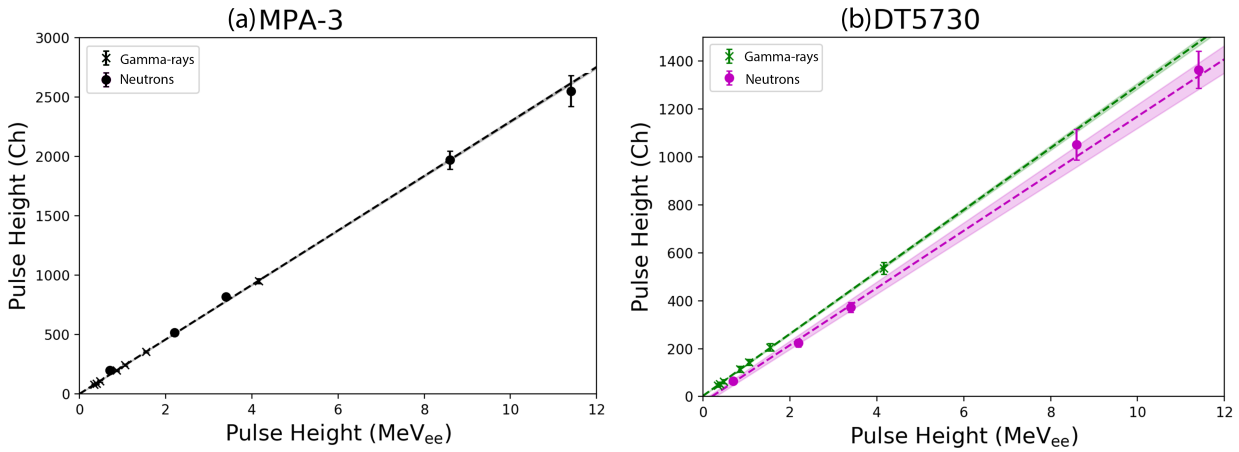

Figure 5.7: The calibration curves for the analogue (a) and the digital for a long gate choice of 400 ns (b) acquisition systems. The neutron edges have been included with their expected edge location obtained through the response functions.

The disagreement of the proton recoil edge of the mono-energetic neutron light output spectra with the gamma-ray calibration occurs due to a difference in the relationship between the measured gamma-ray and neutron light output spectra in comparison to the one encoded in the response functions for the detector. The response functions for the detector are simulated but include parameters which are calibrated empirically, these empirical calibrations were performed using the standard analogue acquisition system. The expected MeV_{ee} values for the edges of the measured neutron line shapes were obtained through the response functions.

With no other additional information than the anode, one way to ensure alignment with the expected relationship in the response functions is to select a long gate that produces this behaviour. This choice is determined through prior knowledge of the incident neutron energy and choosing the long integral that produces the scale in the response functions.

Selecting a long gate to ensure alignment is only applicable in situation where there is a measurement of a known neutron radiation field. Methods for long gate choice without requiring prior knowledge of the neutron radiation field are discussed in chapter 6.

For the measurements presented in this section the long gate choice was determined by selecting the long gate that produces the same MeV_{ee} scale for the neutrons as in the response functions. This was determined using the 7.000 MeV neutron field with a beam current of 0.6 µA. The long integral value which produces the best agreement between the locations of the measured proton recoil light output edge for the two acquisition systems is the selected as the integral length for the analysis of all the digital measurements with anode only information. Figure 5.8 shows this difference as a function of long gate (ns). The long integration time used for the analyses in this chapter was chosen to be 500 ns which produces the best agreement in the digitally measured neutron MeV_{ee} scale to the response functions.

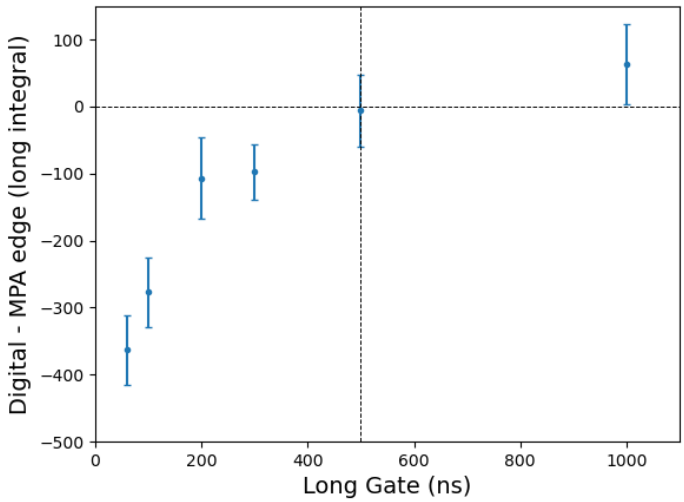

Figure 5.8: The difference between the edge of the 7.000 MeV neutron light output spectra for the analogue and digital acquisition systems as a function of long gate.

5.2 Standard Intensity Measurements

5.2.1 The Measurements

The measurements for made with the BC501A detector across the neutron energy range of 1.200 MeV to 20.490 MeV. A summary of the measurements taken can be found in chapter 3 table 3.1. Figure 5.9 shows the counts as a function of light output parameter, L, and pulse shape parameter, S, for the standard intensity measurements over the neutron energy range of 1.200 MeV to 20.490 MeV. The counts have been normalised to an integral of unity for comparison purposes.

The distribution of the counts in figure 5.9 demonstrate the same features attributed to the different interactions of neutrons and gamma-rays in the detector as in the analogue measurements (fig 4.2) for the same beam conditions.

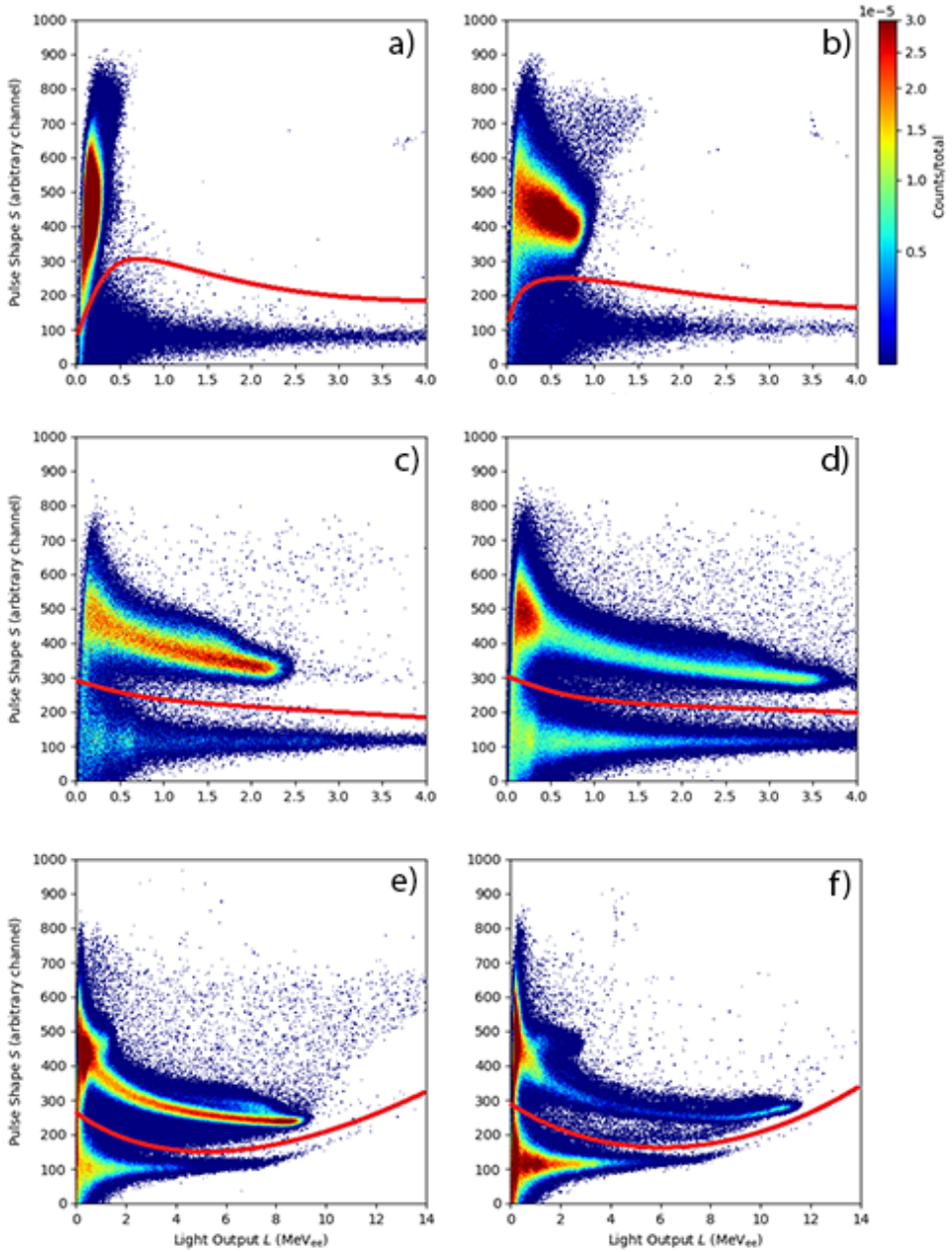

Figure 5.9: Scaled counts as a function of L and S for the standard intensity measurements as summarised in table 3.1 for the digitally measured neutron beams of (a) 1.200 MeV; (b) 2.500 MeV; (c) 5.000 MeV; (d) 7.000 MeV; (e) 15.100 MeV and (f) 20.490 MeV. The counts are normalised to a unity integral. The red line indicates the cut applied to this data to select for the neutron induced events.

The method by which the neutron events were isolated follows the same procedure as for the analogue measurements (section 4.1). Slices along the light output were taken and the point of minimum between the neutron and gamma-ray distributions was used at the best cut point for that region. This was then applied to all the slices along the L-axis. A cubic spline is then taken of all these points to make a function to cut across all channels.

All measurements were made with the gain range of 2.0 V_{pp} for the digitiser input. Figure 5.9(e) and (f) show evidence of light output saturation, where the amplitude of the pulse exceeds the maximum acceptable input voltage. The light output saturation occurs at approximately 8 MeV_{ee} for the electron recoil locus and 8.5 MeV_{ee} for the proton recoil locus. Light output saturation causes distortion in the measured light output spectra compressing the spectrum above the saturation point. The distortion to the light output spectra results in an disagreement with the associated response function.

The pulse pile up effects take on a slightly different structure to the pile up events in the analogue measurements. Correcting for pile up events and digital dead time will be discussed further in sections 5.3.1 and 5.3.2 respectively.

The measurements for the neutron energies of 1.200 MeV, 2.500 MeV, 5.000 MeV and 7.000 MeV are analysed further. The neutron light output spectra for the standard intensity measurements of the above mentioned neutron energies have been plotted in figure 5.10. The overall shape and edge behave as expected with increasing neutron energy.

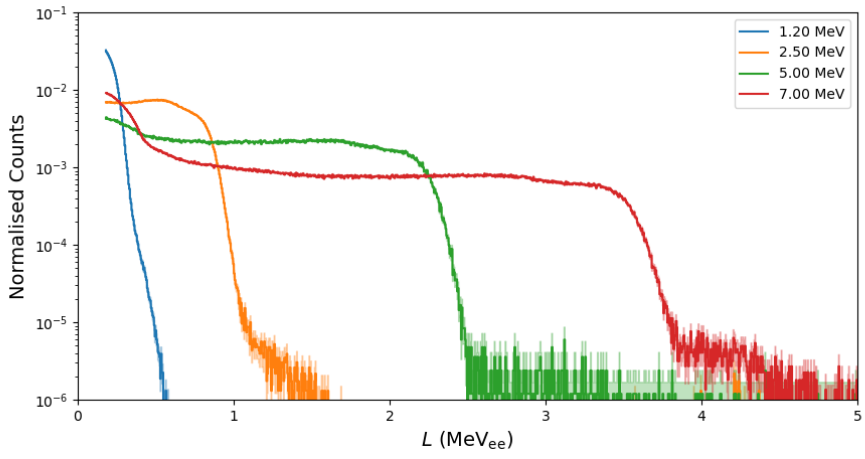

Figure 5.10: Neutron light output spectra for the measurements made at standard beam intensities for neutrons fields with a calculated nominal peak energy of 1.200 MeV, 2.500 MeV, 5.000 MeV and 7.000 MeV as selected by the cuts illustrated in figure 5.9. The counts are scaled to an integral of unity for comparison. The uncertainties due to the cuts and Poisson statistics have been included for each light output spectra as the lighter shading.

5.3 Correction Factors

5.3.1 Pile up

The form of the digital pile up differs to the analogue equivalent measurement due to the different ways of determining the pulse shape parameter, refer to figure 5.11 for a sample PSD plot indicating the cut used to select for the pile up events. Pile up events affect both the L and S. Without more detailed analysis on the individual pulses within a pile up event the type radiation causing the event of the pulses are not distinguishable. Pile up gamma-ray pulses are therefore unable to be excluded from the neutron light output spectra.

With a pile up event always having an increased L value this can change the S parameter in several ways. The increased L results in reduced S values if the second event occurs outside of the short integral window, figure 5.12a. In this case, the S value will be increased proportional to the integral of the second pulse. If the second pulse occurs within the window of the short integral (figure 5.12(b)) this results in the value of S being closer to the expected value since it increases in a similar proportion to the long integral. The events with the second pulse within the short integral window occur above the edge of the proton recoil locus but at the correct S value, as indicated in figure 5.11.

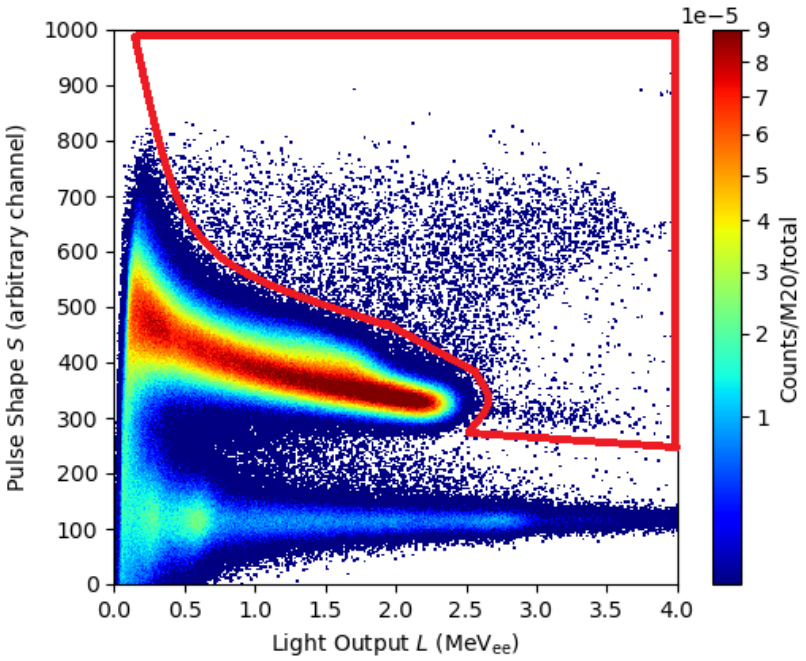

Figure 5.11: Sample PSD plot with the region outlined in red representing the area used to quantify the number of pile up events.

The QtDAQ software is configured such that only the largest pulse in the acquired window is analysed resulting in a another contribution to the counts that occur to the higher L values at the same pulse shape value as the edge of the proton recoil locus. If two events occur but the second has a larger light output then the value of S will not be affected significantly but the affected pulses will have a slightly increased L value, depending on how much of the tail of the previous pulse occurs within the analysis window for the larger pulse, figure 5.12(b) shows a sample event with some of the previous events tail within the short integral window.

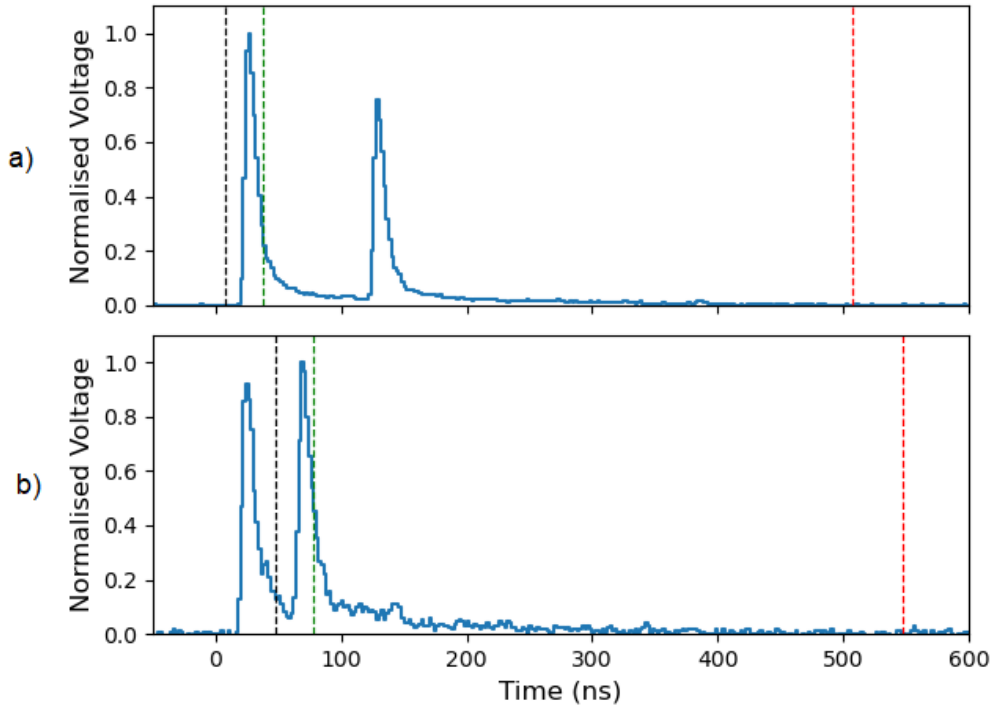

Figure 5.12: (a) Pile up event in which the second pulse occurs only within the long integral window of the main pulse, increasing the L and S parameters proportionally to the area and the inverse of the area of the second pulse respectively. (b) QtDAQ analyses the largest pulse in the case of pile up events, in the case plotted there will be minimal affect to the S value but a slight increase in the L parameter. The three limits for the two integrals (t_0, t_{short} and t_{long}) have been included in both plots as the black, green and red dashed lines respectively.

Digital pile up affects the neutron line shape with a shift of events to higher L values, as shown in figure 5.13 for 1.84 MeV deuteron beam incident on a TiD target producing 5.000 MeV neutrons with a beam current of 2.57 µA. Figure 5.13(c) show that these pile up events affect the spectra up to 0.26% in individual channels and that the shift to higher L values is exponential between around 1.6 MeV_{ee} tp 2.2 MeV_{ee}, corresponding with the edge of the neutron light output spectrum. In the region of the proton recoil edge the pile up events quickly become dominant due to the decreasing statistics.

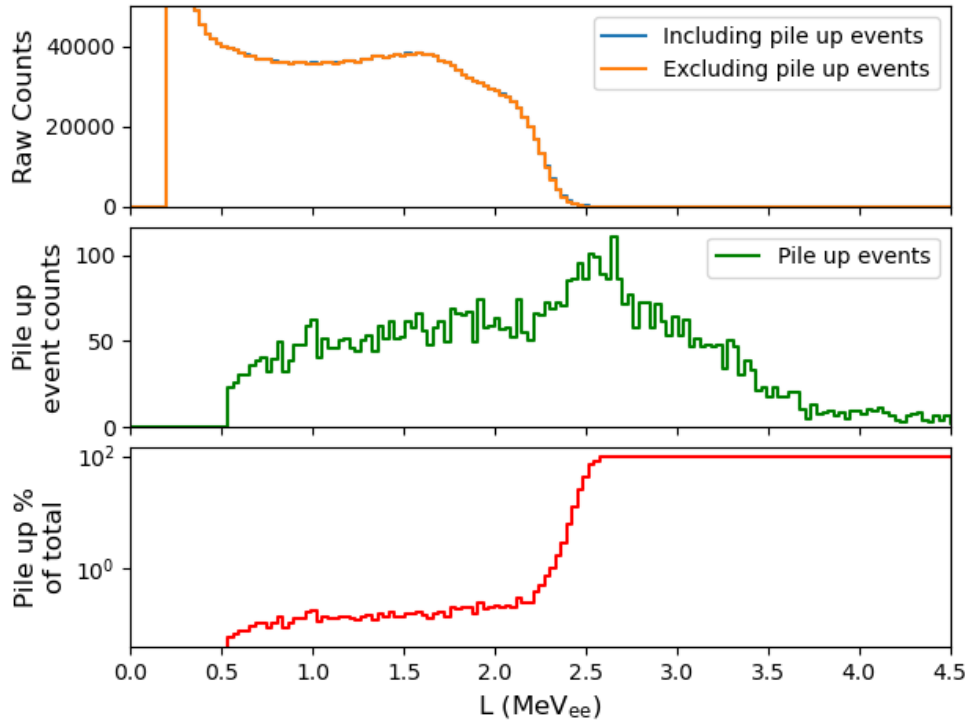

Figure 5.13: (a) Neutron light output spectra with and without pile up events unscaled for the highest intensity run of the 5.000 MeV neutron beam, (b) The pile up events extracted from the pile up regions in pulse shape discrimination plot, along with the percentage that pile up events represent in the neutron light output spectra (c). The percentage is calculated through the ratio of pile up event to the total events.

The correction factor for pile up events, k_{PU}, was calculated as the proportion of events occurring at higher S and L values from the neutron distribution (N_{pu}), as indicated in figure 5.11, to the number of the total events in the neutron light output spectra (N_{tot}) as shown in equation 5.4. This correction is then applied as an additional scaling factor as shown in section 5.3.5.

$$k_{PU} = \frac{N_{tot}}{N_{tot} - N_{pu}} \tag{5.4}$$

The associated uncertainty in k_{PU} is then defined as:

$$u\left(k_{PU}\right) = k_{PU}\sqrt{\left[\frac{u(N_{tot})}{N_{tot}}\right]^2 + \left[\frac{\sqrt{u(N_{tot})^2 + u(N_{pu})^2}}{N_{tot} - N_{pu}}\right]^2}. \tag{5.5}$$

5.3.2 Buffer Saturation Correction

As detailed in section 3.1.4, events are acquired into a set of circular buffers on board in the digitiser unit. When one buffer is full it is locked, preventing overwriting of events and is read out when the desired number of events per block transfer is obtained. If the buffers fill up faster than they are able to be read out, then once all the buffers are full the digitiser will not be able to acquire any events until events have been read out. The dead time associated with the acquisition pausing due to buffer saturation is non-paralysable and can be regarded as a type of saturation, without any appreciable dead time between consecutive events within a single memory buffer as in traditional dead time models. These losses can be minimised by selecting for the minimum acceptable event size and to optimize the number of events that can be read out at a time.

Before buffer saturation any triggers that occur out of an acquired event window will be acquired without any dead time. Triggers occurring within the window of another event will not be acquired as a separate event and these events are recorded as pile up events.

The degree of buffer saturation is dependent on the read out speed, frequency of read out, event size, number of events read out in one block transfer and rate of incoming events. Event size and number of events read out in one block transfer are both controllable parameters through the software and can be optimized to minimize buffer saturation during high intensity runs. The read out speed is limited by the mode of communication from the digitiser to the PC, being either an optical link (80 MB/s) or a USB (30 MB/s) connection. The frequency of read out depends on the frequency of incoming events and is not software controllable.

The digitiser samples at a rate of 500 MS/s, with 14 bit voltage resolution, resulting in a sustained data rate of near 1 GB/s as shown below.

$$\begin{aligned} 500\ \text{MS/s} \times 14\ \text{bit/s} &= 7000\ \text{Mbit/s} \\ \frac{7000\ \text{Mbit/s}}{8\ \text{bit/byte}} &= 875\ \text{Mbytes/s}, \end{aligned}$$

with the additional overhead for header and timing information ≈ 1 Gbytes/s. The maximum event rate before buffer saturation is then determined by the event size.

The measured count rate using the digitiser has been plotted against the monitor (M100) rate for three different sample lengths chosen in figure 5.14. The chosen sample lengths of 256, 512 and 1024 samples saturate at rates of around 34500, 19500 , and 10000 counts s^{-1}, with decreasing sample size.

Buffer saturation is clearly evident in figure 5.15 which present a sample section of the events as a function of time for both an (a) unsaturated and a (b) partially saturated data set.

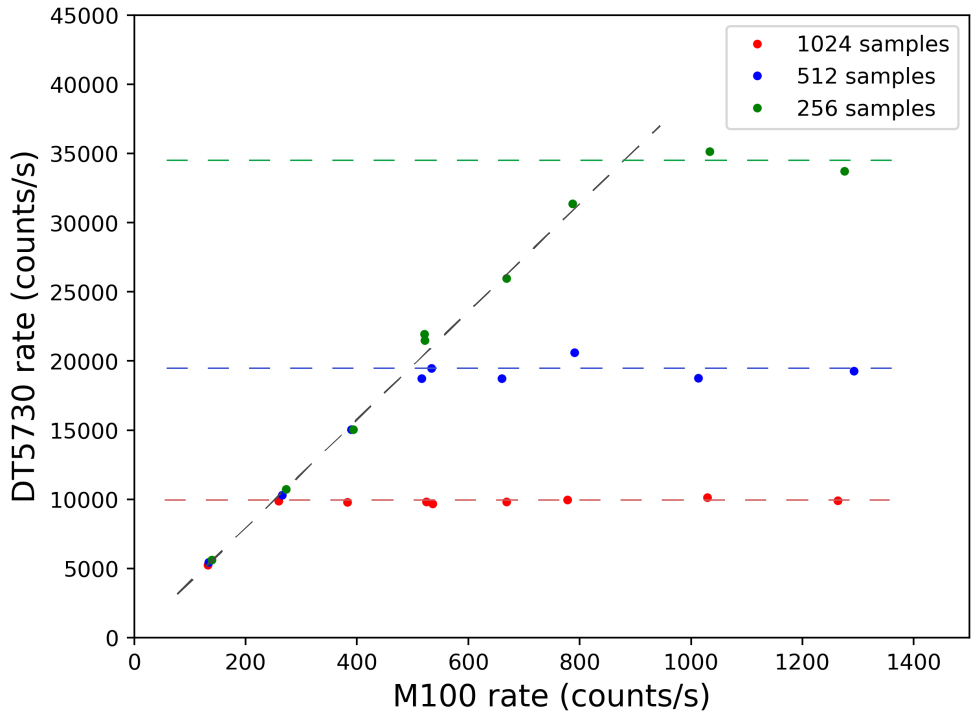

Figure 5.14: Plot of the digitiser acquired rate against the associated monitor rate for varying intensity neutron beams. Three different sample sizes are shown, indicating the effect of sample size with respect to the point at which the buffers become saturated.

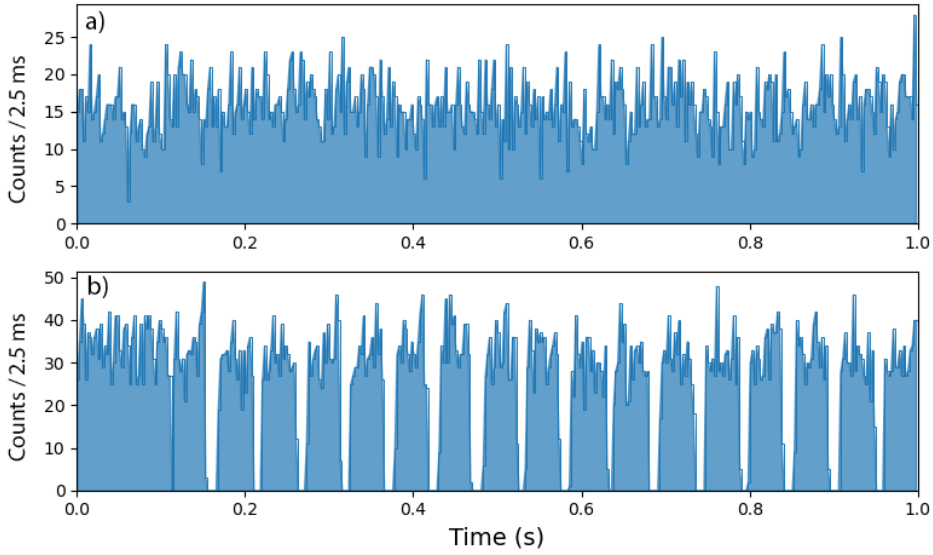

Figure 5.15: Events as function of time for an (a) unsaturated and a (b) partially saturated data set. There are well defined sections of zero acquisition seen in the saturated data set, corresponding to the buffers being full and the read out time for the designated number of events.

The histogram of time-between-events for the unsaturated case is expected to be exponential in form due to the Poisson distribution in the events, as seen in figure 5.16(a). The saturated data set will lose a proportion of the events closely positioned to each other in time within the buffer read out period as can be seen in figure 5.16(b). Additionally, there will be a Gaussian distributed peak associated with the time taken for read out to occur. The higher the intensity, the more saturated the digitiser, the less scatter in the Gaussian distribution. The scatter in the distribution associated with the events occurring after a buffer read out is due to the scatter in time between events, at higher intensities this scatter reduces and the distribution becomes dominated by the read out time.

Figure 5.16(a) shows a frequency histogram for the time between consecutive events (Δt) occurring within a buffer / within consecutive buffers that have not saturated. Note that the vertical axis is a log scale and hence that the form of the histogram is exponential as expected for a Poisson distributed source of events. The period of the exponential (gradient in the lin-log scale shown) is inversely proportional to the average event rate. Figure 5.16(b) illustrates the same histogram for a saturated data set, note that the time axis is greatly extended compared to the previous figure. At low Δt, as with 5.16(a) and shown in the inset, the distribution is exponential in form demonstrating the same behaviour as in the unsaturated case. These data occur within the buffer read period where there is near-zero dead time and events are recorded correctly as expected.

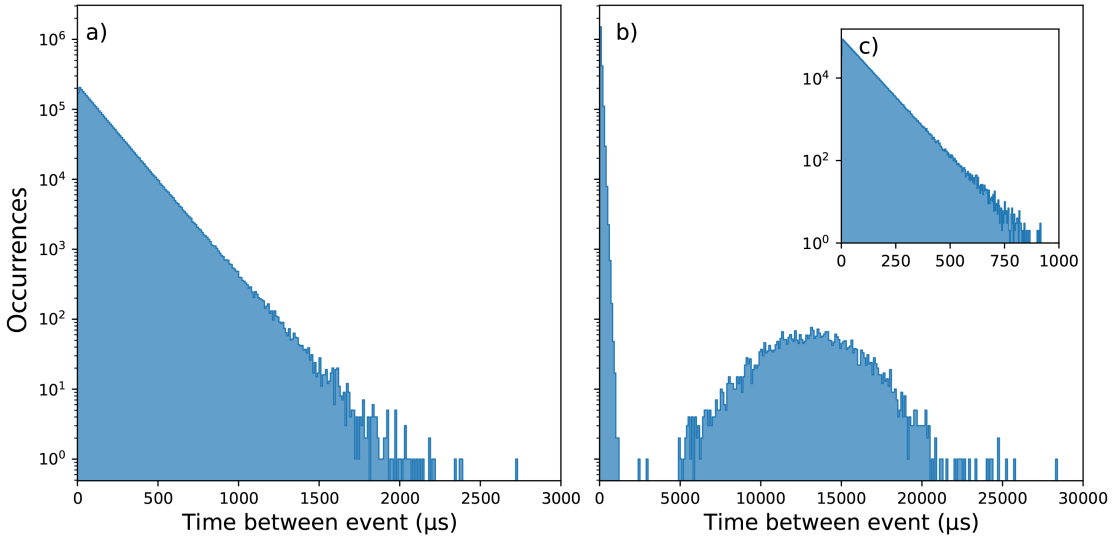

Figure 5.16: The number of occurrences as a function of time between events in µs for the (a) unsaturated 7.000 MeV data set and (b) higher intensity 7.000 MeV measurement which required buffer saturation correction. (c) A zoomed in section of (b) showing the Poisson distributed section of the data.

At long Δt, additional events are observed in the histogram forming a Gaussian type peak with an centroid Δt, in this case, of 14 ms. These events are transposed to large Δt as a result of the buffer saturation, and represent the time difference between the last event in a successfully readout

buffer, and the next event recorded following a saturation delay. Thus the centroid value is a linear combination of the average saturation readout delay (large) plus the time to first event following acquisition start being enabled once again (small).

There is a secondary dead time effect to take into consideration, at the higher intensities there is a loss of events with small time between events. This additional loss can be seen in the highest intensity 7.000 MeV measurements. Unlike figure 5.16 the highest intensity measurement shows a change to the Poisson distribution of the counts, refer to figure 5.17. The source of these additional losses are still under investigation.

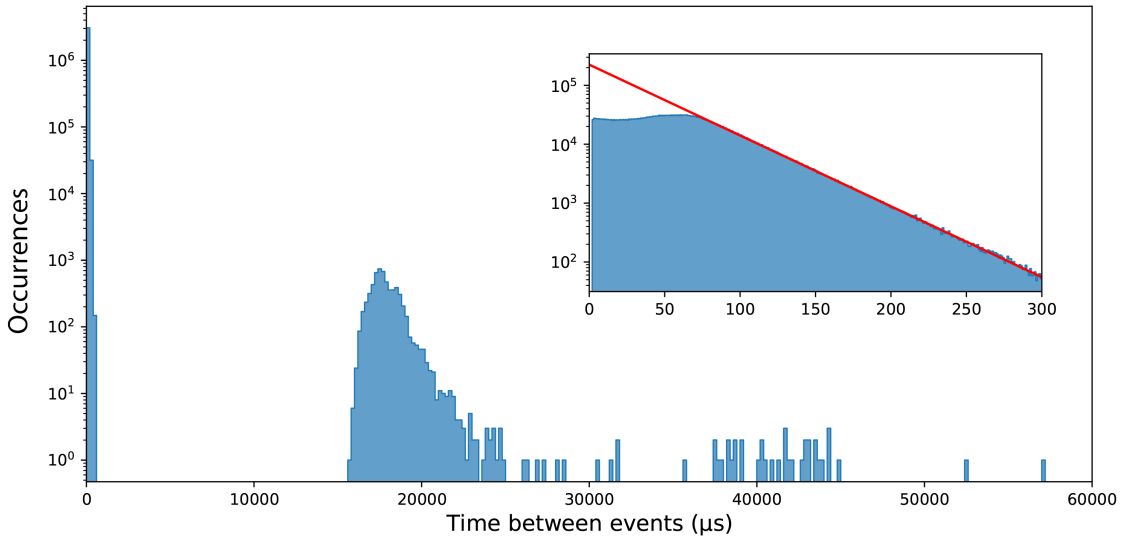

Figure 5.17: Counts as a function of time between events in µs for the highest intensity 7.000 MeV measurement. Unlike the saturated data set in figure 5.16 there is an addition loss of events which can be seen in the deviation from the Poisson distribution at very small time between events, in the inset axis.

To correct fully for the digital buffer saturation (k_S), one must correct for both saturation effects shown. One approach to this is to use the time between events distribution to correct for both. Summing the events in the distribution attributed to the buffer read out freeze period, weighted by their time, produces the total time that the digitiser was frozen and unable to acquire any events (t_{sat}). Using this time we define k_{buf} as the proportion of the live time (the total acquisition time less the time that the buffers were all saturated) to the total acquisition time (t_{tot}), as shown in equation 5.6.

$$k_{buf} = \frac{t_{tot}}{t_{tot} - t_{sat}} \tag{5.6}$$

In the case of extreme buffer saturation the secondary saturation effect should be corrected for with an additional scaling factor $k_{\Delta t}$, which is demonstrated in figure 5.17 in the inset axes. This can be corrected by calculating the proportion of missing events from the deviation from the Poisson distribution. This correction factor is currently not well understood and requires further investigation.

The raw, buffer corrected (k_{buf}) and additional missing counts at low Δt corrected ($k_{buf}k_{\Delta t}$) count rates measured by the digitiser have been plotted against the monitor count rate in figure 5.18 for each of the different acquisition window sizes; (a) 1024, (b) 512 and (c) 256 samples. The low intensity measured count rates were used to determine the linear fit (black dashed line in the figure) representing the proportionality of the two quantities in the case of insignificant dead time effects.

The correction factor for buffer saturation occurring at large Δt (k_{buf}) corrects for the data sets where there is little to no events lost at low Δt, and produces a higher saturation point. The higher the intensity the greater loss of events at low Δt. The correction factor $k_{\Delta t}$ is not correcting for the lost events entirely. In figure 5.18a at the extreme intensities $k_{\Delta t}$ produces inconsistent behaviour and the resultant corrected count rates being much larger than expected. For the other two acquisition window lengths, shown in figure 5.18b and c $k_{\Delta t}$ appears to be under correcting, implying additional effect which has not been corrected for.

Since the $k_{\Delta t}$ correction factor produces inconsistent behaviour the results presented for the rest of the chapter only include the correction factors k_{buf} and k_S.

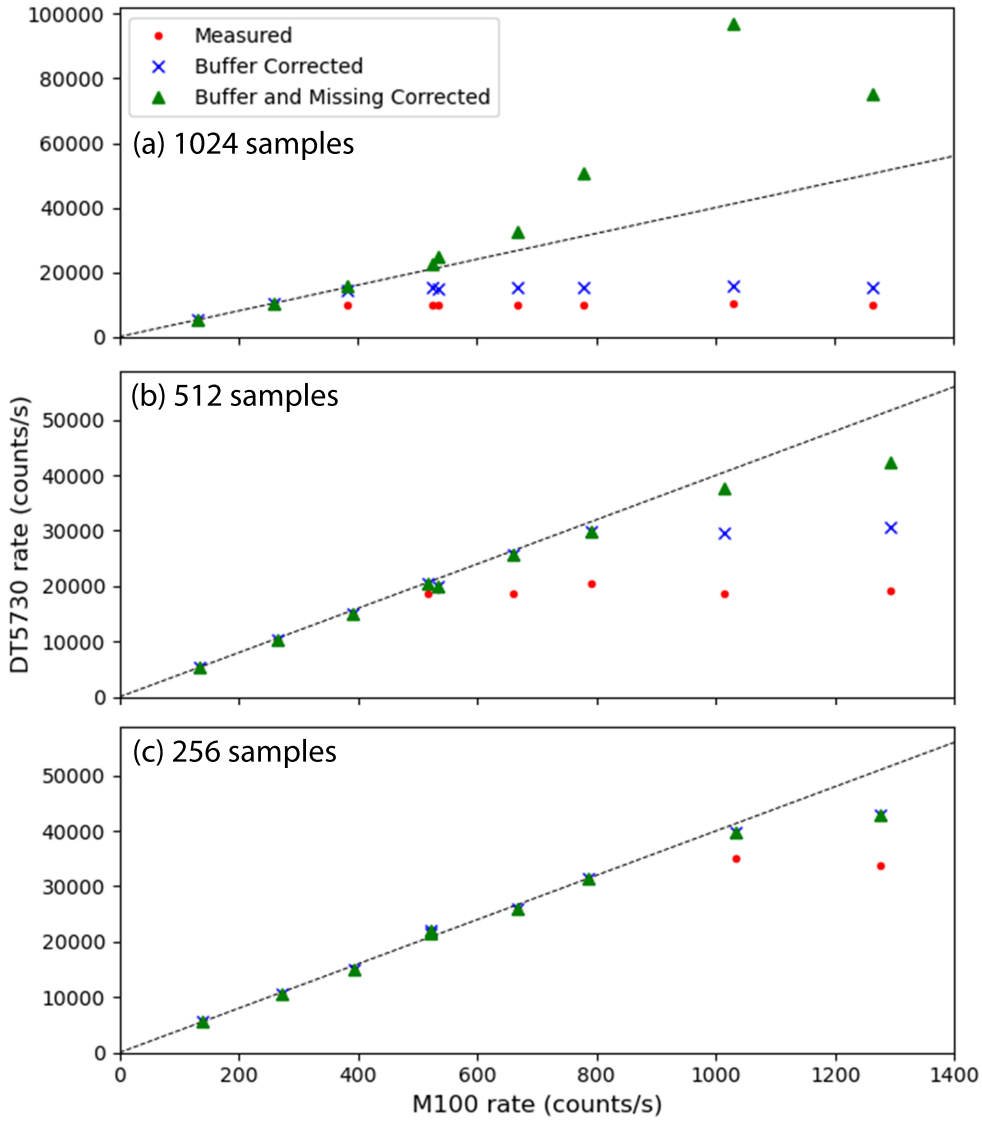

Figure 5.18: Plot of the digitiser acquired rate against the associated monitor rate for varying intensity neutron beams for the measured rates, R (●), the buffer saturated corrected rates, $k_{buff}R$ (×) and the corrected for the additionally missing counts at low Δt, $k_{buff}k_{\Delta t}R$ (▲) for the three different sample sizes; (a) 1024, (b) 512 and (c) 256. The fitted line represents the line of $y = 24x + 7300$ representing the proportionality at low intensities when dead time factors are negligible.

5.3.3 Unfolding

The neutron spectra in figure 5.10 were unfolded through the same two-stage unfolding process as the analogue measurements. The final unfolded neutron spectra all had solutions with a reduced χ^2 value of under 4.0. Figure 5.19 shows the measured and refolded fitted light output neutron spectra for the four standard intensity measurements. There is good agreement for the four measured spectra. As was seen in the refolded spectrum of the MPA 2.500 MeV neutron measurement (figure 4.5(b)) there is an small deviation from the measured light output spectrum at around 0.3 MeV_{ee} which is not physical.

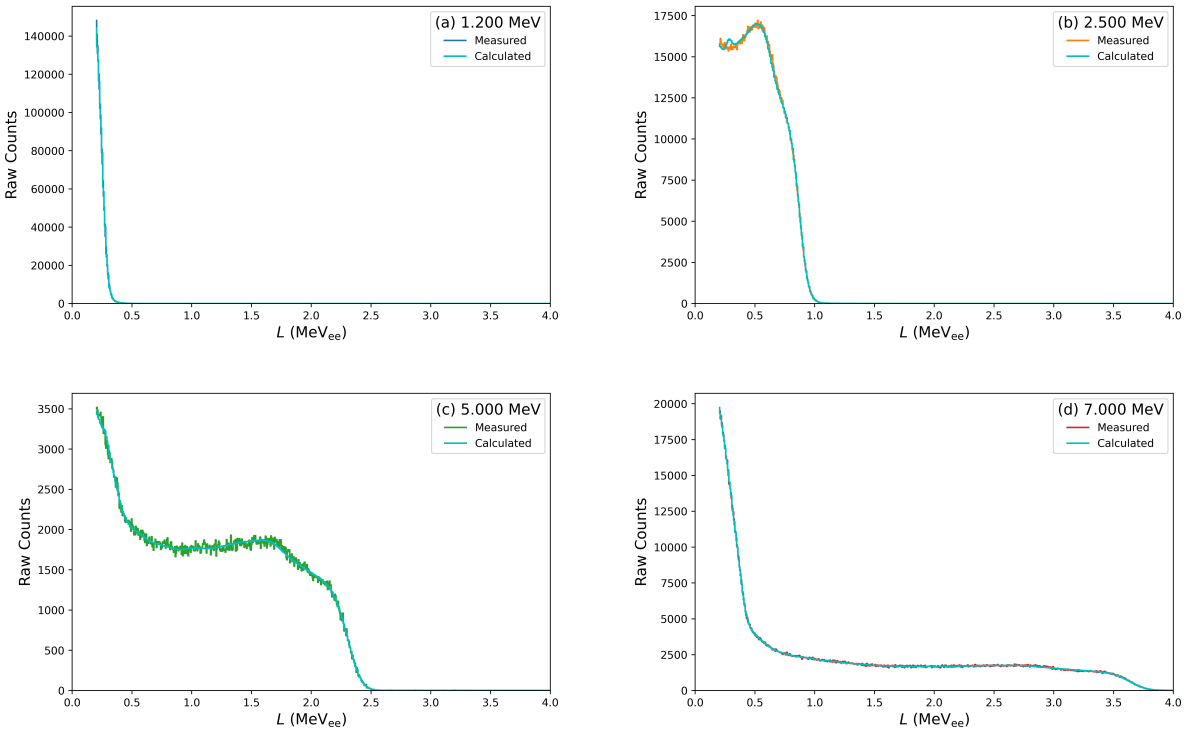

Figure 5.19: Neutron light output spectra measured with the digital acquisition system for four neutron fields with nominal energies of (a) 1.200 MeV; (b) 2.500 MeV; (c) 5.000 MeV and (d) 7.000 MeV for the standard intensities. The refolded light output spectra from the unfolding calculations have been included as the light blue line in each of the plots.

The resultant unfolded neutron energy spectra, Φ_E, for the standard intensity measurements have been plotted in figure 5.20. Other than the primary peak, there are the expected secondary lower energy peaks attributed to secondary reaction channels with carbon and oxygen in the TiT target [108]. For the 1.200 MeV measurement the unfolded spectra showed significant asymmetry in the primary peak, this has been attributed to the neutron edge for this measurement being close to the threshold on the measurements making it difficult to unfold the measurement. The asymmetry in the peaks for the 2.500 MeV, 5.000 MeV and 7.000 MeV measurements are attributed to energy

loss within the target.

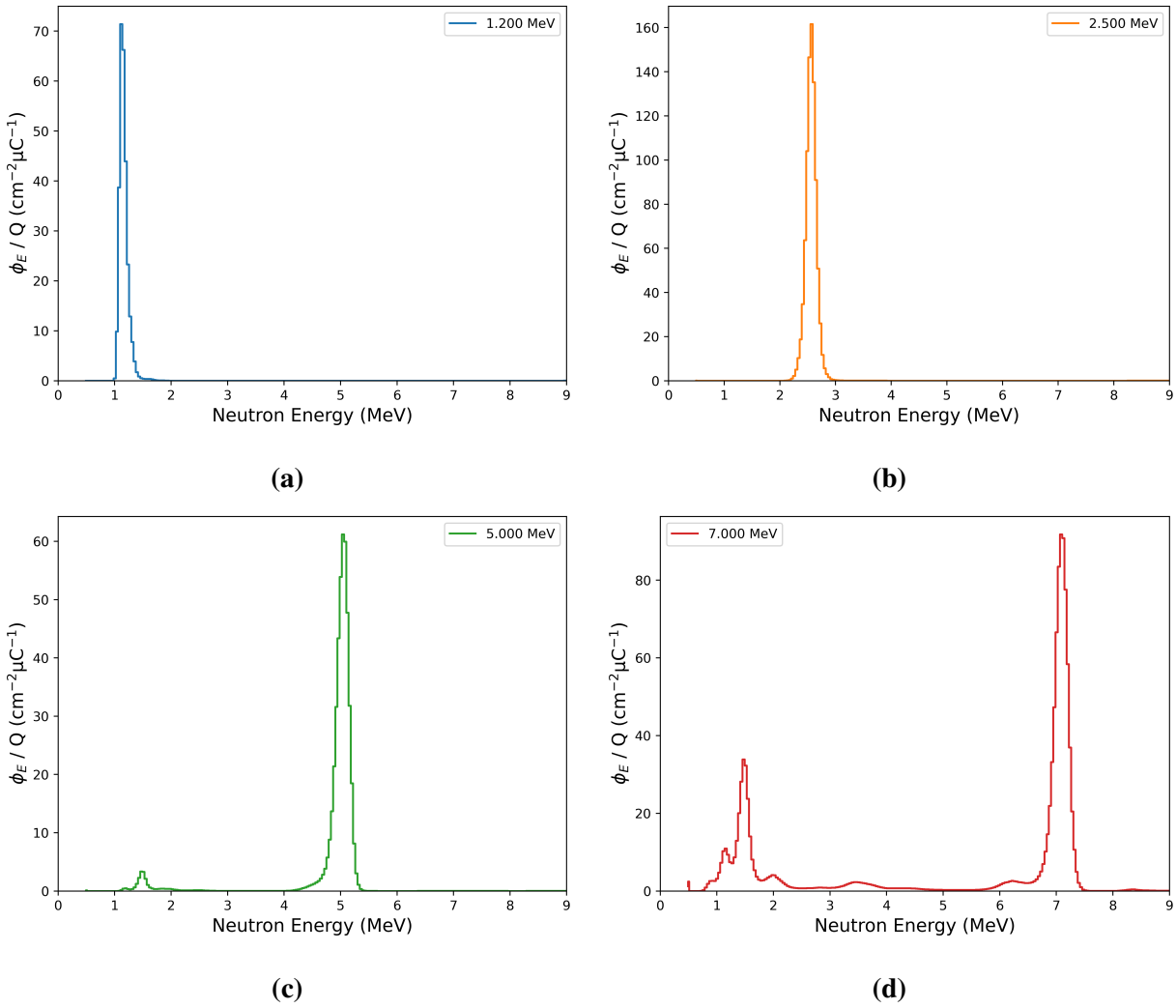

Figure 5.20: Scaled using the monitor value associated with the cumulative charge, the MAXED unfolded neutron energy spectra measured with the digital acquisition system are plotted for four neutron fields with nominal energies of (a) 1.200 MeV; (b) 2.50 MeV; (c) 5.000 MeV and (d) 7.000 MeV for the standard intensities. Effects of pile up are visible in (d) by the small feature at 8.5 MeV. These spectra are not corrected for dead time or pile up effects. The lower energy peaks are attributed to secondary reaction channels with carbon and oxygen in the TiT target [108]

5.3.4 Peak Neutron Energy Uncertainty Analysis

Using the same method of analysis as for the analogue energy calculations, a Gaussian function was fitted to the primary peaks and the centroid of the distribution is taken as the best estimate, $E^{obs}_{n,peak}$, for the energy measured. The uncertainty in the fit parameters is small in comparison to the uncertainty introduced in the MeV_{ee} calibration. The results of the fitting along with the TARGET calculated expected values are given in table 5.2.

Table 5.2: Calculated and measured (obs) values for the peak neutron energy for the standard intensity neutron energy measurements made with the DT5730 CAEN digital acquisition system.

$E^{calc}_{n,peak}$ (MeV)	$E^{obs}_{n,peak}$ (MeV)
1.200 ± 0.003	1.160 ± 0.030
2.500 ± 0.004	2.632 ± 0.059
5.000 ± 0.003	5.150 ± 0.085
7.000 ± 0.006	7.24 ± 0.12

Since the digital long gate was chosen to match the analogue measurements there is a similar disagreement between the Gaussian fitted primary peaks and the expected values as was seen in the analogue measurements. To account for this the same correction factor must be applied, k_{RM}. An additional scaling factor can be introduced to account for differences introduced by the choice of long gate, k_D.

However, since there is no way to deconvolve the two scaling factors from each other and no way to determine their combined value, a correction factor can be applied to scale the results linearly to account for the difference between the measured values and the simulated calculated values, k_{RMD}. Unfortunately, due to the anode only information and the outdated response functions, it is not possible to show that k_{RMD} is equal to the combination of k_D and k_{RM}.

In the same way that k_{RM} was determined for the analogue measurements, figure 5.21 shows the plot of $E^{obs}_{n,peak}$ versus $E^{meas}_{n,peak}$ allowing us to apply a linear fit. The linear fit has a gradient of $1.019(79)$ and an intercept of $0.010(42)$ MeV. Included in the plot is the line of $E^{obs}_{n,peak} = E^{meas}_{n,peak}$ to indicate the line of best agreement between the values.

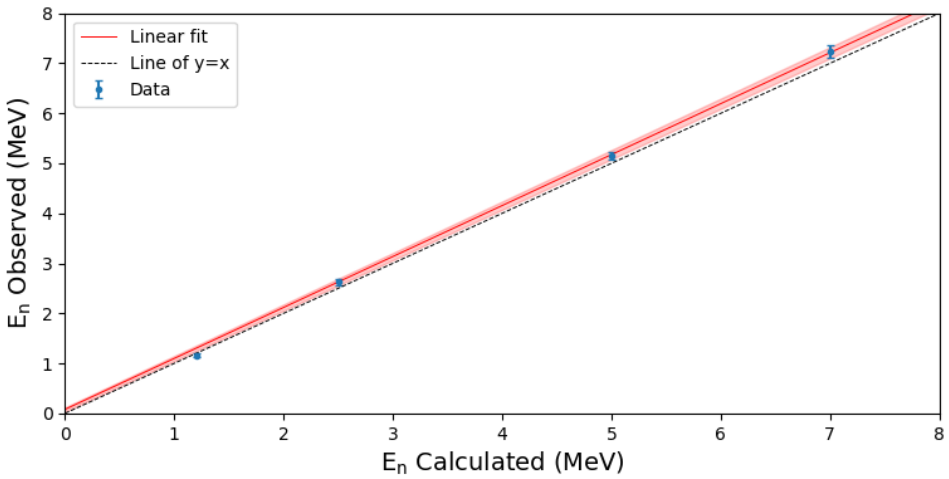

Figure 5.21: The observed neutron peak energies (MeV) vs the calculated neutron peak energies (MeV). The red line has a slope value of 1.019(79) and an intercept value 0.010(42) MeV.

The scaling factor applied, k_{RMD}, is then defined as the inverse of the gradient of a fitted linear fit between the expected values (figure 5.21) for the primary peaks and the measured values, according to equation 5.7.

$$k_{RMD} := \frac{1}{m} = \mathbf{0.9812(97)} \tag{5.7}$$

The final neutron energy measurement, $E^{meas}_{n,peak}$, quoted is then defined by equation 5.8.

$$E^{meas}_{n,peak} = k_{RMD} E^{obs}_{n,peak} \tag{5.8}$$

The uncertainties in $E^{meas}_{n,peak}$ is then the combined uncertainties of the $\mathrm{MeV_{ee}}$ calibration and the scaling factor k_{RMD}. The scaling factor uncertainty is defined by propagating the fit uncertainty in the fitted gradient through to the inverse. Equation 5.9 defines the final combined uncertainty.

$$u\left(E^{meas}_{n,peak}\right) = E^{meas}_{n,peak} \sqrt{\left[\frac{u\left(E^{obs}_{n,peak}\right)}{E^{obs}_{n,peak}}\right]^2 + \left[\frac{u(k_{RMD})}{k_{RMD}}\right]^2} \tag{5.9}$$

The best estimates for the unscaled measured primary peaks have been tabulated in table 5.3 along with both the expected calculated values from the beam conditions using the TARGET code [92] and the final scaled measured values. The final values $E^{meas}_{n,peak}$ all agree with the expected values $E^{calc}_{n,peak}$ within 2σ. For the 1.200 MeV standard intensity measurement the voltage threshold limited the line shape of the spectra significantly, affecting the unfolded neutron energy spectrum.

Table 5.3: Calculated and measured final values for the standard intensity neutron energy measurements made with the DT5730 CAEN digital acquisition system.

$E^{calc}_{n,peak}$	(MeV)	1.200(3)	2.500(4)	5.000(3)	7.000(6)
$E^{obs}n, peak$	(MeV)	1.160(30)	2.632(59)	5.150(85)	7.24(12)
$E^{meas}_{n,peak}$	(MeV)	**1.160(30)**	**2.582(63)**	**5.053(97)**	**7.10(14)**

5.3.5 Peak Fluence Intensity Uncertainty Analysis

For fluence measurements, the counts in the primary peak in the raw unfolded neutron spectra are summed $\left(\Phi^{obs}_{E,peak}\right)$, and then scaled appropriately to produce $\Phi^{meas}_{E,peak}$ in the desired units. Equation 5.10 shows the method by which $\Phi^{obs}_{E,peak}$ was calculated.

$$\Phi^{obs}_{E,peak} = \sum_{j=i-6\sigma}^{i+3\sigma} \phi_j, \tag{5.10}$$

where ϕ_j is the jth channel of the raw unfolded neutron energy spectrum ϕ, i is the centroid channel of the primary peak and σ is the standard deviation of the peak in channels. The summation over the peak is asymmetrical due to the asymmetry in the peak due to energy loss in the target.

The uncertainty in $\Phi^{obs}_{E,peak}$ is then the combined uncertainty in each of the channels. The uncertainties are combined by the square root of the sum of the squared values for each channel as shown in equation 5.11.

$$u\left(\Phi^{obs}_{E,peak}\right) = \sqrt{\sum_{j=i-6\sigma}^{i+3\sigma} u(\phi_j)^2} \tag{5.11}$$

The uncertainties in each channel are determined by the ICQU UMG package (appendix A). The package propagates the uncertainties in the measured neutron light output spectra through the unfolding fitting process. The uncertainties in the neutron light output spectra include the uncertainty due to counting and binning and uncertainty introduced by the PSD cuts. For more detail on these uncertainties refer to section 4.4.

In order to express our final fluence ($\Phi^{meas}_{E,peak}$) in units of neutrons cm^{-2} μC^{-1}, the raw quantity calculated in equation 5.10 is scaled by the charge integrator count (Q) and then corrected for dead time and pulse pile up effects, as shown in equation 5.12.

$$\Phi^{meas}_{E,peak} = k_{DT} \frac{\Phi^{obs}_{E,peak}}{Q}, \tag{5.12}$$

where k_{DT} is defined in equation 5.13 to include contributions from buffer saturation (k_S) and pulse pile up (k_{PU}).

$$k_{DT} = k_S \, k_{PU} \tag{5.13}$$

For the standard intensity measurements, other than the 1.200 MeV measurement, the digitiser was operating below buffer saturation so k_S takes on the value of unity within one standard uncertainty. This correction factor and how to calculate them are discussed in detail in section 5.4.

The standard uncertainty in the final fluence value, $\Phi^{meas}_{E,peak}$, is then:

$$u\left(\Phi^{meas}_{E,peak}\right) = \Phi^{meas}_{E,peak}\sqrt{\left[\frac{u(\Phi^{obs}_{E,peak})}{\Phi^{obs}_{E,peak}}\right]^2 + \left[\frac{u(Q)}{Q}\right]^2 + \left[\frac{u(k_{DT})}{k_{DT}}\right]^2}, \tag{5.14}$$

where

$u(\Phi^{obs}_{E,peak})$: given by equation 5.11

$u(Q)$: Poisson counting, takes the value of $\sqrt{Q}$

$u(k_{DT})$: takes the value of $k_{DT}\sqrt{\left[\frac{u(k_S)}{k_S}\right]^2 + \left[\frac{u(k_{PU})}{k_{PU}}\right]^2}$

The scaling factors used and their uncertainties are presented in table 5.4.

Table 5.4: The calculated scaling factors with their associated uncertainties for the peak neutron fluence calculations for the standard intensity digital measurements.

$E^{calc}_{n,peak}$ (MeV)	1.200(3)	2.500(4)	5.000(3)	7.000(6)
Q (μC)	2551.374(51)	336.603(18)	301.833(17)	331.364(18)
k_S	1.3642(41)	1.0010(21)	1.0010(27)	1.0010(25)
k_{PU}	1.0030(79)	1.001(21)	1.001(37)	1.002(17)

The resultant fluence measurements for the digitally measured standard intensities are presented in table 5.5 along with their associated uncertainties and the expected literature values.

Table 5.5: The calculated neutron fluence measurements for the peak neutron fluence calculations for the standard intensity measurements with and without the correction factors,along with their associated uncertainties. *Uncertainties provided by ICQU on the order of $\times 10^{-6}$

$E^{calc}_{n,peak}$ (MeV)	1.200(3)	2.500(4)	5.000(3)	7.000(6)
$\Phi^{obs}_{E,peak}$ ($\times 10^4 \mathrm{cm}^{-2}$)	71.02*	29.23*	12.85*	23.35*
$\Phi^{meas}_{E,peak}$ ($\mathrm{cm}^{-2}\ \mu\mathrm{C}^{-1}$)	380.9(32)	869(19)	426(16)	706(12)

5.4 Measurements at Higher Intensities

Several measurements were made with the BC501A detector and the CAEN digitiser (section 3.1.4) of varying beam current for nominal neutron energies of 2.500 MeV, 5.000 MeV and 7.000 MeV. Counts as a function of pulse shape and light output parameters have been plotted for beam currents of 0.140 µA, 0.593 µA, 1.180 µA and 2.500 µA for the primary neutron energy of 7.000 MeV in figure 5.22. The shape of the proton and electron loci are consistent throughout but the proportion of the pile up events that occur increase as a function of intensity as expected. The source and effect of pile up events has been discussed in section 5.3.1.

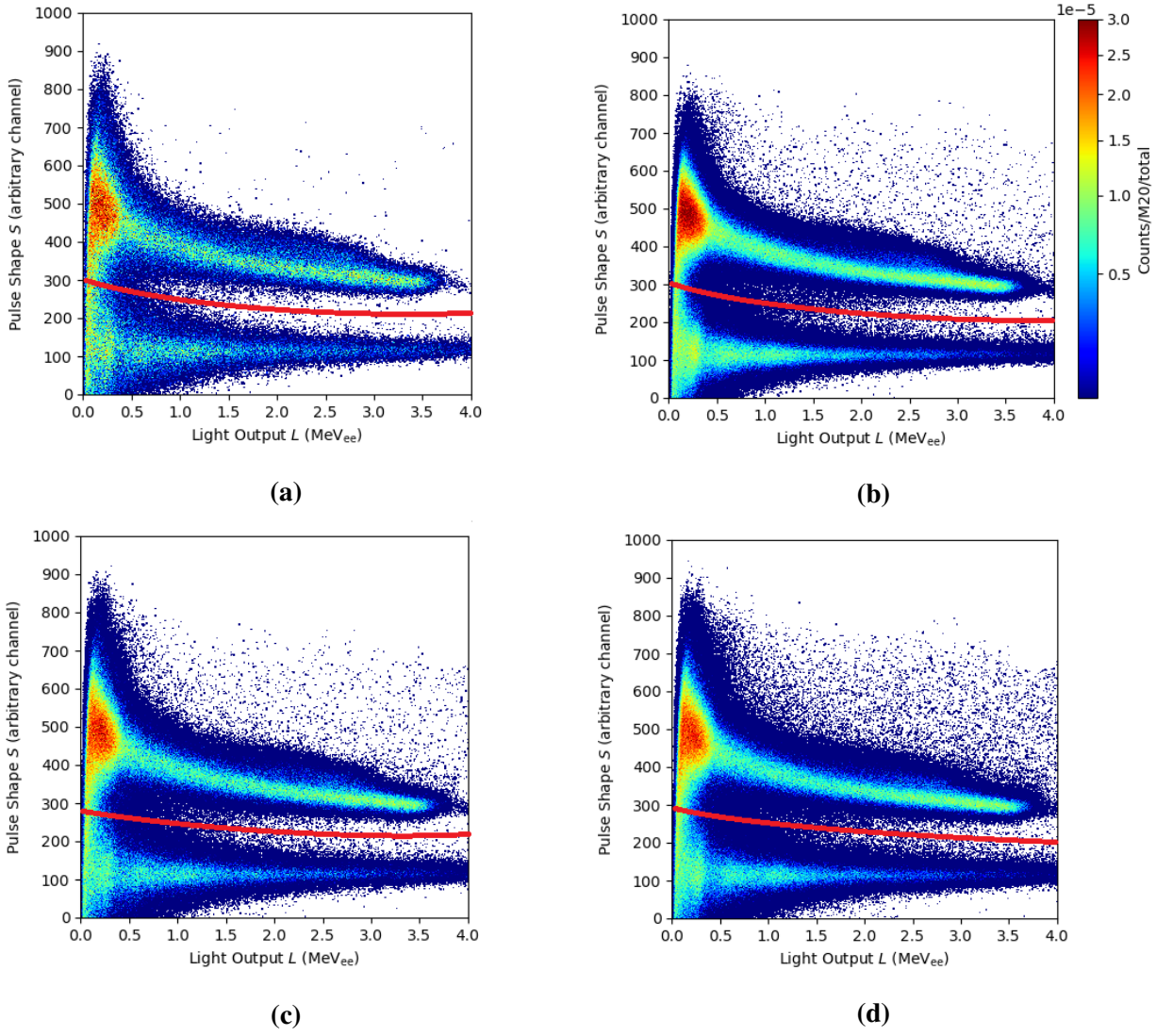

Figure 5.22: Counts as a function of S and L measured with the digital acquisition system for four neutron fields with a nominal energy of 7.000 MeV for beam currents of (a) 0.140 µA; (b) 0.593 µA; (c) 1.180 µA and (d) 2.500 µA. The the cut applied used to separate the gamma-ray and neutron induced events is indicated by the red line.

The events associated with the LED pulser in the detector have been removed from the measurements between L values of 3.5 MeV_{ee} to 4.0 MeV_{ee} with an S value between 700 and 800.

The neutron light output spectra for these measurements (fig. 5.22) along with the additional intensity measurements for the 2.500 MeV and 5.000 MeV neutron beams, scaled by the monitor value Q and then corrected for dead time and pile up as per described in the sections 5.3.1 and 5.3.2, have been plotted in figure 5.23. The correction factors and scaling factors used for the presented results can be found in appendix D. Figure 5.23 shows the scaled neutron light output spectra for the three different nominal energies measured with the digital data acquisition system.

The neutron line shapes should agree with each other after these scaling factors but there are still large discrepancies, as seen in figure 5.23, which propagate to the numerical fluence measurements. As there was with the MPA measurements of the 2.500 MeV neutron field, with the digitally acquired 0.54 μA measurement has a higher resultant scaled counts than the 0.11 μA measurement for the 2.500 MeV neutron field. Both the 5.000 MeV and 7.000 MeV measurements agree with each other, except for the highest intensity measurement.

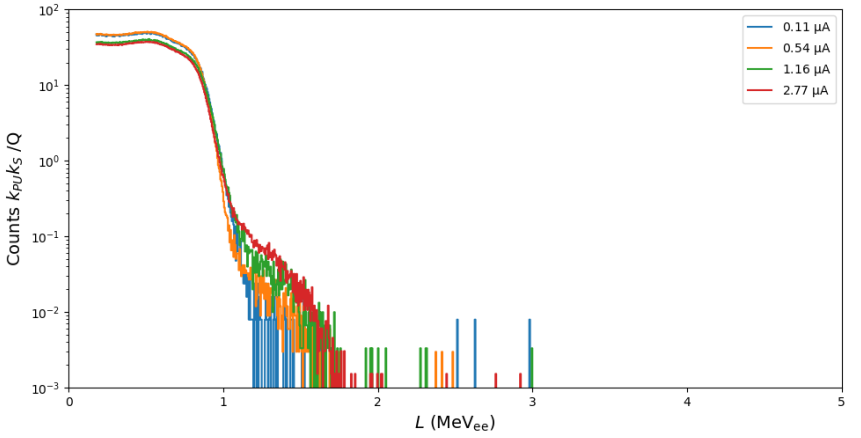

(a)

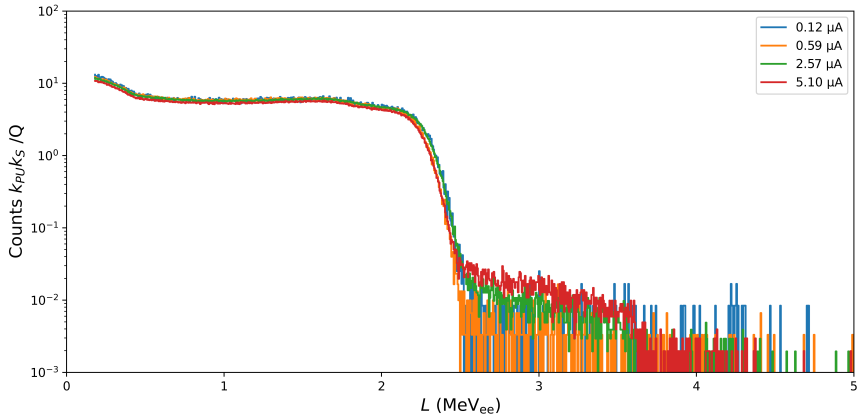

(b)

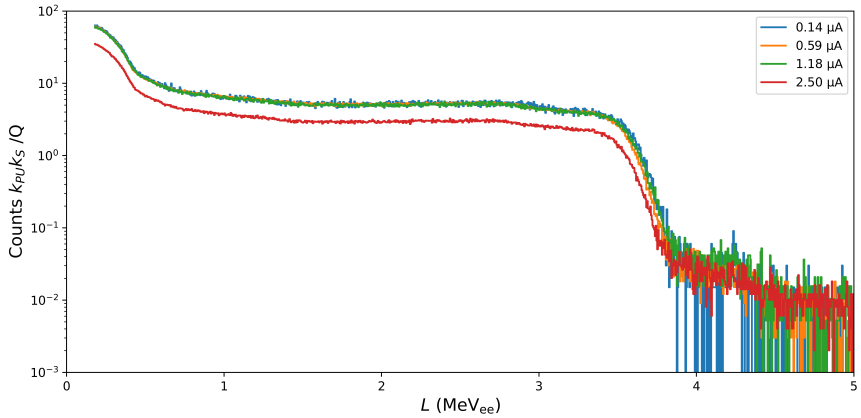

(c)

Figure 5.23: Neutron light output spectra for three different nominal neutron energies (a) 2.500 MeV, (b) 5.000 MeV and (c) 7.000 MeV. At each energy four different beam intensities were measured. The spectra have all been scaled by the charge integrator monitor value and corrected for pile up events and buffer saturation.

5.4.1 Results

The resultant scaled unfolded spectra have been plotted in figure 5.24. As a result of the difference in the neutron light output spectra shown in figure 5.23, the unfolded neutron energy spectra for the different beam intensities do not align in amplitude, except for the 5.000 MeV measurement. All unfolded spectra align in energy and exhibit similar energy resolution. The small peak due to pile up only being evident at the higher intensities at each energy.

The primary peak neutron energy measurements quoted in table 5.6 have all been scaled appropriately using the same factors determined in section 5.3.4, equation 5.7. The raw peak neutron fluences, $\Phi^{obs}_{E,peak}$, for each of the beam conditions, along with the associated scaling factors k_{PU}, k_s and Q, can be found in table D.1 in appendix D. The fluence values presented in table 5.6 were calculated from the energy spectra produced by the ICQU UMG package and are scaled using the charge integrator monitor value, Q, and corrected for pile up and buffer saturation effects.

Table 5.6: The calculated neutron fluence measurements for the peak neutron fluence calculations for the standard intensity measurements with and without the correction factors, along with their associated uncertainties.

$E^{calc}_{n,peak}$ [MeV]	Beam Current [μA]	$E^{meas}_{n,peak}$ [MeV]	$\Phi^{meas}_{E,peak}$ [cm^{-2} μC^{-1}]
2.50(04)	0.108	2.589(65)	844(34)
	0.540	2.582(63)	869(19)
	1.160	2.602(64)	687(15)
	2.770	2.580(63)	633.4(77)
5.00(03)	0.122	5.090(97)	432(19)
	0.585	5.053(97)	426(16)
	2.570	5.096(98)	427.5(58)
	5.100	5.054(97)	390.2(45)
7.00(06)	0.140	7.16(14)	726(26)
	0.593	7.10(13)	706(12)
	1.180	7.14(13)	697(14)
	2.500	7.09(14)	402.1(50)

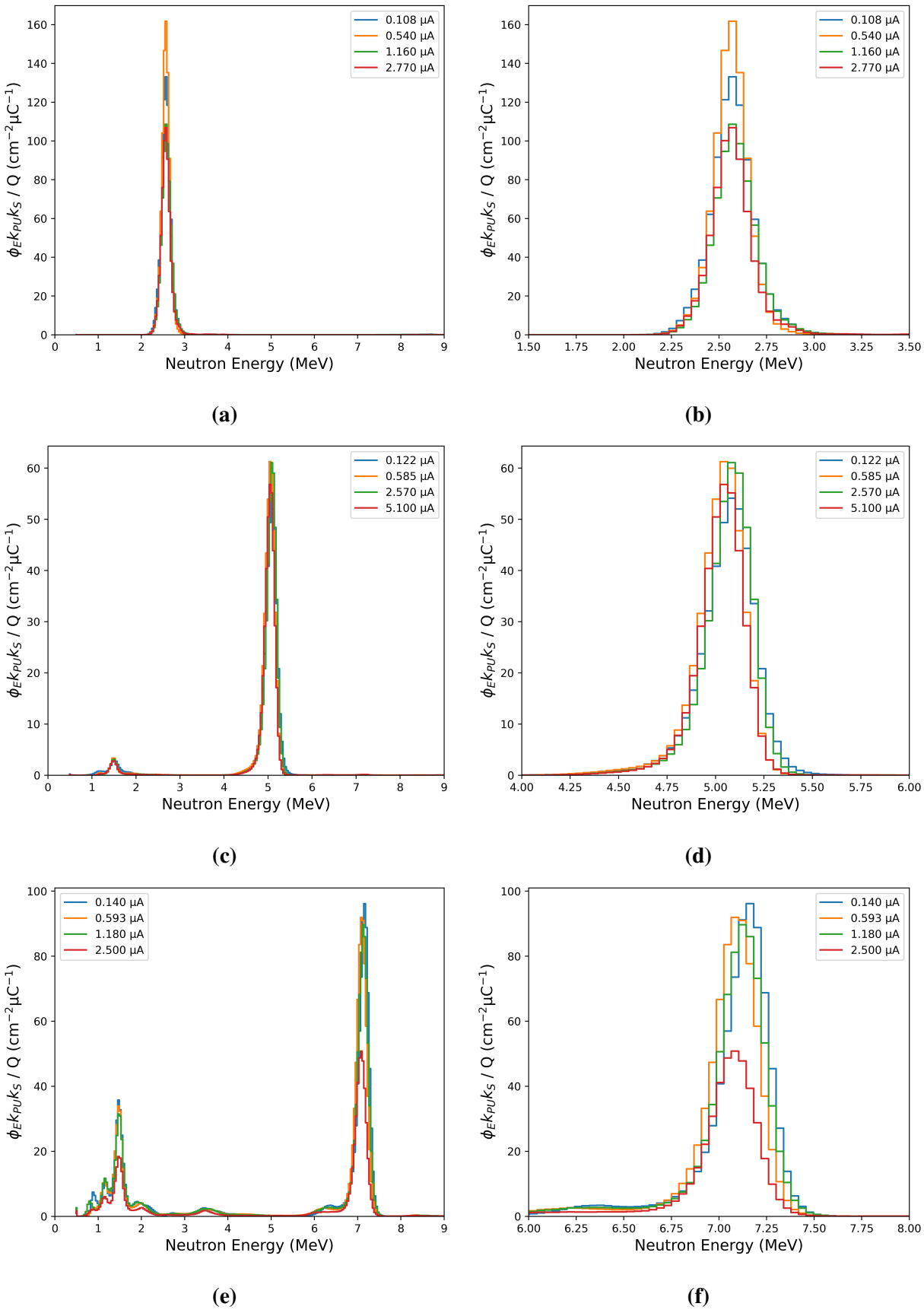

Figure 5.24: Unfolded fluence spectra, in cm^{-2}µC^{-1}, for the different intensity beams at the nominal energies of (a) 2.500 MeV, (c) 5.000 MeV and (e) 7.000 MeV, plots (b), (d) and (f) show only the nominal peaks of the same spectra respectively. All spectra are corrected for pile up and buffer saturation.

6. Dual Channel Digital Data Acquisition

Additional measurements were made at the n-lab facility [111] at the University of Cape Town (UCT). These measurements were made to further address the issue of choice of long gate for digital neutron measurements without time-of-flight information which was demonstrated in section 5.1.3. Thus the digital pulse height parameter and its relationship to L is explored in further detail within this section.

6.1 n-lab Facility

The fast neutron facility (n-lab) falls within the Metrological and Applied Sciences University Research Unit (MeASURe) in Department of Physics at UCT. The n-lab features a Thermo MP-320 [112] sealed tube neutron generator (STNG) which produces mono-energetic neutrons of approximately 14 MeV through a deuterium-tritium fusion reaction. Neutrons can be produced in pulsed or steady state mode with variable beam current up to a maximum of 60 μA. Operating optimally the STNG can produce rates of up to 10^8 neutrons per second into 4π steradians.

Additional to the STNG, the n-lab provides a broad neutron energy spectrum ranging from the thermal range to 11 MeV through the use of a 220 GBq ^{241}Am-^{9}Be radioisotopic source. The AmBe source produces approximately 10^7 neutrons per second into 4π steradians. These two main sources that n-lab hosts make the facility able to cater to a wide range of measurements.

The two sources are housed in a well shielded vault consisting of high-density polyethelene (HDPE) with a variable size collimator producing a pencil beam of neutrons in the experimental area, refer to figure 6.1 for a layout of the facility. The variable collimator is operated at a standard exit diameter of 0.8 cm. The neutron fluence n-lab provides is approximately 400 neutrons cm^{-2} s^{-1} (STNG) and 40 neutrons cm^{-2} s^{-1} (AmBe) at 1.40 m from the source.

The facility includes two reference detectors used as monitors: one liquid scintillator detector embedded in the vault near to the source, and a thin plastic scintillator near the exit of the collimator. These two detectors are used to monitor the neutron emission rate, and to scale all measurements to the same fluence for comparative measurements.

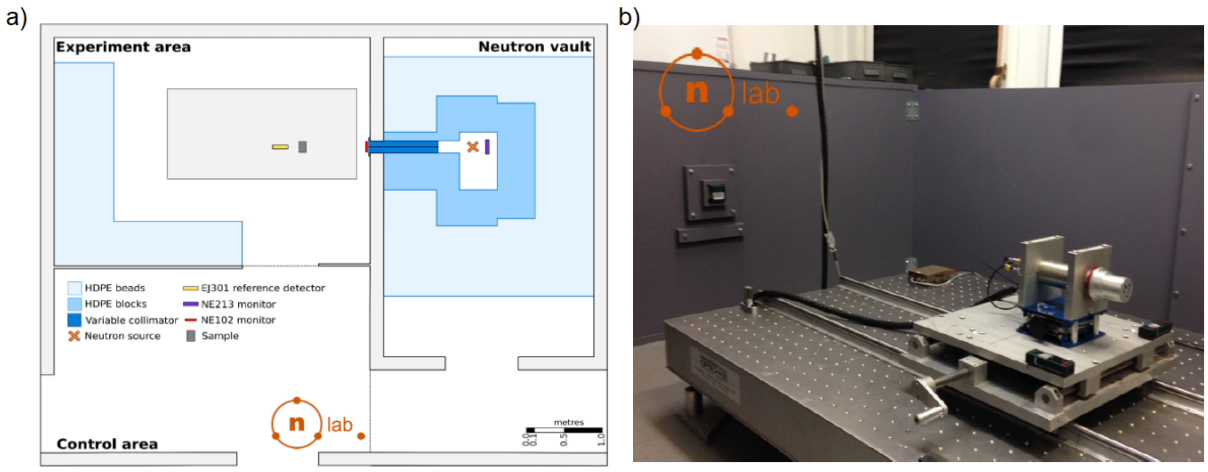

Figure 6.1: (a) A schematic of the layout of the n-lab facility at UCT, showing the vault enclosing the sources along with the experimental measurement area and control section. (b) A photograph of the standard EJ301 detector on the positioning system within the experimental area.

The standard detector used for neutron measurements at the facility is a 50 mm x 50 mm cylindrical EJ301 liquid scintillator [113] optically coupled to a Scionix supplied ETL 9214 12-stage photomultiplier tube [114] and base, operated at a HV negative bias of 1100 V. This detector is equivalent in scintillator chemistry to the BC501A liquid scintillator detector used for the measurements taken at AMANDE, this setup is then ideal for follow up measurements.

6.2 The Digital Pulse Height Parameter

Considering a standard organic liquid scintillator detector such as the BC501A or EJ301 detector, the ionisation and energy deposition is considered instantaneous in conjunction with the resultant scintillation light producing free charge within the photomultiplier tube (PMT). The intensity of the scintillation light is proportional to both the energy deposited in the scintillation medium and the amount of free charge produced in the PMT.

The charges produced are then multiplied through a set of dynodes which create an electron cascade. Once all the charge reaches the anode the charge induction ceases [115], t_c. This processes, typically referred to as charge collection, creates an electronic signal. The time integral of this signal, $i(t)$ for $t = [0, t_c]$, is then equal to the total charge produced from the energy deposited in the scintillation medium.

An equivalent circuit of the base anode electronics consists of a parallel RC circuit, shown in figure 6.2. The scintillation light is assumed to decay exponentially with decay constant λ, thus $i(t)$ can be described by:

$$i(t) = i_0 e^{-\lambda t}, \tag{6.1}$$

where the i_0 refers to the initial current and be determined through the total time integral of $i(t)$ being equal to the total charge induced, Q. The resultant expression for $i(t)$ is then given by

$$i(t) = Q\lambda e^{-\lambda t}. \tag{6.2}$$

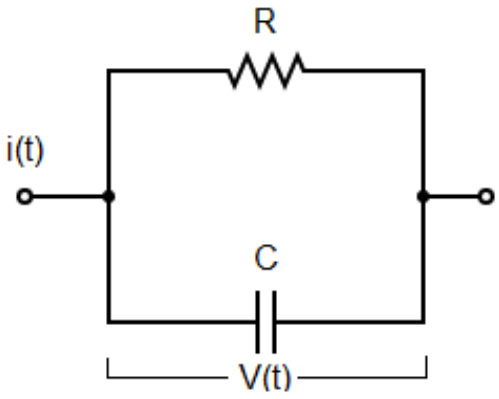

Figure 6.2: Circuit schematic of the anode electronics with resistor R, capacitor C and current $i(t)$. The voltage across the capacitor or resistor is given by $V(t)$.

Additionally, the current $i(t)$ must be equal to the sum of the current in the resistor and capacitor branches:

$$i(t) = C\frac{dV(t)}{dt} + \frac{V(t)}{R}. \tag{6.3}$$

Combining equation 6.2 and 6.3 a differential equation for the voltage $V(t)$ is given by

$$\frac{dV(t)}{dt} + \frac{V(t)}{RC} = \frac{\lambda Q}{C} e^{\lambda t}. \tag{6.4}$$

With an inital condition of $V(0) = 0$, the voltage is

$$V(t) = \frac{1}{\lambda - \Theta}\frac{\lambda Q}{C}\left[e^{\Theta t} - e^{-\lambda t}\right], \tag{6.5}$$

where $\Theta = 1/RC$. In the case of $\Theta \ll \lambda$ (large time constant relative to Θ, dynode electronics) the amplitude of the pulse tends to Q/C, while for $\Theta \gg \lambda$ (short constant relative to Θ, anode electronics) the amplitude of the pulse tends to $\lambda Q/\Theta C$.

The pulse height parameter is to be defined such that it is proportional to the energy deposited in the detector. This parameter must be determined from the output of the detector $i(t)$ and can be determined in a number of ways [110]:

- integrate on the sensor capacitance
- charge sensitive pre-amplifier (CSP) along the dynode and determine the pulse height
- amplify $i(t)$ and use a charge collecting ADC
- sample the anode voltage at a high frequency and digitally integrate

In traditional analogue electronics systems typically use a CSP in conjunction with an amplifier along the dynode output [13] to produce the light output parameter $\boldsymbol{L}$ from the amplitude of the event. The CSP integrates the current pulse with the use of a long time constant capacitor, converting the collected charge into a voltage amplitude, refer to equation 6.6 where V_{dyn} is the potential difference measured across the capacitor, Q is the total collected charge and C is the capacitance of the capacitor.

$$V_{dynode} = \frac{Q}{C} \tag{6.6}$$

After this integration the information of the energy deposited in the detector is carried in the amplitude of the pulse. The critical parameter in these systems is the total capacitance in the system. The greater the capacitance the smaller the signal-to-noise ratio (SNR) [110]. This is usually applied to the dynode output of the detector due to the long time constant of the dynode electronics chain resulting in a better energy resolution while the fast timing aspect of the anode is better for measurements requiring good time resolution, such as the pulse shape parameter determined through a zero-crossing method. The larger time constant on the dynode chain allows for one to measure the voltage being proportional to the collected charge even without a pre-amplifier or amplifier, but due to the load of the analogue electronics the pre-amplifier is necessary.

The measurements were made with a pre-amplifier and amplifier on the dynode acquired at the same time as the anode. Although the digitiser is significant loading on the anode, the anode was acquired without a pre-amplifier in order to relate to the measurements made at the IRSN.

The CAEN digitiser connections make use of a 50 Ω terminator to impedance match with the NIM/TTL signals on LEMO connectors to ensure that the input of the digitiser is on the same order of magnitude as the output of the equivalent analogue readout output. The 50 Ω terminator is a considerable load on the dynode and anode. Due to the low impedance of the anode (as a requirement for timing resolution for PSD) a pre-amplifier should be used between the output of the anode or dynode to the digitiser in order to maintain the integrity of the pulse.

The digital equivalent of the analogue CSP along the dynode chain, is to digitally integrate or sum the raw anode pulses over time. A single current pulse is measured across a resistor resulting in a voltage pulse described by equation 6.7, where $V_{anode}(t)$ is the raw anode voltage as a function of time, $i(t)$ is the time dependent current pulse and R is the resistance of the resistor which the current pulse is measured across. The voltage pulse must therefore be integrated to obtain the charge Q, which should be proportional to the energy deposited in the detector [13], as demonstrated in equation 6.8, where t_0 is the beginning of the event and t_L is the charge collection time, or some reasonable time to encompass the pulse. As expected for a small t_L, with regards to the duration of the pulse, the full charge would not be determined while for t_L tending to infinity, additional contributions due to noise and baseline variation would become larger.

$$V_{anode}(t) = i(t)R \tag{6.7}$$

$$\int_{t_0}^{t_L} V_{anode}(t)dt = R\int_{t_0}^{t_L} i(t)dt \equiv RQ \tag{6.8}$$

An important choice in determining L digitally is then the integration time t_L (long gate). For a single event without noise or baseline variation, the ideal long gate would be $t_L = \text{inf}$, but due to practicalities we require $t_l < \text{inf}$. The longer the window of integration the greater percentage of pile up events, even in such low event rates such that pile up events would be unlikely an extremely long integral window starts to decrease the SNR due to the portion of the window where the noise is dominant.

Due to the different pulse shapes caused by the different interacting radiation there is an additional factor to consider in the choice of t_L. Referring to figure 6.3, the two neutron pulses that have been plotted have the same apparent energy in MeV_{ee} as a gamma-ray for two integral times of 300 ns and 800 ns respectively. This shows that the relationship between the gamma-ray and neutron scales change as a function of long gate and directly affects the results one would get from unfolding neutron energy from a MeV_{ee} calibrated neutron light output spectrum. The issue of a long gate choice is therefore not present when only dealing with gamma-ray measurements, or time-of-flight neutron spectrometry.

The unfolding process is heavily reliant on a well characterised detector relative to the response functions. Response functions have, in the past, been calibrated to the detector through empirical measurements made with the standard analogue acquisition system used with that detector, in this case the dynode pulse height. These measurements determine the relationship between a light output spectrum calibrated to electron equivalent MeV (MeV_{ee}) and the associated neutron line shape which determines the neutron energy in MeV. For the case of integrating the anode pulse this relationship is different as a function of neutron energy and integration time of the pulses, as shown in figure 6.3.

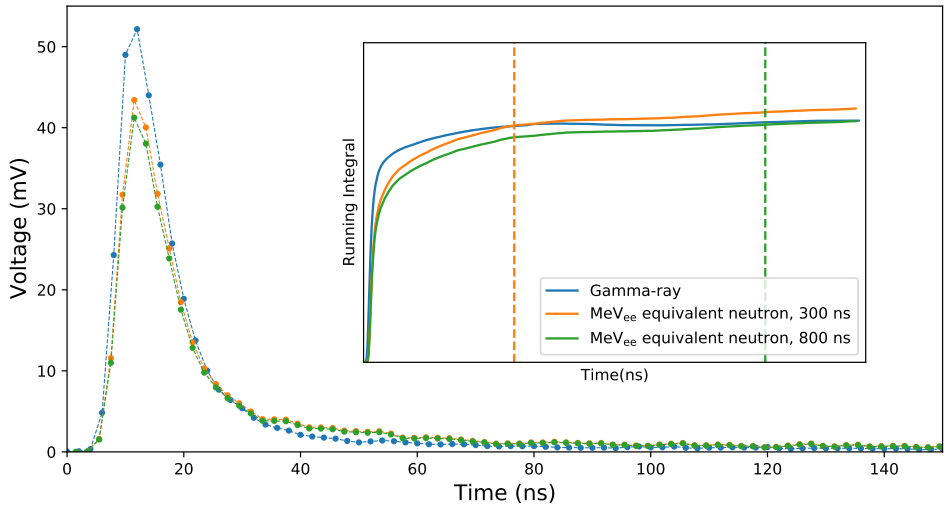

Figure 6.3: Plot showing the pulse shape of a gamma-ray and two neutron pulses. The neutron pulses are the MeV_{ee} equivalent to the gamma-ray pulse for two different long gate choices, 300 ns and 800 ns.

6.3 The Measurements

The measurements presented in this section were made with the 0.8 cm diameter collimated 14.1 MeV neutron beam produced by the STNG by accelerating deuterium incident on a zirconium doped tritium target with a beam current of 60 µA and accelerator voltage of 80 kV. The reference detector was placed directly in the neutron beam line at 1.68 m from the centre of the STNG target.

A CAEN DT5730 desktop digitiser was used to acquire the anode signal along with the dynode signal after a 100 pF CSP and an amplifier. The amplifier was set to 50 V coarse gain and a 0.5 µs shaping time. The high voltage was set to -1.07 kV. The raw anode pulses were acquired in channel 0 and the dynode through the pre-amplifier and amplifier were acquired on channel 1. For each triggered event, both the anode and dynode outputs were acquired.

With the raw pulses from the two channels two sets of pulse height parameters can be extracted, the digitally integrated raw anode pulse following equation 6.8 (anode integral) and the equivalent of the analogue pulse height parameter from the dynode chain and extracting the acquired pulse amplitudes (dynode PH). These can then be used to investigate the behaviour of the digitally integrated anode pulse in comparison with the analogue equivalent pulse height, dynode PH. The dynode PH is independent of post acquisition choices.

The pulse shape parameter is calculated in the standard digital charge comparison method as in chapter 3, equation 2.7, using the ratio of a shorter integral to a longer integral bound of the same anode pulse. The short integral length was set to being 30 ns from the start (defined by the CFD as per the previous chapters, for more information on the digital CFD refer to chapter 5).

Figure 6.4 presents counts as a function of pulse shape parameter (S) and the dynode chain pulse height parameter L, for the AmBe radioisotopic source measurement and the 14.1 MeV neutron beam along with their associated cuts to separate the neutron induced events from the gamma-ray induced events.

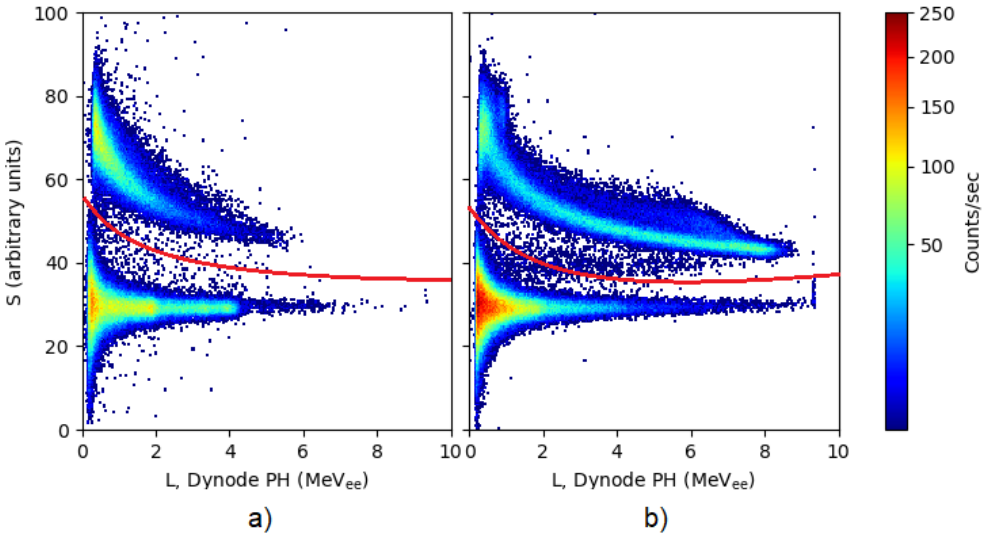

Figure 6.4: Count rate as a function of pulse height parameter, dynode PH, and the pulse shape parameter for (a) the AmBe radio-isotopic source and (b) the 14.1 MeV neutron beam. Small amounts of pulse height saturation occurring at around 9.5 MeV_{ee} in both measurements. The red line indicates the cuts chosen to separate the neutron induced events from the gamma-ray induced events.

For the MeV_{ee} calibration the gamma-ray sources used were ^{22}Na, ^{60}Co, ^{54}Mn, ^{137}Cs and the radio-isotopic AmBe source. For each long gate chosen there is a different MeV_{ee} calibration, presented in figure 6.5. The three different long integral lengths used for the results presented are 50 ns, 450 ns and 1700 ns.

These integral lengths have been chosen to investigate the consequences of having an integral which: does not include all the charge information (50 ns), a reasonable choice (450 ns) and an integral time with a significant portion of the window which is baseline (1700 ns).

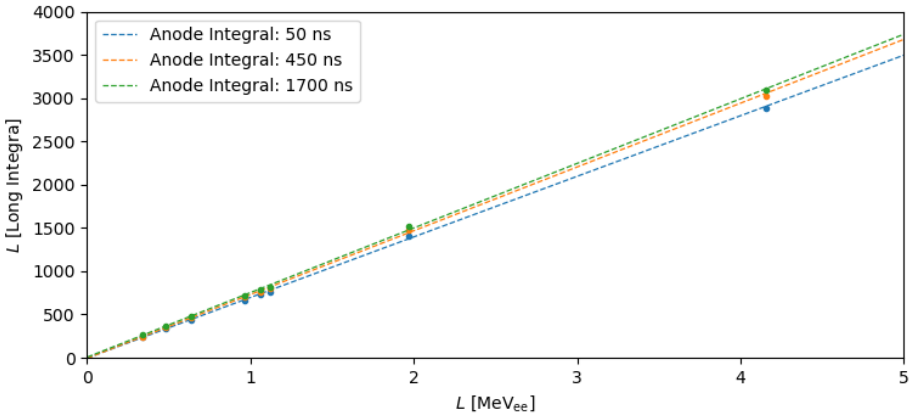

Figure 6.5: Gamma-ray calibrations for the anode integral lengths of 50 ns, 450 ns and 1700 ns using a weighted linear least square fit. The fitted calibrations have gradients of 0.001428(11) longint/MeV_{ee}, 0.001356(11) longint/MeV_{ee} and 0.001340(14) longint/MeV_{ee} respectively.

6.4 Long Gate Choice

The two different pulse height parameters calculated either along the anode or the dynode chain should be proportional to each other by definition. If these two pulse height parameters are equivalent, or at least proportional to each other, they should be linear with respect to each other with gamma-ray and neutron induced events being equivalent in both parameters. Considering the ratio of two parameters plotted in figure 6.6, the difference between the parameters is evident through the separation of events. The distribution of this ratio would also provide the scaling factors required for both the neutron and the gamma-ray induced events to ensure the relationship between the two would be equal to the empirical relationship between neutron and gamma-ray MeV_{ee} scales in the analogue measurements.

The distribution plotted in figure 6.6 shows events as a function of the ratio of the two pulse height parameters and the anode integral for the AmBe data set. The separation of the neutron and gamma-ray associated events seen forms due to the choice of the anode integral forming a charge integral comparison using the anode integral (short integral) and the dynode PH (total energy deposited in the detector as defined by the dynode PH). If the choice of anode integral length produced a quantity which is proportional to the total energy deposited in the detector this should give a single peaked distribution. Any other choices of anode long integral length would result in the split of the two distributions in the ratio as seen in figure 6.6.

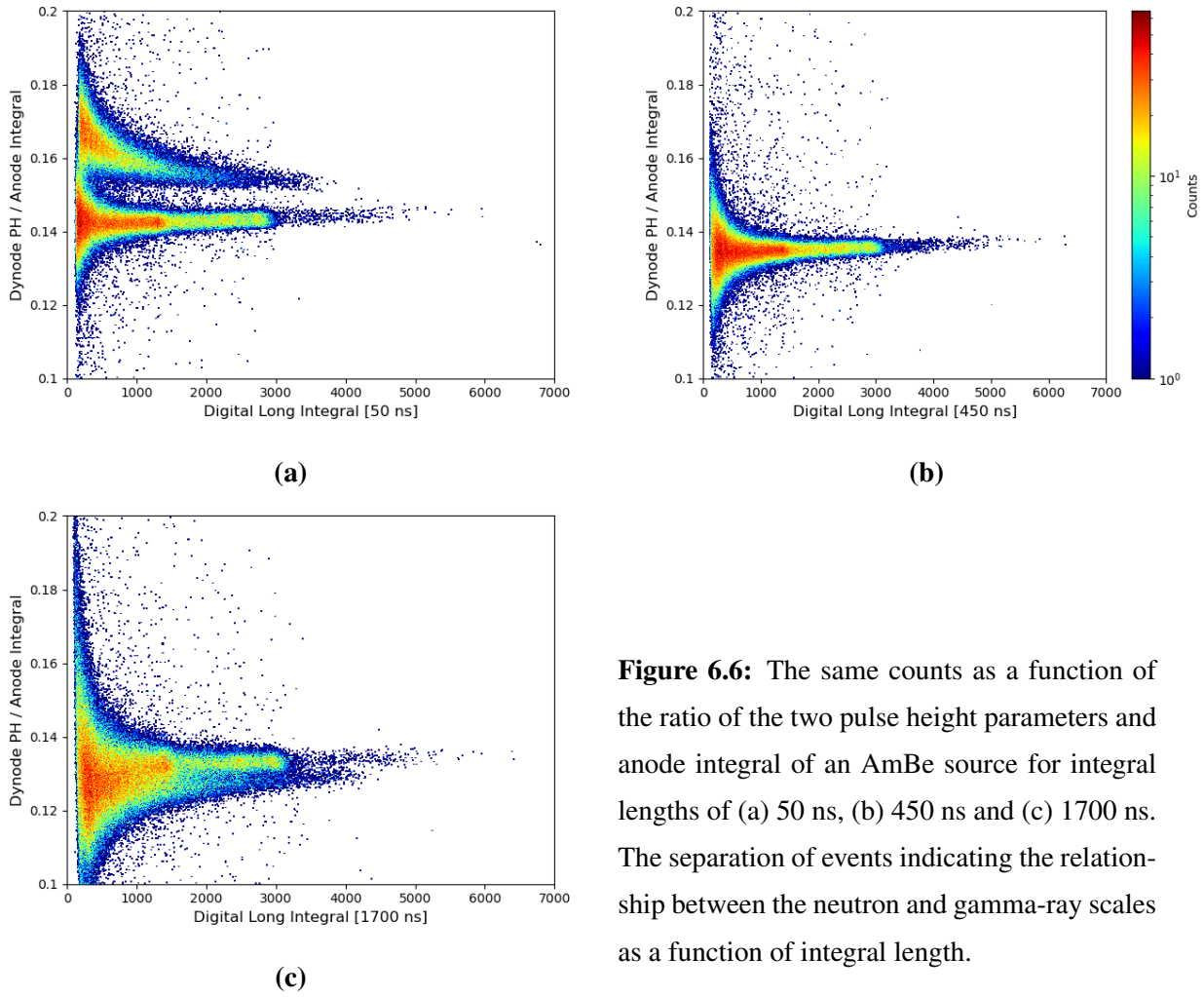

Figure 6.6: The same counts as a function of the ratio of the two pulse height parameters and anode integral of an AmBe source for integral lengths of (a) 50 ns, (b) 450 ns and (c) 1700 ns. The separation of events indicating the relationship between the neutron and gamma-ray scales as a function of integral length.

The integral length which results in the distributions converging allows a pulse height parameter to be determined which is proportional to the analogue neutron and gamma-ray pulse height parameter. This L would include the same relationship between the neutron MeV_{ee} and the gamma-ray MeV. Any separation in the ratio plotted in figure 6.6 is undesirable and will lead to incorrect neutron energy measurements through unfolding using the response functions calibrated through the analogue measurements.

Histograms of the ratio of the two pulse height parameters for three different long gate choices can be seen in figure 6.7 (a). The three different long gates show how the neutrons and the gamma-ray loci move as a function of long gate choice. The choice of 50 ns acts similarly to a short integral and essentially the ratio becomes a charge comparison and becomes equivalent to the pulse shape parameter used digitally. As this integral increases there is a point where the distributions merge and peak maximally. As the length of integral increases past this point the neutron distribution begins to separate from the gamma-ray peak and disperse due to the integral including a greater portion of noise. This plot demonstrates how the choice of long gate determines the relationship of the gamma-ray induced pulse height parameters to the neutron induced pulse height parameters.

In order to ensure that our digital pulse height parameter is the same as the analogue pulse height parameter we can determine when these two distributions converge.

Another way to determine the long gate which produces the best convergence is to consider the width of the distribution or the figure of merit of the two distributions, the width can be determined as the sum of the full width half maxes for the two distributions. A measure of the width of these two distributions as a function of long gate has been plotted in figure 6.7 (b), where the minimum was taken as the best estimate for the best choice for long gate and was determined to being 450 ns.

It is desirable to determine this long gate because the distribution in figure 6.6 show how the neutron locus is not entirely linear with pulse height at low pulse height values. This would mean when the distributions are not converged a non-linear scaling factor would need to be applied for accurate neutron measurements through unfolding. If a constant scaling factor would be applied to this distribution the neutron distribution would still disagree at lower energies. One can use the scaling factors $k_{lg}^{n/\gamma}$ obtainable from the peaks of distributions of the ratio of the pulse height parameters, as seen in figure 6.7 (a) and table 6.1, to account for any choice in long gate. Due to the non-linear behaviour of the neutrons at low pulse height values, the method which would result in the lowest uncertainty on the measurement would be to obtain the long gate that produces the best convergence in this ratio.

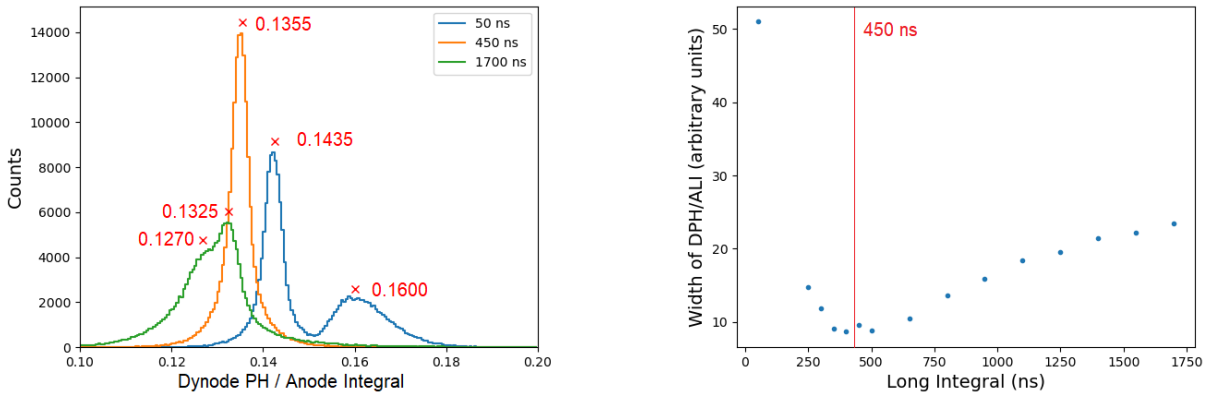

(a) **(b)**

Figure 6.7: Distributions of the ratio of the two pulse height parameters for three different long gate choices (a); 50 ns in blue, 450 ns in orange and 1700 ns in green. The effective width of this distribution has been plotted as a function of long gate (b) to determine the long gate which produces the best convergence of the two distributions, which was chosen to be 450 ns.

Table 6.1: Table of the scaling factors $k_{lg}^{n/\gamma}$ for the neutron and gamma-ray loci, respectively. Determined from the ratio of the dynode PH to the anode integral of an AmBe measurements (figure 6.7) for the integral length of 50 ns, 450 ns and 1700 ns.

Anode Integral Length (ns)	k_{lg}^{n}	k_{lg}^{γ}
50	0.1600(14)	0.1435(10)
450	0.1355(10)	0.1355(10)
1700	0.1270(21)	0.1325(13)

6.5 Results

The neutron light output and energy spectra are produced through the same means as the spectra from the data measured at AMANDE, detailed in chapters 3, 4 and 5. The neutron cuts were calculated in the same way and all pile up events were included in the spectra following. The unfolded energy spectra were determined using GRAVEL and MAXED.

6.5.1 14 MeV Neutrons

The MeV_{ee} calibrated light output spectra for the different three long gates (figure 6.6) have been plotted in figures 6.8 and 6.9 with the light output spectra produced from the dynode PH. The unscaled spectra, figure 6.8, are the raw calibrated light output spectra of the selected long gates. The scaled neutron light output spectra, figure 6.9, are the raw neutron light output spectra (figure 6.8) scaled by the factors determined in table 6.1 which were applied to the data before MeV_{ee} calibration. The effect of the long gate is most noticeable around the neutron edge for the unscaled spectra (figure 5.8) consequentially the unfolded results are inconsistent with each other as evident in figure 6.8 (b).

The unscaled unfolded neutron energy spectrum for the long gate of 1700 ns in figure 6.8 (b) has an abnormal addition to the expected single peak, it is unclear what produces this artefact. The scaled neutron light output and energy spectra, figure 6.9 (a) and (b) respectively, are in much better agreement than the unscaled results. In contrast to the unscaled unfolded results there is an anomaly in the scaled unfolded neutron energy spectrum determined using a long gate of 50 ns.

Applying the scaling factors obtained from the loci in figure 6.6(a) the edges align within uncertainty. The resultant peak centroids and their associated variances can be seen in table 6.2.

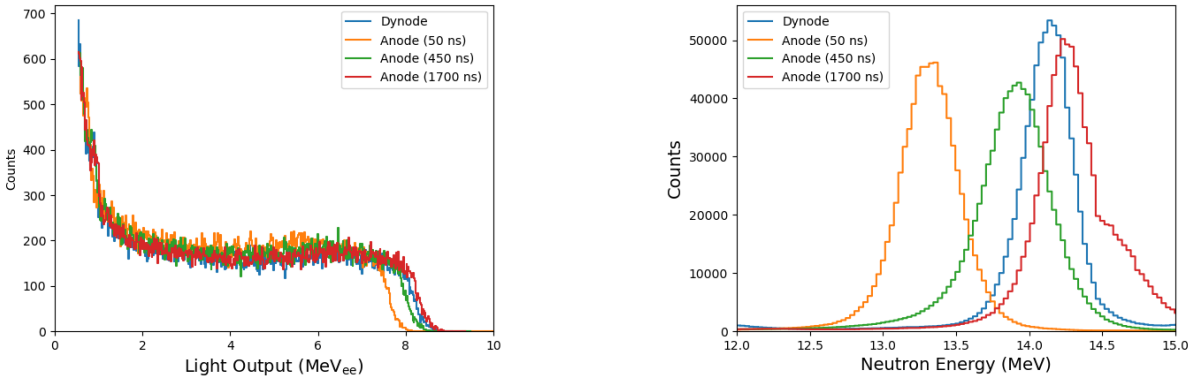

(a) **(b)**

Figure 6.8: Plots showing the unscaled MeV_{ee} calibrated light output spectra (a) and unfolded neutron energy spectra (b) for integral lengths of 50 ns, 450 ns and 1700 ns for the measurements made with the 14 MeV neutron beam at n-lab.

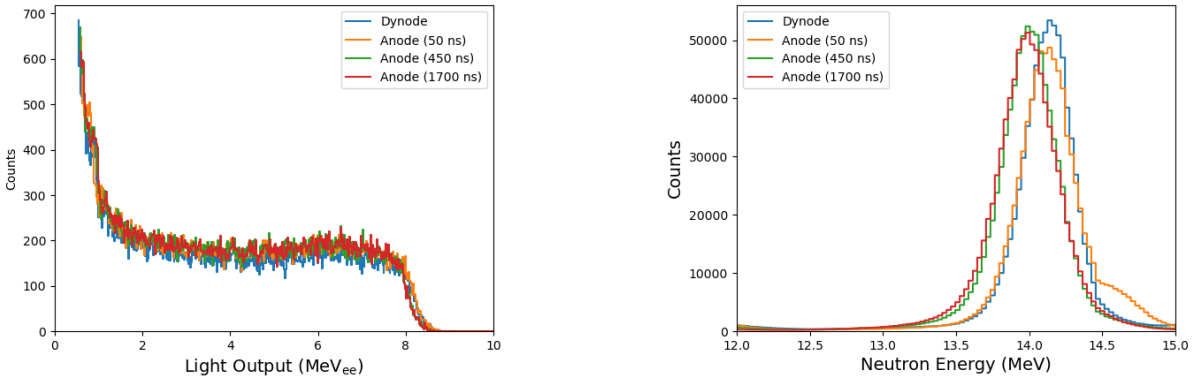

(a) **(b)**

Figure 6.9: Plots showing the scaled MeV_{ee} calibrated light output spectra (a) and unfolded neutron energy spectra (b) for integral lengths of 50 ns, 450 ns and 1700 ns, for the measurements made with the 14 MeV neutron beam and n-lab.

Table 6.2: The resultant peak centroids along with their standard deviations, measured from the MXD_MC33 unfolded neutron energy spectra presented in figure 6.9(b)

Spectrum	Peak Centroid [MeV]	Standard Deviation σ [MeV]
Dynode PH	14.14	0.18
Anode Integral (50 ns)	14.15	0.22
Anode Integral (450 ns)	14.02	0.20
Anode Integral (1700 ns)	14.00	0.22

The use of the data file with the two channel acquisition allows for one to determine the optimal long gate, relative to the analogue equivalent (dynode PH), for the lowest uncertainty measurements, along with its scaling factor without prior knowledge of the radiation field measured.

The dual channel acquisition set up requires one additional calibration measurement to determine the best long gate and scaling factor. This can be done with a calibration source which emits both neutrons and gamma-rays and applied to all other measurements, provided the detector is being operated within the recommend HV range where the response to the scintillation light is then linear with intensity.

The scaling factors obtained in the ratio of the pulse height parameters allows for one to correct for any choice of long gate. For the best measurements, with respect to preserving the line shape of the response functions, one should choose the long gate based on the convergence of the gamma-ray and neutron loci in the ratio of the two pulse height parameters.

6.5.2 ^{241}Am-^{9}Be

The same analysis applied to the ^{241}Am-^{9}Be radioisotopic calibration source data sets to investigate the effectiveness of such analysis across a larger neutron energy range. Figure 6.10 shows (a) the unscaled $\mathrm{MeV_{ee}}$ calibrated light output spectra for the dynode PH and the three chosen anode integrals, along with (b) the normalised unfolded results for the plotted light output spectra plotted in (a). As expected, the light output spectra do not align with each other and this influences the unfolded results, with the largest disagreement with the dynode PH neutron light output spectrum being the spectrum obtained using the anode with an integral time of 50 ns. The neutron light output spectra determined from the anode measurements with integral times of 450 ns and 1700 ns are in better agreement with the expected dynode PH neutron light output spectrum. The unfolding was completed with MXD_MC33 using the AmBe ISO standard fluence spectrum as the default.

The spectra can be compared through the use of the maximum difference Δ_m and coefficient of variation C_v. The maximum difference is used as a metric for the magnitude and nature of the largest difference between the distributions being compared. Defining $F_i(E)$ as the ith channel of the primary distribution F as a function of energy E and $G_i(E)$ as the ith channel of the distribution G, that is being compared to F, the maximum difference is defined as:

$$\Delta_m = max\left[F_i(E) - G_i(E)\right]_{i\in[0,N]}, \tag{6.9}$$

where N is the total number of channels.

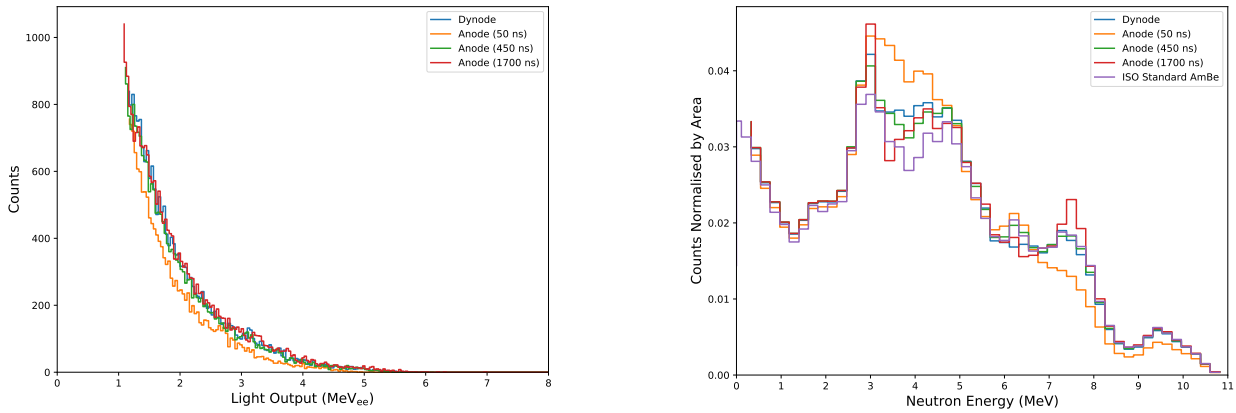

(a) **(b)**

Figure 6.10: Plots showing the unscaled MeV_{ee} calibrated light output spectra (a) and unfolded neutron energy spectra (b) of the AmBe measurements, for integral lengths of 50 ns, 450 ns and 1700 ns along with the AmBe ISO standard fluence spectrum.

Since Δ_m does not provide a measure of how well $G(E)$ agrees with $F(E)$, the coefficient of variation C_v, defined in equation 6.10, is used to determine the average deviation from $F(E)$.

$$C_v = \frac{1}{F(\bar{E})}\sqrt{\frac{\sum_{i=0}^{N}\left[F_i(E) - G_i(E)\right]^2}{N}} \tag{6.10}$$

The coefficient of variation produces a value of zero if $F(E) = G(E)$ and otherwise is presented as a percentage indicating how closely $G(E)$ follows $F(E)$ over the entire range, with respect to the mean of $F(E)$.

The dynode PH AmBe spectrum is defined as $F(E)$, and the final resultant anode integral unfolded spectra as $G(E)$. The results of the shape analysis for the unscaled AmBe unfolded spectra are presented in table 6.3.

Table 6.3: Table of the maximum differences (Δ_m) between the dynode PH AmBe spectrum and the unscaled measured unfolded spectra along with the coefficient of variation (C_v) for the difference between the two respective spectra.

Spectrum $G(E)$	Maximum Difference Δ_m	Coefficient of Variation C_v
Anode Integral (50 ns)	-0.0095	0.150
Anode Integral (450 ns)	-0.0029	0.043
Anode Integral (1700 ns)	0.0064	0.083

The coefficient of variation values presented in table 6.3 indicate, as expected, that the spectrum with the largest difference and variation in shape with the dynode PH AmBe spectrum is the anode integral of 50 ns. The spectrum with the smallest difference and the least variation off the expected is the anode integral of 450 ns. The coefficient of variation for the anode integral of 1700 ns is almost double that of the integral of 450 ns, indicating increased variation relative to the dynode PH spectrum.

The scaled MeV_{ee} calibrated light output spectra for the dynode PH and the three chosen anode integrals agree with each other, refer to figure 6.11(a). The corresponding unfolded spectra can be seen in figure 6.11(b) showing a much better agreement with the ISO standard spectrum than the unscaled results in figure 6.10(b).

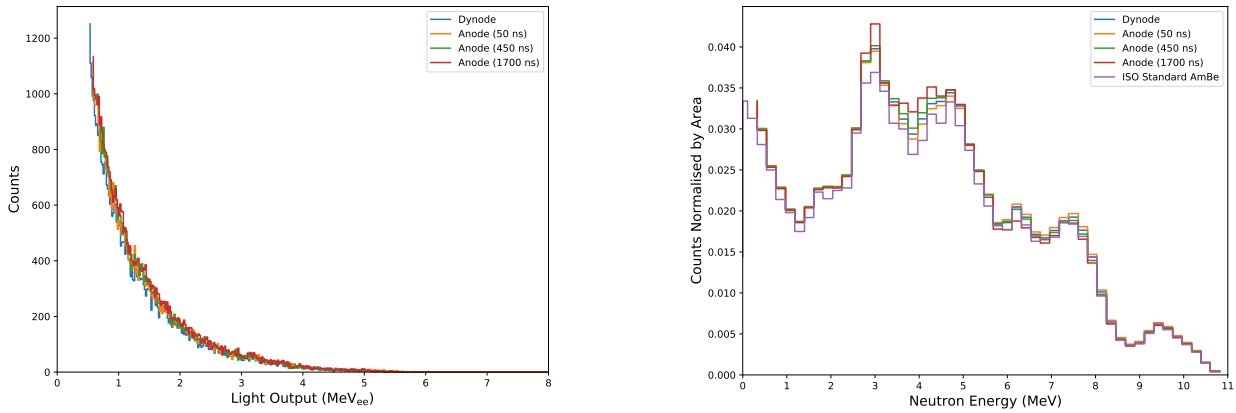

(a) **(b)**

Figure 6.11: Plots showing the scaled MeV_{ee} calibrated light output spectra (a) and unfolded neutron energy spectra (b) of the AmBe measurements, for integral lengths of 50 ns, 450 ns and 1700 ns along with the AmBe ISO standard fluence spectrum

The maximum differences and coefficient of variations for the scaled unfolded spectra in comparison with the dynode PH AmBe spectra can be found in table 6.4.

Table 6.4: Table of the maximum differences (Δ_m) between the dynode PH AmBe spectrum and the scaled measured unfolded spectra along with the co-efficient of variation (C_v) for the difference between the two respective spectra.

Spectrum $G(E)$	Maximum Difference Δ_m	Coefficient of Variation C_{nu}
Anode Integral (50 ns)	0.0052	0.082
Anode Integral (450 ns)	0.0039	0.059
Anode Integral (1700 ns)	-0.0019	0.032

Comparing the tables 6.3 and 6.4 there is an improvement in the C_v and Δ_m due to the scaling for the anode integrals of 50 ns and 1700 ns, while for the anode integral of 450 ns they worsened by a small amount. The energy spectra with the largest disagreement after scaling is the anode integral of 50 ns, with all spectra on the same order of magnitude for both C_v and Δ_m. The spectrum with the smallest Δ_m and C_v after scaling is the spectrum determined using the integral length of 1700 ns.

The unfolded AmBe spectra are all close in shape to the ISO standard due to it being used as the default spectrum and none of the solutions iterating to further than 3 iterations off the default. This is not a rigorous demonstration of the behaviour across energy but rather a demonstration that the solution is better behaved after scaling. Investigations with mono-energetic beams over a large range in energy would be better suited to further determine the behaviour of this method of scaling.

6.6 Simplified Scaling

The above method allows for the determination of scaling factors without requiring a mono-energetic beam measurement, however, if one has a mono-energetic beam measurement at a known energy value, a χ^2 minimisation can be applied to measurements to ensure agreement between the anode light output spectrum and the measured dynode pulse height spectrum. This fitting should provide a scaling factor for the MeV_{ee} scale which can be applied to the rest of the measured data.

For the same unscaled raw MeV_{ee} calibrated neutron light output spectra and unfolded spectra plotted in figure 6.8 (a), a scaling factor is applied to the MeV_{ee} scale of the desired light output spectra to match the scale of the 14.1 MeV measured dynode spectrum. The scaled spectra need to be re-binned accordingly to be comparable across measurements. The results of this scaling can be seen in figure 6.12, along with the associated measured peak centroid and standard deviation in table 6.5.
The presented unfolded results required the unfolded dynode PH resultant unfolded fluence spectrum to be used as the default spectrum in order for MXD_MC33 to converge. The solutions, with a flat default spectrum, were unable to converge to a well fitted solution.

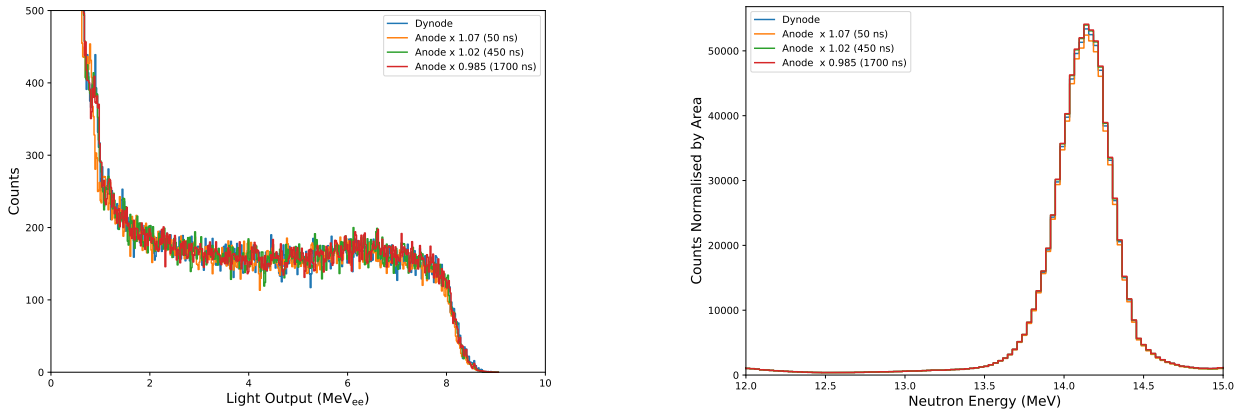

(a) **(b)**

Figure 6.12: Plots showing the scaled MeV_{ee} calibrated light output spectra (a) and unfolded neutron energy spectra (b) for integral lengths of 50 ns, 450 ns and 1700 ns, for the measurements made with the 14 MeV neutron beam and n-lab, with scaling factors of 1.070, 1.020 and 0.985 respectively.

Table 6.5: The resultant peak centroids along with their amplitudes and standard deviations, measured from the MXD_MC33 unfolded neutron energy spectra presented in figure 6.12(b)

Spectrum $G(E)$	Peak Centroid [MeV]	Peak Amplitude Counts $\times 10^4$	Standard Deviation σ [MeV]
Dynode PH	14.14	4.92	0.18
Anode Integral (50 ns)	14.14	4.83	0.18
Anode Integral (450 ns)	14.14	4.98	0.18
Anode Integral (1700 ns)	14.14	4.99	0.18

There is excellent agreement between the different scaled light output spectra. The only significant difference between the spectra can be seen in the small shoulder, due to the alpha contribution, occurring at around 1 MeV_{ee} for the anode measurement with an integral time of 50 ns. This difference at lower MeV_{ee} values implies that a single constant scaling factor applied to any anode integral will not correct across the entire energy range. This agrees with the plot in figure 6.6 where the neutron distributions centroid changes as a function of pulse height parameter, in the distributions obtained from the ratio of the anode measured integral to the dynode PH, resulting in non-Gaussian neutron distributions in figure 6.7 (a). This would imply that a non-linear scaling factor may be needed to ensure agreement across the energy range.

The unfolded spectra presented in figure 6.12(b) appear identical. Since the results are very dependent on the dynode PH unfolded neutron energy spectrum, the results all closely agree with the centroid, amplitude and and standard deviation of the dynode PH spectrum. All unfolded results had a χ^2/dof value of 1.4. The results being not varying much between each other could indicate that MAXED is not iterating from the default solution, this would require further measurements to investigate and verify these results.

Applying the same scaling factors to the AmBe data, the resultant scaled AmBe measurement can be seen in figure 6.13 along with the maximum differences and coefficient of variations are presented in table 6.6. The unfolded neutron energy spectra presented were only able to converge on a reasonable result using the ISO standard spectrum as the default spectrum. All spectra presented in figure 6.13(b) were not allowed to iterate more than 3 times off of the default spectrum.

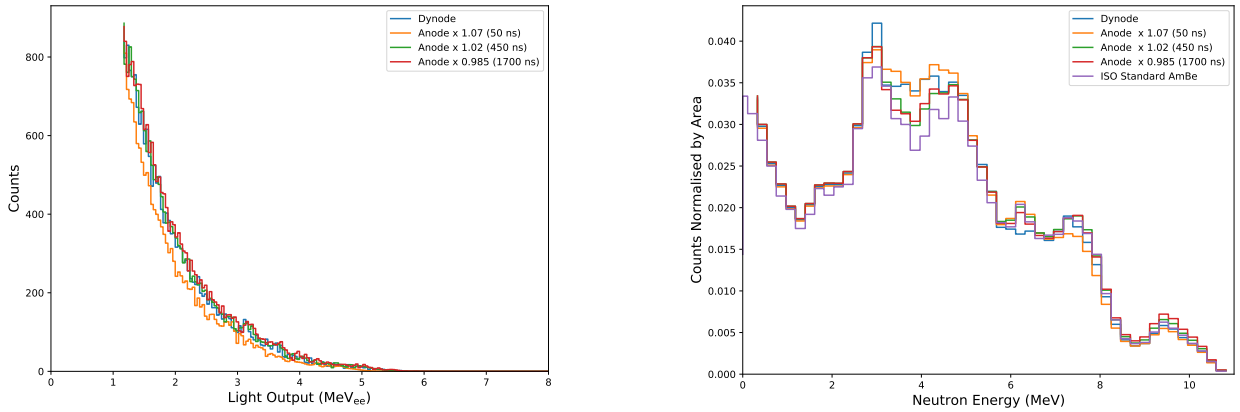

(a) **(b)**

Figure 6.13: Plots showing the scaled MeV_{ee} calibrated light output spectra (a) and unfolded neutron energy spectra (b) of the AmBe measurements, for integral lengths of 50 ns, 450 ns and 1700 ns along with the AmBe ISO standard fluence spectrum, with the scaling factors of 1.070, 1.020 and 0.985 respectively.

The light output spectra do not entirely agree with each other, implying the scaling factors determined through the scaling of the 14.1 MeV measurement do not work entirely across all energies, when integration times are either extremely long or short. Despite this, in comparison with the results presented in table 6.3 there is an improvement in the agreement with the dynode PH spectrum as presented in table 6.6. The spectrum associated with an anode integral of 450 ns produced the largest Δ_m and C_v. While all the spectra have Δ_m and C_v of the same orders of magnitude the spectrum with the smallest average variation relative to the dynode PH spectrum is the spectrum produced with an anode integral of 50 ns.

Table 6.6: Table of the maximum differences (Δ_m) between the Dynode PH spectrum and the scaled measured unfolded spectra along with the co-efficient of variation (C_v) for the spectra presented in figure 6.13b, with the scaling factors of 1.070, 1.020 and 0.985 respectively.

Spectrum $G(E)$	Maximum Difference Δ_m	Coefficient of Variation C_{nu}
Anode Integral (50 ns)	-0.0039	0.056
Anode Integral (450 ns)	0.0042	0.064
Anode Integral (1700 ns)	0.0036	0.062

This scaling method provides a quicker and easier alternative to the method presented in the previous section, and produces essentially equivalent results. The only significant difference is the dependency on a known mono-energetic beam measurement and the slight non-linearity introduced through a constant scaling factor. Both methods indicate the ability to use any choice of long integral as a comparable pulse height parameter L, with an associated scaling factor.

Acquiring energy information through the dynode PH while acquiring the anode for further information would be the simplest solution to ensuring measurements made with a digitiser produce the same MeV_{ee} scale as the analogue measurements, however this would result in the files acquired becoming unreasonably large for simple measurements. Thus these methods for determining the long gate or associated scaling factors are required for acquisition with the anode. Additional pulse height parameters such as a triangular filter have not been considered in this work and would need to be investigated in future. Another solution would be to determine response functions through a digitally measured empirical calibration this would yield the correct resultant neutron energy spectra through unfolding.

7. Discussion

A number of comparisons are possible from the results derived from the MPA-3 and DT5730 systems. A quantitative shape comparison of the measurements presented in chapters 4 and 5 allows for further discussion on the two acquisition systems. The metrics used for comparing the shapes of the different measured distributions are the Figure-of-Merit (FoM), coefficient of variation (C_v, equation 6.10) and maximum difference (Δ_m, equation 6.9).

The FoM values provide a method to evaluate the quality of separation of the neutron and gamma-ray distributions in the *L*-*S* density plots. For more on the definition of the FoM refer to section 5.1.2.

In this context, the coefficient of variation (C_v) is a measure of the how far the residuals differ from zero on average, relative to the average of one of the spectra. This metric has been used in the context of nuclear physics in the medical industry [116]. The maximum difference provide information on the size and nature of the largest disagreement between the distributions.

7.1 Pulse Shape Discrimination

Event density plots of pulse shape parameter (S) against the light output parameter (L) for the standard intensity measurements made with the MPA-3 and DT5730 acquisition systems, for the neutron energies of 1.200 MeV, 2.500 MeV, 5.000 MeV and 7.000 MeV are presented in figure 7.1.

The S parameter measured by the MPA-3 system is determind through the zero crossing method while the S calculated from the data acquired with the DT5730 digitiser is based on the charge comparison method. Both of these methods have been detailed in section 2.2.

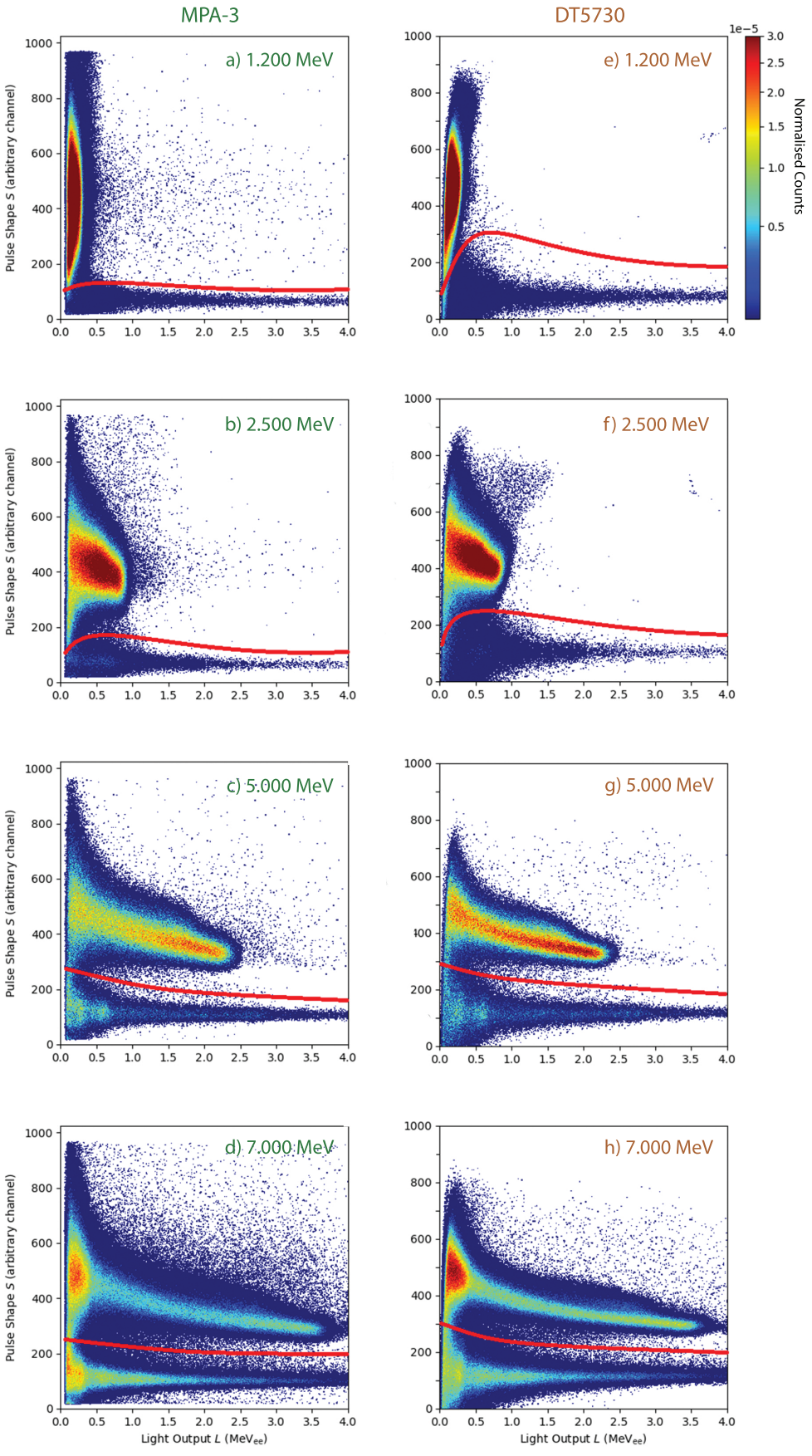

Figure 7.1: Events as a function of S and L for the measurements made at standard beam intensities for the four measured neutron energies: 1.200 MeV; 2.500 MeV; 5.000 MeV and 7.000 MeV for the MPA-3 (a to d) and DT5730 (e to h) acquisition systems. The PSD cuts that were applied to each of the plots are indicated by the red lines.

The scales of S in figure 7.1 are arbitrary as the digitally acquired S can be scaled with a simple multiplication factor (equation 2.7). The distributions are seen to be consistent with each other, with the only obvious difference being the distribution of pile up events, due to the different method of calculating S between the two systems.

A Figure-of-Merit (FoM) is a useful way to compare these measurements since these density plots are used to separate the distributions associated with gamma-ray and neutron induced interactions. For a FoM value greater than one the loci are considered separable. The FoM changes as a function of L, thus in order to compare the plots produced from data acquired with the two different acquisition systems the FoM values were calculated from slices along the L-axis of width 0.1 MeV_{ee}. The uncertainty in this value has been propagated through from a fit uncertainty in the centroid and FWHM of the distribution. Figure 7.2 shows the FoM as a function of L for the measurement made with neutrons at 7.000 MeV with the standard intensity, for the two different acquisition systems.

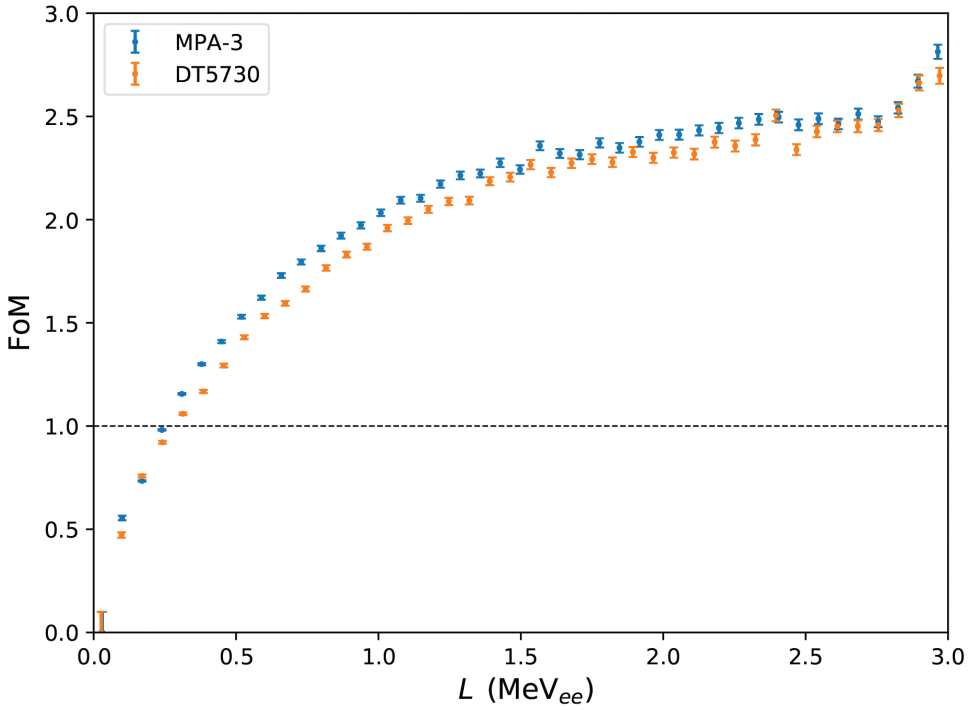

Figure 7.2: The FoM as a function of energy for the measurements at 7.000 MeV with the MPA-3 and DT5730 acquisition systems.

From figure 7.2 the quality of separation of the neutron and gamma-ray loci is seen to be marginally better for the measurements made with the MPA-3 acquisition system for reasons which are not fully understood and require further investigation.

7.2 Light Output and Energy Spectra

Neutron light output spectra were compared for the measurements made at standard intensities with the MPA-3 and the DT5730 acquisition systems for a 1.200 MeV, 2.400 MeV, 5.000 MeV and 7.000 MeV neutron beams. Figure 7.3 shows the measured spectra and residuals (R_i) determined by subtracting the spectrum measured with the DT5730 digitiser (D_i) from the MPA-3 measurement (M_i) as indicated in equation 7.1.

$$R_i = D_i - M_i \tag{7.1}$$

The largest differences in the measured neutron light output spectra occur at low MeV_{ee} values, near the threshold limit and at the upper edge of the spectra. This difference is expected due to the complications in the choice of the long gate for the digital measurements. The residuals plotted (fig. 7.3) indicate that the upper edges are in better agreement for the lower neutron energy measurements.

The resolution of the edge can not be accurately commented on for the 1.2 MeV measurement due to the edge being near to the threshold limit, however the residuals of the 2.5 MeV measurement indicate that the analogue measurements have a better resolution.

The difference in the upper edge changes the MeV_{ee} range in which the spectra have been normalised. The digitally measured spectra typically have an edge of a lower MeV_{ee} value than the analogue spectra the digital spectra and thus, in the 5.000 MeV and 7.000 MeV spectra, have a higher normalised counts along the plateau region of the spectra. The undershooting in the residuals is then an artefact of normalisation.

The metrics used to further compare the spectra are the coefficient of variation (C_v) and maximum difference (Δ_m). Table 7.1 presents these values for the spectra being compared in figure 7.3.

The spectrum with the largest coefficient of variation and residual when compared with the MPA-3 measurement is the DT5730 measurement at 1.200 MeV. This is not surprising as the upper edge of the neutron light output spectra for these measurements is very close to the applied acquisition threshold. The spectra which demonstrate the best agreement with each other are those at a neutron energy of 5.000 MeV.

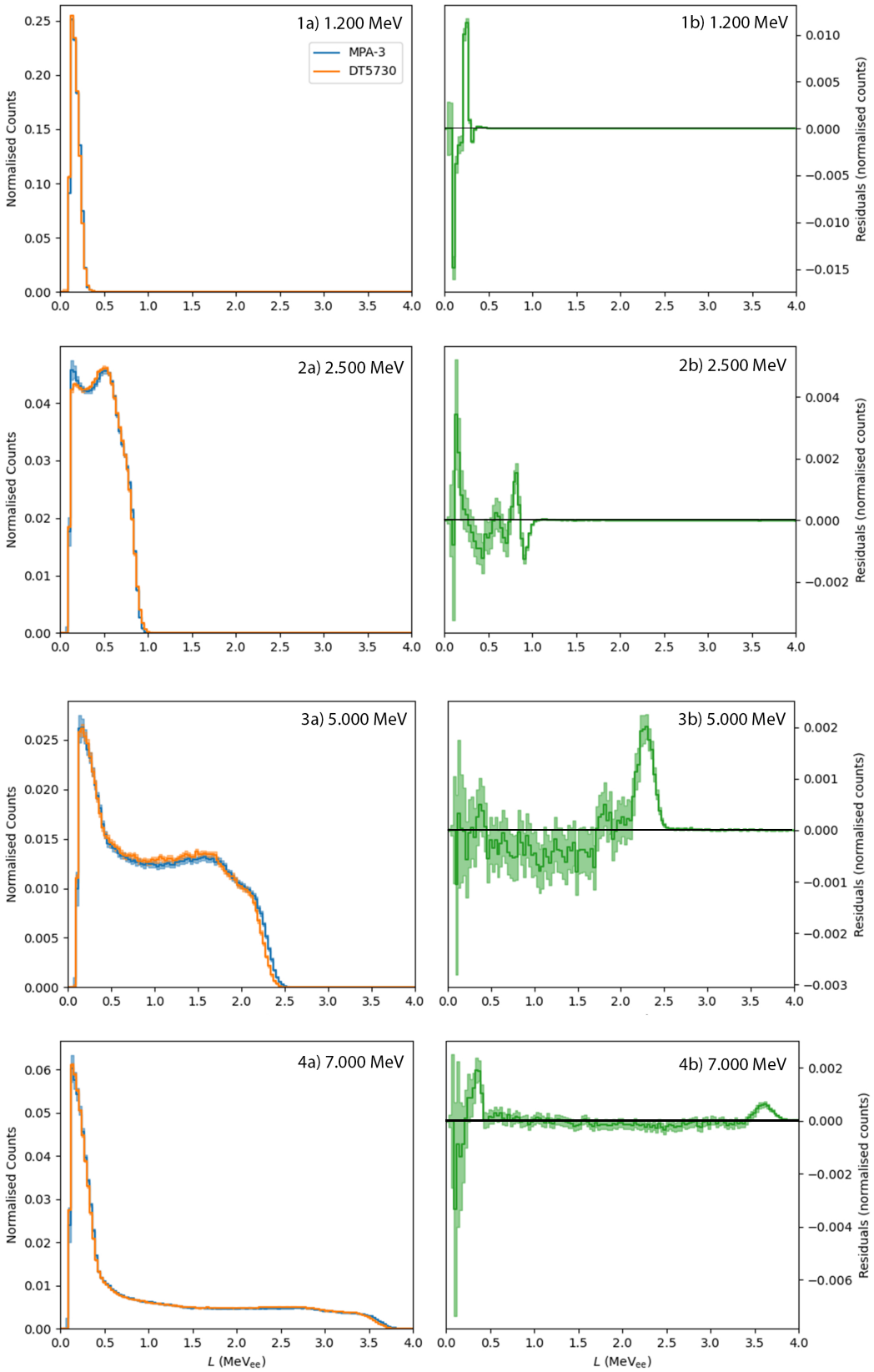

Figure 7.3: Measured light output spectra normalised to an area of one (a) and residuals (b) for the same beam conditions as measured by the MPA-3 and DT5730 acquisition system. The measurements presented are the standard intensities at 1) 1.200 MeV, 2) 2.500 MeV, 3) 5.000 MeV and 4) 7.000 MeV neutron beam energies. The relative uncertainties have been included, represented by the shaded regions around the counts and the residuals.

Table 7.1: The calculated metrics (coefficient of variation (C_v) and maximum difference (Δ_m)) for the standard intensity measurements of the neutron light output spectra for neutron beam energies of 1.200 MeV, 2.500 MeV, 5.000 MeV and 7.000 MeV, measured for both acquisition systems. All calculations presented assume the MPA-3 measurement as the primary function with the DT5730 measured spectrum being compared to it. The maximum (red) and minimum (blue) of each of the metrics have been indicated with text color in the table.

$E^{calc}_{n,peak}$ [MeV]	Beam Current [μA]	C_v %	Δ_m
1.200(3)	4.520	26.6	-0.0148
2.500(4)	0.540	6.8	0.0034
5.000(3)	0.590	7.1	0.0020
7.000(6)	0.574	6.7	-0.0033

A similar analysis can be applied to the measured neutron energy spectra, where the unfolded neutron spectra for the MPA-3 and DT5730 measurements are shown together with their residuals in figure 7.4. The residuals were calculated by subtracting the DT5730 measurement from the MPA-3 measurement. The correction to the energy scale has been applied to the spectra as discussed in chapter 4 and 5.

The largest difference between the spectra presented in figure 7.4 is due to the offset between the primary peaks. The centroids of the unfolded neutron energy spectra measured with the DT5730 digitiser appear at a higher energy to the MPA-3 centroids. The difference in amplitudes are an artefact of the normalisation. The digitally acquired spectra have a slightly broader primary peak indicating a better resolution for the analogue acquired spectra. The largest difference in primary peak is produced by the 7.000 MeV measurement. This agrees with the results presented for the neutron light output spectra (fig. 7.3) as the difference in upper edge would follow through the unfolding process resulting in different mean energy.

Similarly to the difference between the measured light output spectra (figure 7.3), the difference in centroid value is primarily due to the difference in the neutron MeV_{ee} scale.

The same metrics of comparison that were used for the neutron light output spectra were used for the unfolded energy spectra and are presented in table 7.2. The 1.200 MeV measurements produce the smallest relative coefficient of variation and maximum difference, implying the best agreement between the two measured spectra. The 2.500 MeV measurements have the largest coefficient of variation and maximum difference. The measurements for 5.000 MeV and 7.000 MeV have similar coefficients of variation and maximum differences, indicating a similar quality and good agreement between the spectra.

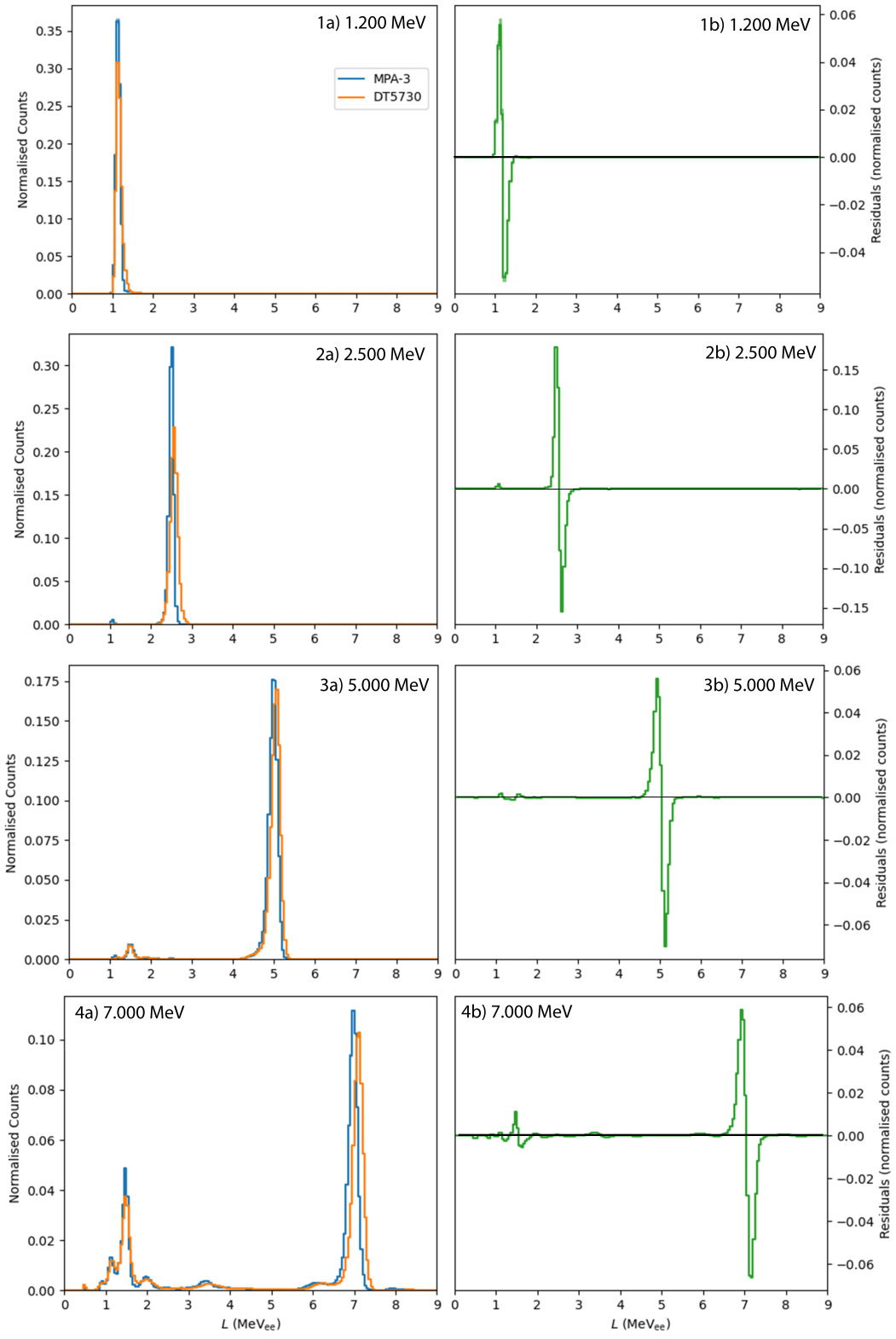

Figure 7.4: Measured neutron energy spectra (a) along with their residuals (b), for the same beam conditions as measured by the MPA-3 and DT5730 acquisition systems. The measurements presented are the standard intensities at 1) 1.200 MeV, 2) 2.500 MeV, 3) 5.000 MeV and 4) 7.000 MeV neutron beam energies.

Table 7.2: Calculated metrics (coefficient of variation (C_v) and maximum difference (Δ_m)) for the measurements of the neutron energy spectra for neutron beam energies of 1.200 MeV, 2.500 MeV, 5.000 MeV and 7.000 MeV. The maximum (red) and minimum (blue) of each of the metrics have been indicated with text color in the table.

$E_{n,peak}^{calc}$ [MeV]	Beam Current [μA]	C_v %	Δ_m
1.200(3)	4.520	152.5	0.056
2.500(4)	0.540	435.1	0.179
5.000(3)	0.590	194.4	-0.070
7.000(6)	0.574	213.4	-0.066

7.3 Uncertainty Budget Comparison

The analogue measured neutron energies have two significant sources of uncertainty. The one is associated with the uncertainty in the MeV_{ee} calibration, $u\left(E_{n,peak}^{obs,MPA}\right)$, and the other is due to the scaling factor introduced to correct for outdated response functions, $u\left(k_{RM}\right)$. Similarly, the two factors accounted for in the digitally measured neutron energies are the MeV_{ee} calibration uncertainty, $u\left(E_{n,peak}^{obs,DT5730}\right)$, and the scaling factor introduced to correct for the choice of long gate, $u\left(k_{RMD}\right)$. The final uncertainty is then a combination of these two factors, as seen in equation 7.2

$$u\left(E_{n,peak}^{obs,MPA/DT5730}\right) = E_{n,peak}^{meas,MPA/DT5730}\sqrt{\left[\frac{u\left(E_{n,peak}^{obs,MPA/DT5730}\right)}{E_{n,peak}^{obs,MPA/DT5730}}\right]^2 + \left[\frac{u\left(k_{RM/RMD}\right)}{k_{RM/RMD}}\right]^2} \tag{7.2}$$

The values used to calculate the final measured neutron energies and their associated uncertainties are included in table 7.3. The values for the uncertainty are of the same order of magnitude for all the measurements except for the 7.000 MeV measurement. However, the values for the uncertainty in $E_{n,peak}^{obs,MPA}$ are consistently smaller than those for $E_{n,peak}^{obs,DT5730}$.

The final measured energies and their standard uncertainties have been tabulated along with the expected energies in table 7.4, showing that the resultant final energy measurements do agree with each other within one standard uncertainty.

The fluence measurements made are unfortunately unable to be compared due to several complications.

Table 7.3: The measured values for $k_{RM/RMD}$ and $E_{n,peak}^{obs,MPA/DT5730}$ and their associated uncertainties for the MPA-3 and DT5730 standard intensity measurements.

	MPA-3	DT5730
$k_{RM/RMD}$	0.954(15)	0.9812(97)
$E_{n,1.200}^{obs}$	1.200(20)	1.160(30)
$E_{n,2.500}^{obs}$	2.636(16)	2.632(59)
$E_{n,5.000}^{obs}$	5.235(25)	5.150(85)
$E_{n,7.000}^{obs}$	7.320(32)	7.24(12)

Table 7.4: Final neutron energy measurements from the unfolded spectra presented in figure 7.4 along with the expected values of the neutron energies calculated from beam conditions.

Expected Neutron Energy [MeV]	1.200(30)	2.500(4)	5.000(3)	7.000(6)
DT5730 Measured Energy [MeV]	1.160(30)	2.582(63)	5.053(97)	7.10(14)
MPA-3 Measured Energy [MeV]	1.145(26)	2.515(42)	4.994(82)	6.98(11)

7.4 Time-of-Flight measurements

Time-of-Flight (ToF) measurements were made with the BC501A detector using both the CAEN DT5730 digitiser and the standard analogue acquisition system coupled with the MPA-3 multi-parameter analyser. Preliminary results are presented for a calculated neutron energy of 17.00(72) MeV, produced by 1.380 MeV deuterons incident on a 2045 µg cm^{-2} TiT target. The stop pulse frequency for these measurements was 2.00 MHz and the time calibration was determined to be 2.23 channel per ns for the MPA-3 measurements and 1.00 channel per ns for the DT5730 measurements. The time zero channel (t_0), for the time-of-flight parameter (T), was calculated from the centroid channel of the gamma-ray peak.

The measured T-spectra are presented in figure 7.5 for three different detector distances for (a) the MPA-3 and (b) DT5730 systems.

The neutron energy spectra were calculated as described in section 2.3.2 and are presented in figure 7.6. The spectra have an energy binning of 0.5 MeV and have been corrected for the efficiency of the detector at a threshold of 0.25 MeV_{ee}.

The numerical results for the neutron energies have can be found in table 7.5, where the neutron energies (E_n) and their associated FWHM/E_n (ΔE_n) have been tabulated for each of the distances and acquisition system. All the measured results agree within one standard uncertainty with the expected value.

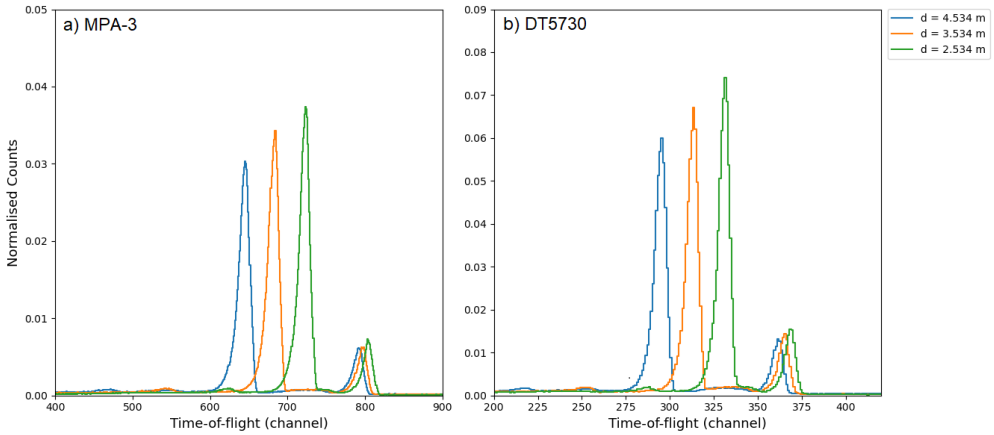

Figure 7.5: Time-of-flight spectra measured with the (a) MPA-3 and (b) DT5730 for the BC501A detector, placed at three distances from the edge of a the TiT target for the 17.00 MeV neutron beam. The spectra have been normalised to an integral of unity and the gamma-ray peaks are evident in the regions of (a) 800 ch and (b) 360 ch.

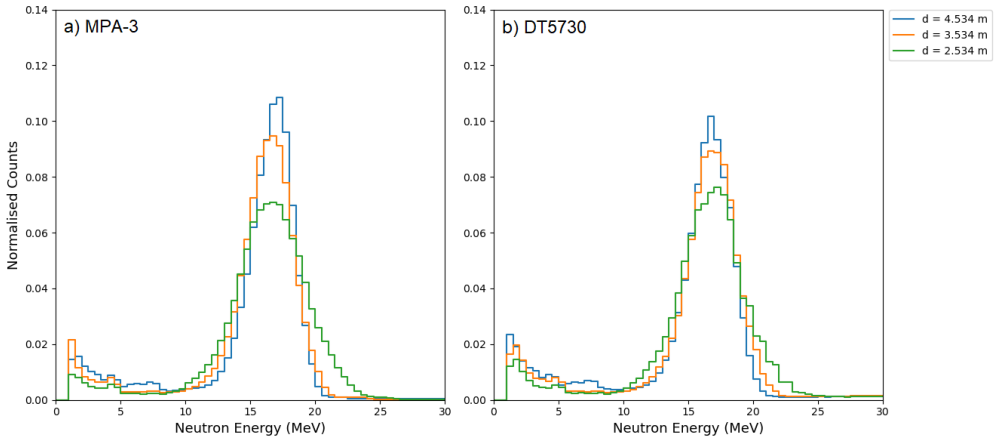

Figure 7.6: Neutron energy spectra measured via ToF with the (a) MPA-3 and (b) DT5730 for the BC501A detector, placed at three distances from the edge of a the TiT target for the 17.00 MeV neutron beam. The spectra have been normalised to an integral of unity after being corrected for the efficiency of the detector at a threshold of 0.25 MeV_{ee}.

Table 7.5: Neutron energies as determined from the ToF spectra for 17.00 MeV neutrons measured with a BC501A detector with the two acquisition systems for 3 distances.

Distance [m]		4.534(68)	3.534(54)	2.534(40)
MPA-3	E_n [MeV]	17.04	16.72	16.90
	ΔE_n [MeV]	0.17	0.21	0.30
DT5730	E_n [MeV]	17.02	17.15	17.07
	ΔE_n [MeV]	0.18	0.21	0.26

8. Conclusion

Investigations have been completed into the suitability of a CAEN DT5730 digitiser unit, coupled with the QtDAQ software, as viable alternative to a traditional analogue system for data acquisition for fast neutron metrology. Previous investigations into the use of digitisers for neutron metrology by Lebreton in 2007 [117] have resulted in mixed conclusions. Experiments were completed at the fast neutron facilities of AMANDE (IRSN, Cadarache) using a BC501A scintillation detector and both the DT5730 digitiser and an analogue system based on NIM electronics and an MPA-3 multi-channel analyser acquisition unit, under identical conditions using a broad range of beam conditions available at the AMANDE facility. Follow-up measurements were made at the n-lab facility at the University of Cape Town.

The main focus of the analyses was the unfolding of measured light output spectra to determine the neutron energy distributions of the neutron fields. Detailed investigations were made into the dead time characteristics of the DT5730 unit, and uncertainty budgets for both systems were used as the basis of the comparisons between the two systems. Preliminary results for measurements with neutron time-of-flight have also been presented, although future measurements should include a wider range of beam conditions.

The quality of pulse shape discrimination for both systems is very similar (figure 7.1), with the difference in the distributions of the pile-up being attributed to the different ways in which the pulse shape parameter S is derived in each case. The quality of separation of the neutron and gamma-ray induced events was quantified using a Figure-of-Merit (FoM) value, which were also very similar to each other as expected (figure 7.2), although further exploration of digital pulse shape parameters is necessary.

Furthermore, the measured energy spectra from unfolding analyses achieved in both systems are in good agreement with each other with respect to both peak energy and spectral fluence, although a comparison with reference values was not possible due to unresolvable inconsistencies in the analogue pulse processing. Comparison of the uncertainty budgets for the two systems indicates similar quality of measurement result, with the DT5730 uncertainties being consistently larger by a few percent.

The fact that the response functions used for the analyses were not well matched to the measured data does not detract from these conclusions since reasonable corrections were applied consistently to both systems to mitigate this.

For the digitally acquired measurements, there is non-linear behaviour between the choice of long gate in the definition of the light output parameter and the proportionality to the light output parameter measured by the analogue acquisition system. There needs to be a reliably scaled light output parameter L from the anode pulses, which is consistent for both gamma-ray and neutron events. A reliable calibration of the neutron light output spectra in MeV_{ee} is a prerequisite for producing accurate energy spectra from the subsequent unfolding analyses. In the analogue system the *L* parameter is determined from the (voltage) pulse height of the amplified dynode pulse. In the DT5730 system, the unamplified anode pulse is used which does not provide a reliable *L* parameter from the "pulse height" due the sharp rise time of the anode pulse. Therefore, the *L* parameter is determined from a (long) integral of the anode pulse, typically between 500 ns and 1000 ns, depending on the detector. The selection of the long integration time is thus critical if a reliable calibration of the *L* parameter is to be achieved. Although post-acquisition corrections may be applied to ensure this, a more direct method was explored in follow-up measurements at the n-lab at the University of Cape Town (Chapter 6). It was shown that one solution is to record both the anode pulse (for pulse shape discrimination) and the dynode pulse (for light output) in coincidence, as is done when using the MPA-3 system. This increases the size of the list mode file by a factor of about 12. It was thus demonstrated that it is sufficient to calibrate the anode channel to the dynode channel in order to either determine either the appropriate long integral for the anode pulse, or the (single) factor by which an unoptimized long integral needs to be scaled. Further work on possible definitions of the digital light output parameter, such as a trapezoidal filter [13] for a digital light output parameter may offer an alternative method to derive a stable light output parameter.

Another factor which influenced the precision of the energy measurements made at AMANDE with the DT5730 digitiser is that the analogue pulser correction unit remained operational throughout. This unit dynamically adjusts the high voltage power supply to correct for gain drifts in the analogue light output parameter (*L*).

A coarse gain pulser correction was developed and presented (Chapter 5). A fine gain pulser correction was also developed (see Appendix C) which may improve the resolution of the edge of the neutron light output spectra in the digitally measured spectra.

A considerable advantage of the DT5730 digitiser over the MPA-3 acquisition system is the effective zero event loss while operating below the buffer saturation level. After buffer saturation occurs events lost increases linearly, although these may be corrected for until an additional dead time affect becomes apparent. Further investigations are required to fully correct for these effects. Pile-up events are also a contributing factor to the loss of events.

At low rates this correction is small but at increasing rates this factor become significant. A broad correction for these events has been applied in this work, however the digitally acquired waveforms provide the potential to deconvolve the overlaid pulses and analyse all peaks within an acquired window. This method requires further work to be implemented but has already been used in several contexts [118, 119]. Separating the pulses within one acquisition window and processing them as individual events would allow for the loss of events due to pile up to be reduced to effectively zero.

In conclusion, the measurements reported here made with a CAEN DT5730 system, and the Qt-DAQ software, suggest that modern digital systems are now offering a reliable alternative to the well characterized reference acquisition systems based on analogue NIM modules. A compact digital unit also offers the advantage of deploying the same metrology reference system in both laboratory and field environments. The present measurements were made with the DT5730 module connected by USB-2 cable to a regular laptop. Further improvements in stability, reliability and performance would be gained by utilising the optical cable connection between the DT5730 and an appropriate desktop PC. The present investigations have shown that there is now value in seriously considering implementation of a digital acquisition system for fast neutron metrology in a laboratory setting. Further experiments are planned to advance these investigations under conditions that better represent the standard beam and acquisition setups for fast neutron metrology measurements at the AMANDE facility, and elsewhere.

Bibliography

[1] D. J. Thomas, R. Nolte, and V. Gressier. What is neutron metrology and why is it needed? *Metrologia*, 48(6):S225–S238, 2011.

[2] R. Nolte, M. S. Allie, R. Böttger, F. D. Brooks, A. Buffler, and et al. Quasi-monoenergetic neutron reference fields in the energy range from thermal to 200 MeV. *Radiation Protection Dosimetry*, 110(1-4):97–102, 2004.

[3] R.C. Block, Y. Danon, F. Gunsing, and R.C. Haight. *Neutron Cross Section Measurements*, pages 1–81. Springer US, Boston, MA, 2010.

[4] A. Carlson. The neutron cross section standards, evaluations and applications. *Metrologia*, 48:S328, 2011.

[5] F.D. Brooks and H. Klein. Neutron spectrometry—historical review and present status. *Nuclear Instruments and Methods in Physics Research*, 476:1–11, 2002.

[6] G. Dietze and H. Klein. NRESP4 and NEFF4: Monte Carlo codes for the calculation of neutron response functions and detection efficiencies for NE 213 scintillation detectors. Technical Report PTB-ND-22, Braunschweig Univ. Phys.-Tech. Bundesanst, Braunschweig, 1982.

[7] MCNP User Manual. `https://mcnp.lanl.gov/mcnp_manual.shtml`, 2017. (Accessed on 06/03/2021).

[8] G. Bonheure, M. Angelone, R. Barnsley, L. Bertalot, and et al. Neutron diagnostics for reactor scale fusion experiments: a review of JET systems. *Proceedings of Science*, 2006.

[9] O.N. Jarvis. Neutron measurement techniques for tokamak plasmas. *Plasma Physics and Controlled Fusion*, 36(2):209–244, 1994.

[10] G. Ericsson. Advanced neutron spectroscopy in fusion research. *Journal of Fusion Energy*, 38:330–355, 2019.

[11] V.A. Fedorov, Y.A. Kashchuk, E.S. Martazov, Y.A. Parishkin, N.A. Selyaev, and V.A. Vorobiev. Study of the data acquisition system for ITER divertor neutron flux monitor diagnostic. *IEEE Transactions on Nuclear Science*, 67(4):688–693, 2020.

[12] N. Zaitseva, B. Rupert, I.A. Pawełczak, A. Glenn, and et al. Plastic scintillators with efficient neutron/gamma pulse shape discrimination. *Nuclear Instruments and Methods in Physics Research.*, 668:88–93, 2012.

[13] CAEN Team. *Application Note AN2508: CAEN Digital Pulse Height Analyser - a digital approach to Radiation Spectroscopy*. CAEN, Viareggio, Italy, 2011.

[14] CAEN. Digital Spectroscopy - CAEN - Tools for Discovery. `https://www.caen.it/sections/digital-spectroscopy/`. (Accessed on 02/18/2020).

[15] XIA. Nuclear spectroscopy products. `https://xia.com/dgf_products.html`. (Accessed on 02/18/2020).

[16] NI. PXI IF Digitizer - NI. `https://www.ni.com/en-za/shop/hardware/products/pxi-if-digitizer.html`. (Accessed on 01/18/2021).

[17] Teledyne SP Devices. SP Devices - Products - High-speed Digitizers/Oscilloscopes & ADC IP for Silicon & FPGA. `https://www.spdevices.com/products`. (Accessed on 01/18/2021).

[18] D. Marocco, M. Riva, B. Esposito, L. Bertalot, and A. Zimbal. A digital data acquisition system optimized for spectrometry with liquid scintillation detectors. *Proceedings of Science*, 025, 2007. International Workshop on Fast Neutron Detectors and Applications (FNDA2006).

[19] L. X. Liu, H. W. Wang, Y. G. Ma, X. G. Cao, X. Z. Cai, Justin G. Chen, G. L. Zhang, J. L. Han, J. F. Hu, Xian Hai Wang, and H. J. Fu. A data acquisition system based on root and waveform digital technology for photo-neutron source. *arXiv: Instrumentation and Detectors*, 2017.

[20] ENEA. ENEA-Fusion:Electric & Electronic Engineering: Real Time Systems. `http://www.fusione.enea.it/INGELE/rtdaps.html.en`. (Accessed on 01/18/2021).

[21] L. Giacomelli, A. Zimbal, M. Reginatto, and K. Tittelmeier. Evaluation of a digital data acquisition system and optimization of n-γ discrimination for a compact neutron spectrometer. *Review of Scientific Instruments*, 82(1):013505, 2011.

[22] M. Riva, B. Esposito, D. Marocco, F. Belli, and B. Syme. The new digital electronics for the jet neutron profile monitor: Performances and first experimental results. *Fusion Engineering and Design*, 86(6):1191–1195, 2011. Proceedings of the 26th Symposium of Fusion Technology (SOFT-26).

[23] Keysight. U1082A 8-bit High-Speed PCI Digitizers with On-Board Signal Processing. https://www.keysight.com/zz/en/product/U1082A/8bit-highspeed-pci-digitizers-with-onboard-signal-processing.html. (Accessed on 06/04/2021).

[24] F. Saglime, Y. Danon, and R. Block. Digital data acquisition system for time of flight neutron beam measurements. *The American Nuclear Society's 14th Biennial Topical Meeting of the Radiation Protection and Shielding Division*, 2006.

[25] P.F. Mastinu, U. Abbondanno, and G. Aerts et al. Neutron cross section measurements at n-TOF for ADS related studies. *Journal of Physics: Conference Series*, 41:352–360, 2006.

[26] A. Borella, G. Aerts, F. Gunsing, M. Moxon, and et al. The use of C6D6 detectors for neutron induced capture cross-section measurements in the resonance region. *Nuclear Instruments and Methods in Physics Research*, 577(3):626–640, 2007.

[27] M. Flaska and S.A. Pozzi. Identification of shielded neutron sources with the liquid scintillator BC-501A using a digital pulse shape discrimination method. *Nuclear Instruments and Methods in Physics Research*, 577(3):654–663, 2007.

[28] A. Enqvist, M. Flaska, and S. Pozzi. Measurement and simulation of neutron/gamma-ray cross-correlation functions from spontaneous fission. *Nuclear Instruments and Methods in Physics Research*, 595(2):426–430, 2008.

[29] A. Danagoulian, W. Bertozzi, C.L. Hicks, and et al. Prompt neutrons from photofission and its use in homeland security applications. In *2010 IEEE International Conference on Technologies for Homeland Security (HST)*, pages 379–384, 2010.

[30] J. Uher, J. Jakubek, U. Koster, and et al. Detection of fast neutrons with the medipix-2 pixel detector. *Nuclear Instruments and Methods in Physics Research*, 591(1):71–74, 2008. Radiation Imaging Detectors 2007.

[31] C.L. Fontana, N. Tuccori, F.E. Pino, and et al. Performance comparison between signal digitizers and low-cost digital oscilloscopes: spectroscopic, pulse shape discrimination and timing capabilities for nuclear detectors. *Journal of Instrumentation*, 15(06):P06020–P06020, 2020.

[32] G. Tian, X. Ouyang, H. Qu, and et al. Digital n/γ discrimination measurement of low intensity pulsed neutron. *He Jishu/Nuclear Techniques*, 38, 2015.

[33] H. Mavromichalaki, Victor Yanke, L. Dorman, and et al. *Neutron Monitor Network in Real Time and Space Weather*, volume 176, pages 301–317. 2006.

[34] D.T. Strauss, S. Poluianov, C. van der Merwe, and et al. The mini-neutron monitor: A new approach in neutron monitor design. *Journal Space Weather Space Climate*, 10, 2020.

[35] Teach, Learn, and Make with Raspberry Pi. `https://www.raspberrypi.org/`. (Accessed on 05/09/2021).

[36] Internal Report TM-1805383. `https://nucleus.iaea.org/sites/nuclear-instrumentation/Documents/Internal%20Report_TM-1805383_final.pdf`, 2019.

[37] G.F. Knoll. *Radiation Detection and Measurement*, chapter 2: Radiation Interactions, pages 53–55. Wiley, 4 edition, 2010.

[38] F.D. Brooks. Development of organic scintillators. *Nuclear Instruments and Methods in Physics Research*, 162(1):477–505, 1979.

[39] G.F. Knoll. *Radiation Detection and Measurement*, chapter 15.3: Detectors That Utilize Fast Neutron Scattering, pages 569–594. Wiley, 4 edition, 2010.

[40] A.H. Compton. The spectrum of scattered x-rays. *Physical Review*, 22:409–413, 1923.

[41] G.F. Knoll. *Radiation Detection and Measurement*, chapter 2.1: Interaction of Heavy Charged Particles, pages 30–41. Wiley, 4 edition, 2010.

[42] Q. Jianguo, L. Caifeng, Y. Bangjiao, and et al. Characterizations of BC501A and BC537 liquid scintillator detectors. *Applied Radiation and Isotopes*, 104:15–24, 2015.

[43] G. Laustriat. The luminescence decay of organic scintillators. *Molecular Crystals*, 4(1-4):127–145, 1968.

[44] F.Q.L. Friesen and C.R. Howell. A functional form for liquid scintillator pulse shapes. *Nuclear Instruments and Methods in Physics Research*, 955:163302, 2020.

[45] T. Murai, T. Nakamura, and A. Yamamoto. A New Method of Integral Dose Measurement with a Plastic Scintillator Phantom**. *Journal of Radiation Research*, 5(1):23–34, 1964.

[46] J.B. Birks. Scintillations from Organic Crystals: Specific Fluorescence and Relative Response to Different Radiations. *Proceedings of the Physical Society A*, 64:874–877, 1951.

[47] G.F. Knoll. *Radiation Detection and Measurement*, chapter 8: Scintillation Detector Properties, pages 223–274. Wiley, 4 edition, 2010.

[48] N. Nakao, T. Kurosawa, T. Nakamura, and Y. Uwamino. Absolute measurements of the response function of an NE213 organic liquid scintillator for the neutron energy range up to 206 MeV. *Nuclear Instruments and Methods in Physics Research*, 463(1):275–287, 2001.

[49] G. Dietze and H. Klein. Gamma-calibration of NE213 scintillation counters. *Nuclear Instruments and Methods in Physics Research*, 193(3):549–556, 1982.

[50] G.T. Wright. Scintillation decay times of organic crystals. *Proceedings of the Physical Society. Section B*, 69(3):358–372, 1956.

[51] F.D. Brooks. *Liquid Scintillation Counting*, page 268. Pergamon, London, 1958.

[52] T.K. Alexander and F.S. Goulding. An amplitude-insensitive system that distinguishes pulses of different shapes. *Nuclear Instruments and Methods in Physics Research*, 13:244–246, 1961.

[53] R.ST. Onge, A. Galonsky, R.K. Jolly, and T.M. Amos. Organic-scintillator pulse-shape discriminator signatures associated with high-energy neutrons. *Nuclear Instruments and Methods in Physics Research*, 126(3):391–395, 1975.

[54] M.L. Roush, M.A. Wilson, and W.F. Hornyak. Pulse shape discrimination. *Nuclear Instruments and Methods in Physics Research*, 31(1):112–124, 1964.

[55] P. Sperr, H. Spieler, M.R. Maier, and D. Evers. A simple pulse-shape discrimination circuit. *Nuclear Instruments and Methods in Physics Research*, 116(1):55–59, 1974.

[56] 2160A. `https://www.fastcomtec.com/nim/2160a`. (Accessed on 02/09/2020).

[57] Z.W. Bell. Tests on a digital neutron-gamma pulse shape discriminator with ne213. *Nuclear Instruments and Methods in Physics Research*, 188(1):105–109, 1981.

[58] M. Moszynski, G. Bizard, G.J. Costa, and et al. Study of n-γ discrimination by digital charge comparison method for a large volume liquid scintillator. *Nuclear Instruments and Methods in Physics Research*, 317(1):262–272, 1992.

[59] Y. Kaschuck and B. Esposito. Neutron/γ-ray digital pulse shape discrimination with organic scintillators. *Nuclear Instruments and Methods in Physics Research*, 551(2):420–428, 2005.

[60] B. Esposito, Y. Kashchuk, A. Rizzo, L. Bertalot, and A. Pensa. Digital pulse shape discrimination in organic scintillators for fusion applications. *Nuclear Instruments and Methods in Physics Research*, 518:626–628, 2004.

[61] D. Wolski, M. Moszyński, T. Ludziejewski, and et al. Comparison of n-γ discrimination by zero-crossing and digital charge comparison methods. *Nuclear Instruments and Methods in Physics Research*, 360(3):584–592, 1995.

[62] B. Wan, X.-Y. Zhang, L. Chen, and et al. Digital pulse shape discrimination methods for n-γ separation in an EJ-301 liquid scintillation detector. *Chinese Physics C*, 39(11):116201, 2015.

[63] P.A. Söderström, J. Nyberg, and R. Wolters. Digital pulse-shape discrimination of fast neutrons and γ rays. *Nuclear Instruments and Methods in Physics Research*, 594(1):79–89, 2008.

[64] R. Aryaeinejad, J.K. Hartwell, and D.F. Spencer. Comparison between digital and analog pulse shape discrimination techniques for neutron and gamma ray separation. In *IEEE Nuclear Science Symposium Conference Record, 2005*, pages 500–504, 2005.

[65] R.F. Lang, D. Masson, J. Pienaar, and S. Röttger. Improved pulse shape discrimination in EJ-301 liquid sctintillators. *Nuclear Instruments and Methods in Physics Research*, 856, 2016.

[66] Y. Yun, L. Guofu, Y. Jun, and L. Xiaoliang. The digital discrimination of neutron and γ ray using organic scintillation detector based on wavelet transform modulus maximum. *Chinese Physics C*, 38, 2013.

[67] M. Safari, F. Abbasi davani, H. Afarideh, S. Jamili, and E. Bayat. Discrete fourier transform method for discrimination of digital scintillation pulses in mixed neutron-gamma fields. *IEEE Transactions on Nuclear Science*, 63:325–332, 2016.

[68] R.F. Lang, D. Masson, J. Pienaar, and S. Röttger. Improved pulse shape discrimination in EJ-301 liquid sctintillators. *Nuclear Instruments and Methods in Physics Research*, 856, 2016.

[69] F. C. E. Teh, J.-W. Lee, K. Zhu, K. W. Brown, and Z. Chajecki et al. Value-assigned pulse shape discrimination for neutron detectors. *IEEE Transactions on Nuclear Science*, 68(8):2294–2300, 2021.

[70] T.S. Sanderson, C.D. Scott, M. Flaska, J.K. Polack, and S.A. Pozzi. Machine learning for digital pulse shape discrimination. In *2012 IEEE Nuclear Science Symposium and Medical Imaging Conference Record (NSS/MIC)*, pages 199–202, 2012.

[71] S. Andaloro, G.V. Rogachev, and J. Hooker. Using Machine Learning to Improve Gamma-Neutron Discrimination in P-terphenyl and ^{6}Li Glass Detectors. `https://meetings.aps.org/Meeting/HAW18/Session/HA.32`. (Accessed on 02/17/2021).

[72] G.F. Knoll. *Radiation Detection and Measurement*, chapter 18.5: Spectrum Analysis, pages 724–731. Wiley, 4 edition, 2010.

[73] J.T. Routti and J.V. Sandberg. *Unfolding Techniques for Activation Detector Analysis. In: Nelson W.R., Jenkins T.M. (eds) Computer Techniques in Radiation Transport and Dosimetry.*, volume vol 3 of *Ettore Majorana International Science Series (Physical Sciences)*. Springer, Boston, MA, 1980.

[74] M. Reginatto, P. Goldhagen, and S. Neumann. Spectrum unfolding, sensitivity analysis and propagation of uncertainties with the maximum entropy deconvolution code maxed. *Nuclear Instruments and Methods in Physics Research*, 476(1):242–246, 2002. Int. Workshop on Neutron Field Spectrometry in Science, Technolog y and Radiation Protection.

[75] M. Reginatto and P. Goldhagen. MAXED, a computer code for the deconvolution of multisphere neutron spectrometer data using the maximum entropy method. 1998. User Manual,url:https://www.osti.gov/biblio/663223.

[76] W.R. Burrus. *Utilization of a Priori Information by Means of Mathematical Programming in the Statistical Interpretation of Measured Distributions (Ph.D thesis)*. Oak Ridge National Laboratory, Report ORNL-3743 edition, 1965.

[77] R.H. Johnson and B.W. Wehring. FORIST unfolding code manual, 1976. ORNL/RSIC–40.

[78] A.K. McCracken and M.J. Grimstone. The experimental data processing program RADAK. *Commission of the European Communities*, 1977. EUR–5667(pt1).

[79] D. Slaughter and R. Strout. Flyspec: A simple method of unfolding neutron energy spectra measured with NE213 and stilbene spectrometers. *Nuclear Instruments and Methods in Physics Research*, 198(2):349–355, 1982.

[80] F.G. Perey. Least-squares dosimetry unfolding: the program STAY'SL. *Oak Ridge National Laboratory*, (ORNL/TM–6062), 1977.

[81] M. Shahmohammadi Beni, D. Krstic, D. Nikezic, and et al. Studies on unfolding energy spectra of neutrons using maximum-likelihood expectation–maximization method. *Nuclear Science Technology*, 30(134), 2019.

[82] R. Koohi-Fayegh, S. Green, N.M.J. Crout, and et al. Neural network unfolding of photon and neutron spectra using an NE-213 scintillation detector. *Nuclear Instruments and Methods in Physics Research*, 329(1):269–276, 1993.

[83] S.A. Hosseini and I.E.P. Afrakoti. Evaluation of a new neutron energy spectrum unfolding code based on an Adaptive Neuro-Fuzzy Inference System (ANFIS). *Journal of Radiation Research*, 59(4):436–441, 2018.

[84] H. Zhu, Y. Altmann, A.D. Fulvio, and et al. A hierarchical bayesian approach to neutron spectrum unfolding with organic scintillators. *IEEE Transactions on Nuclear Science*, 66(10):2265–2274, 2019.

[85] R. Koohi-Fayegh, S. Green, and M.C. Scott. A comparison of neutron spectrum unfolding codes used with a miniature ne213 detector. *Nuclear Instruments and Methods in Physics Research*, 460(2):391–400, 2001.

[86] M.A. Cognet and V. Gressier. Development of a measurement reference standard for neutron energies between 1 MeV and 20 MeV using time of flight method at the AMANDE facility. *Metrologia*, 47(4):377–386, 2010.

[87] J.W. Poston. Dosimetry. In Robert A. Meyers, editor, *Encyclopedia of Physical Science and Technology (Third Edition)*, pages 603–650. Academic Press, New York, third edition edition, 2003.

[88] V. Gressier, J.F. Guerre-Chaley, V. Lacoste, L. Lebreton, G. Pelcot, J. Pochat, T. Bolognese-Milstajn, and D Champion. Amande: A new facility for monoenergetic neutron fields production between 2 kev and 20 mev. *Radiation protection dosimetry*, 110:49–52, 2004.

[89] V. Gressier, B. Asselineau, J. F. Guerre-Chaley, A. Martin, and H. Müller. AMANDE Accelerator Performances. AMANDE Accelerator Energy Performances. *Proceedings of Science*, FNDA2006:061, 2006.

[90] V. Gressier, A.C. Bonaldi, M.S. Dewey, D.M. Gilliam, and et al. International key comparison of neutron fluence measurements in monoenergetic neutron fields: CCRI(III)-k11. *Metrologia*, 51(1A):06009–06009, 2014.

[91] V. Lacoste. Design of a new long counter for the determination of the neutron fluence reference values at the irsn amande facility. *Radiation Measurements*, 45:1250–1253, 2010.

[92] D. Schlegel. *TARGET's users manual*. Braunschweig, 2005. PTB-6.42-05-2.

[93] AMANDE facility. https://www.irsn.fr/EN/Research/Scientific-tools/experimental-facilities-means/Amande/Pages/Amande-facility.aspx. (Accessed on 06/09/2021).

[94] The AMANDE facility. https://www.irsn.fr/EN/Research/Scientific-tools/experimental-facilities-means/GF-amande-facility/Pages/default.aspx. (Accessed on 02/09/2020).

[95] A. Ohrn, J. Blomgren, H. Park, S. Khurana, R. Nolte, D. Schmidt, and K. Wilhelmsen. A monitor for neutron flux measurements up to 20 mev. *Radiation protection dosimetry*, 126:394–7, 2007.

[96] FastComtec. *Model MPA-3, PC-card Multiparameter Multichannel Analyzer System*.

[97] DT5730 / DT5730S - 8 Channel 14 bit 500 MS/s Digitizer - CAEN - Tools for Discovery. online: https://www.caen.it/products/dt5730/.

[98] A.C. Comrie, A. Buffler, F.D. Smit, and H.J. Wörtche. Digital neutron/gamma discrimination with an organic scintillator at energies between 1 mev and 100 mev. *Nuclear Instruments and Methods in Physics Research.*, 772:43–49, 2015.

[99] A. Buffler, A.C. Comrie, F.D. Smit, and H.J. Wörtche. A new compact neutron/gamma ray scintillation detector. *International Journal of Modern Physics: Conference Series*, 44, 2016.

[100] A. Comrie. qtdaq — bitbucket. https://bitbucket.org/veggiesaurus/qtdaq/src/master/.

[101] CoMPASS - Multiparametric DAQ Software for Physics Applications. https://www.caen.it/products/compass/.

[102] Qt — Cross-platform software development for embedded & desktop. https://www.qt.io/.

[103] Software Libraries - CAEN - Tools for Discovery. https://www.caen.it/subfamilies/software-libraries/.

[104] D. Schmidt, B. Asselineau, R. Böttger, and et al. Characterization of liquid scintillation detectors. *Nuclear Instruments and Methods in Physics Research*, 476:186–189, 2002.

[105] Z. V. P. Murthy. *Nonlinear Regression: Levenberg-Marquardt Method*, pages 1–3. Springer Berlin Heidelberg, Berlin, Heidelberg, 2015.

[106] D. Schmidt, B. Asselineau, R. Böttger, and et al. Characterization of liquid scintillation detectors. *Nuclear Instruments and Methods in Physics Research*, 476(1):186–189, 2002. Int. Workshop on Neutron Field Spectrometry in Science, Technolog y and Radiation Protection.

[107] V. Lacoste and V. Gressier. Experimental characterization of the irsn long counter for the determination of the neutron fluence reference values at the AMANDE facility. *Radiation Measurements*, 45(10):1254–1257, 2010. PROCEEDINGS OF THE 11TH SYMPOSIUM ON NEUTRON AND ION DOSIMETRY.

[108] C. Varignon, X. Ledoux, I. Lantuéjoul, G. Alloy, N. Arnal, and I. Bailly et al. A new neutron beam line for (n,xn) reaction studies. *Nuclear Instruments and Methods in Physics Research*, 248(2):329–335, 2006.

[109] R. Köhler. *The International Vocabulary of Metrology, 3rd Edition: Basic and General Concepts and Associated Terms. Why? How?*, pages 233 – 238. 2010. ISBN: 9780470611371.

[110] H. Spieler. Analog and digital electronics for detectors, 2006. Lecture notes, Berkley.

[111] T. Hutton and A. Buffler. A new D-T neutron facility at UCT. In *Proceedings of the 62nd South African Institute of Physics Conference*, 2017.

[112] Thermo Fisher Scientific Inc. Thermo Scientific MP 320: Product Specifications, 2007. `https://www.thermofisher.com/order/catalog/product/1517021A`.

[113] Eljen Technology. Neutron/Gamma PSD: EJ-301, EJ-309 data sheets, 2021. `https://eljentechnology.com/products/liquid-scintillators/ej-301-ej-309`.

[114] ET Enterprises. 9214B series data sheet, 2010. `https://et-enterprises.com/products/photomultipliers/product/p9214b-series`.

[115] G.F. Knoll. *Radiation Detection and Measurement*, chapter Appendix D: The Shockley-Ramo Theoren for Induced Charge, pages 813–818. Wiley, 4 edition, 2010.

[116] S.G. Levin. Understanding and using statistics in nuclear medicine. *The Journal Of Nuclear Medicine*, 20:550–558, 1979.

[117] L. Lebreton, J.F. Guerre-Chaley, D. Manuel, and et al. Performances of Digital Acquisition for a BC501A detector system. *Proceedings of Science*, FNDA2006:027, 2007.

[118] F. Belli, B. Esposito, D. Marocco, and et al. A method for digital processing of pile-up events in organic scintillators. *Nuclear Instruments and Methods in Physics Research*, 595(2):512–519, 2008.

[119] P.A.B. Scoullara, C.C. McLeana, and R.J. Evansb. Real Time Pulse Pile-up Recovery in a High Throughput Digital Pulse Processor. *AIP Conference Proceedings*, 1412(270), 2011.

A. The UMG Package

As described in section 2.3.1, unfolding is the process by which a neutron energy spectrum is determined through the deconvolution of a detectors inherent response functions from a measured combined neutron pulse height spectrum. The energy spectrum of the neutron source measured can be determined from the measured pulse height spectrum by solving the system of linear equations:

$$z_i = \int_0^\infty R_i(E)\phi(E)dE, \tag{A.1}$$

where $i \in [1,m]$ is the subscript referring to the channel number of the measurement with a total of m channels, z_i represents the measured neutron light output spectrum in channel i, $R_i(E)$ are the response functions for energy E in the ith channel and $\phi(E)$ are the average fluence values in the interval of $E \in [E_i, E_{i+1}]$. Writing this as a discretised matrix equation:

$$z = \mathbf{R}\Phi, \tag{A.2}$$

where the z column vector is the measured pulse height spectrum with associated uncertainties given by the co-variance matrix $\mathbf{S_z}$ which is diagonal. The matrix $\mathbf{R}$ is the response matrix which is assumed to be known with little uncertainty, leaving the column vector Φ needing to be solved for. The uncertainties are then able to be propagated through this unfolding calculation producing uncertainties in the final unfolded neutron energy spectrum Φ.

A best estimate for Φ can be determined through χ^2 minimisation, where χ^2 is defined as the weighted sum of residuals:

$$\chi^2 = \sum_i W_i \left[z_i - \sum_j R_{ij}\phi_j \right]^2, \tag{A.3}$$

the weighting factors W_i being the inverse of the variance of each data point. The minimisation process can be executed through a least squares algorithm, such as the minimisation algorithm implemented by GRAVEL, or through more advanced algorithms to reduce the likelihood of non-physical features and negative elements in the solution.

MAXED relies on a maximum entropy algorithm, allowing for an *a priori* to be taken into consideration. MAXED includes an error column vector in equation A.2 being the difference between the

predicted and measured values of the neutron light output spectrum. This is then constrained by:

$$\sum_i \frac{\varepsilon_i^2}{u(z_i)^2} = \Omega, \tag{A.4}$$

where $u(z_i)^2$ is the standard uncertainty in the ith element of the z column vector, ε_i is error between the predicted and measured values for the ith channel in the neutron light output spectrum and Ω is a free parameter chosen by the user. The function minimised by MAXED is given by:

$$S = -\sum_j \left[\phi_j ln\left(\frac{\phi_j}{\phi_j^{def}} \right) + \phi_j^{def} - \phi_j \right], \tag{A.5}$$

where ϕ_j^{def} is the provided default spectrum. This calculation allows for the uncertainties in the solution ϕ_i, u(ϕ_i), to be determined through a type A analysis and is provided through the ICQU code included in the UMG package.

B. Analogue Varying Intensities

The counts as a function of pulse shape S and pulse height L normalised by area to aid in comparison can be seen in figure B.1 and B.2 for the nominal neutron energies of 2.500 MeV and 5.000 MeV.

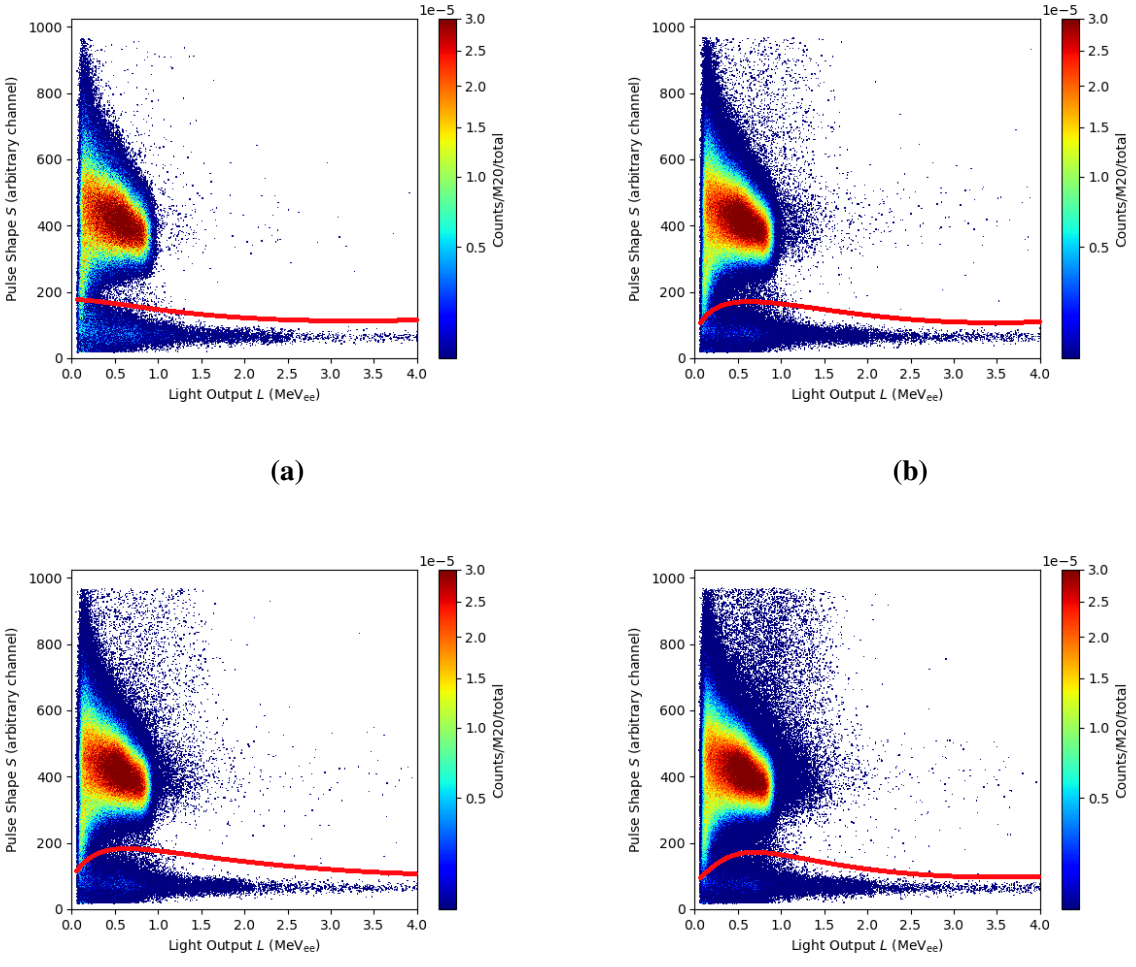

Figure B.1: Counts as a function of S and L measured with the analogue acquisition system for four neutron fields with a nominal energy of 2.500 MeV for beam currents of (a) 0.108 µA; (b) 0.540 µA; (c) 1.130 µA and (d) 2.770 µA. The plots also include the cut applied used to separate the gamma-ray and neutron induced events.

As with the 7.000 MeV data sets shown in the text, the measurements all exhibit the same features with the increase in pile up with intensity being the difference between the measurements.

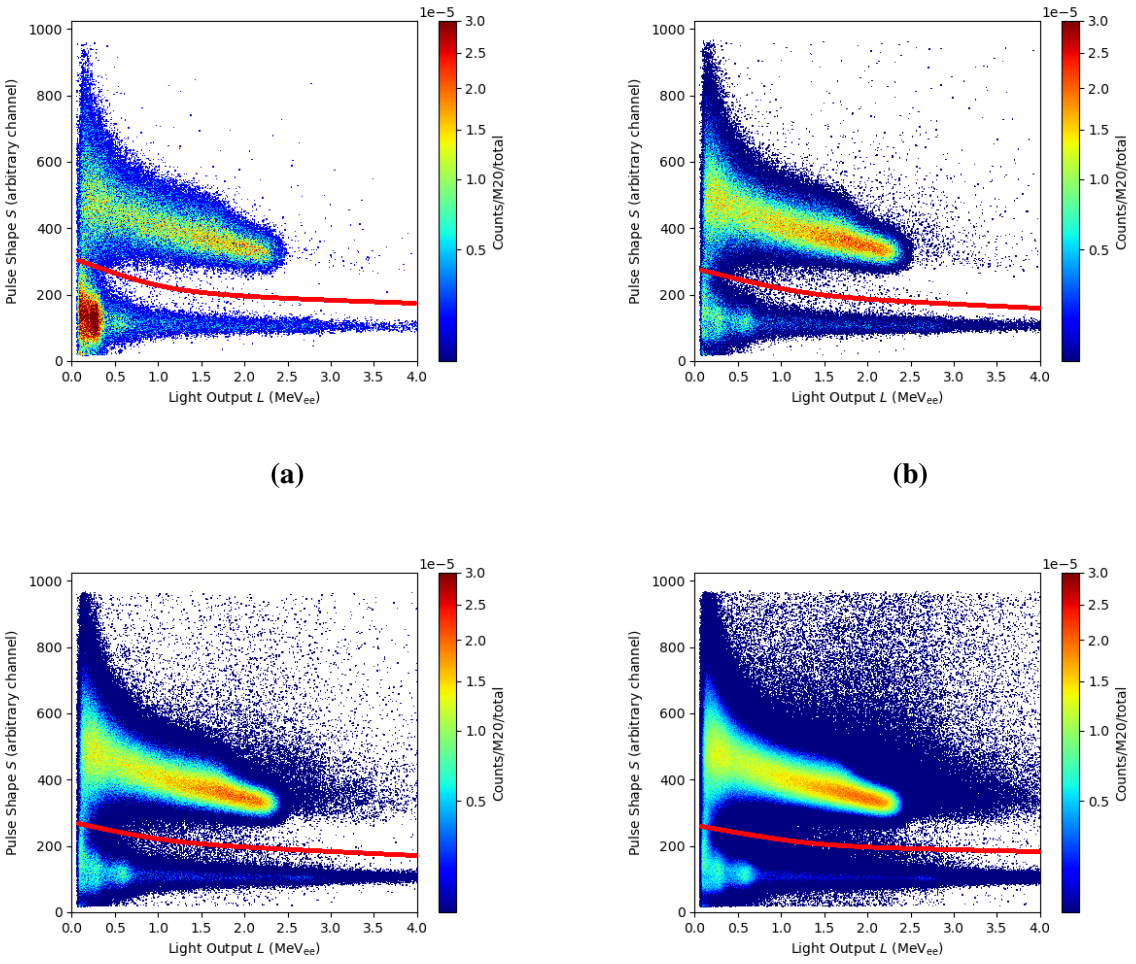

(a) **(b)**

(c) **(d)**

Figure B.2: Counts as a function of S and L measured with the analogue acquisition system for four neutron fields with a nominal energy of 5.000 MeV for beam currents of (a) 0.135 µA; (b) 0.590 µA; (c) 2.560 µA and (d) 5.060 µA. The red line indicating the cut applied used to separate the gamma-ray and neutron induced events.

The raw peak neutron fluences, $\Phi^{obs}_{E,peak}$, for each of the beam conditions, along with the associated scaling factors k_{MPA}, k_{PU} and Q, can be found in tables B.1, B.2 and B.3.

Table B.1: Scaling factors that make us k_{DT} for the peak neutron fluence calculation for each of the different beam intensities for the nominal energy of 2.500 MeV

Beam Current (μA)	0.108	0.540	1.130	2.770
M20 count rate (counts s^{-1})	51.90(18)	220.09(55)	415.90(96)	1051.9(24)
k_{MPA}	1.0028(40)	1.011(29)	1.021(28)	*1
k_{PU}	1.0004(10)	1.00108(73)	1.0019(16)	1.0042(11)
Q (μC)	216.080(15)	423.231(21)	671.289(82)	379.743(62)
$\Phi^{obs}_{E,\,peak}$ ($\times 10^4 cm^{-2}$)	*11.88	*30.11	*23.52	34.95777(52)

Table B.2: Scaling factors that make us k_{DT} for the peak neutron fluence calculation for each of the different beam intensities for the nominal energy of 5.000 MeV

Beam Current (μA)	0.135	0.590	2.560	5.060
M20 count rate (counts s^{-1})	18.35(14)	82.02(36)	358.37(95)	701.0(10)
k_{MPA}	*1	1.0053(62)	1.0229(24)	1.04526(91)
k_{PU}	1.00047(51)	1.0009(33)	1.0024(15)	1.00386(93)
Q (μC)	‘110.204(10)	369.793(19)	1085.73(10)	3845.86(20)
$\Phi^{obs}_{E,\,peak}$ ($\times 10^6 cm^{-2}$)	*44.62	*14.65	39.00673(50)	*129.57

Table B.3: Scaling factors that make us k_{DT} for the peak neutron fluence calculation for each of the different beam intensities for the nominal energy of 7.000 MeV

Beam Current (μA)	0.120	0.574	1.130	2.500
M20 count rate (counts s^{-1})	44.94(28)	185.46(52)	350.4(12)	770.0(13)
k_{MPA}	1.0039(48)	1.0164(48)	1.0309(15)	1.06758(58)
k_{PU}	1.0005(10)	1.0009(27)	1.0012(23)	1.0017(14)
Q (μC)	76.4313(87)	416.161(20)	312.430(56)	1273.38(11)
$\Phi^{obs}_{E,\,peak}$ ($\times 10^6 cm^{-2}$)	*4.810	23.5953(36)	13.7575(13)	48.266(12)

C. Digital Pulser Correction

To correct for the affects of the analogue pulser altering the HV, a digital pulser correction was applied matching the centroids of the pulser distributions. The correction factors k_p, the resultant centroid and FWHM values for the pulser distribution along with the uncorrected pulser centroid and FWHM values for the digital data sets are presented in table C.1.

Table C.1: The pulser centroid values along with the FWHM of the pulser distribution, before and after correction, k_p, is applied, for the digital neutron measurements.

$E^{calc}_{n,peak}$ (MeV)	Beam Current (μA)	k_p	Uncorrected (long int)		Corrected (long int)	
			Centroid	FWHM	Centroid	FWHM
1.20(4)	4.520	1.00(1)	3842(2)	203.8(2)	3842(2)	203.8(2)
2.50(3)	0.108	1.02(1)	3789(2)	220.6(3)	3865(2)	225.1(3)
	0.540	1.03(1)	3755(1)	206.6(2)	3867(2)	212.5(2)
	1.160	1.02(1)	3816(2)	219.9(2)	3892(2)	223.2(2)
	2.770	0.99(1)	3864(2)	222.9(3)	3864(2)	223.1(2)
5.00(7)	0.122	1.02(1)	3774(1)	203.6(1)	3850(1)	208(1)
	0.585	1.01(1)	3826(2)	196.0(1)	3826(2)	196.0(1)
	2.570	0.99(1)	3877(3)	202.3(1)	3876(3)	202.3(2)
	5.100	0.98(1)	3905(4)	205.1(2)	3827(4)	202.1(3)
7.00(4)	0.140	1.02(1)	3785(1)	202.7(2)	3861(2)	207(2)
	0.593	1.00(1)	3847(3)	199.0(1)	3847(3)	199.0(2)
	1.180	1.00(1)	3849(3)	205.7(2)	3849(3)	205.7(2)
	2.500	0.98(1)	3899(4)	207.6(3)	3821(4)	204.7(3)

D. Digital Varying Intensity

In order to compare measurements across intensities and energies the raw neutron spectra need to be scaled by a monitor value and corrected for pile up and dead time affects. The monitor chosen was the integrated charge value in order to express the final fluence values in neutrons cm^{-2} μC^{-1}. The correction factors and the scaling factors along with the raw calculated fluence value can be seen in table D.1.

Table D.1: Scaling factors for the peak neutron fluence calculation for each of the different beam intensities for the three different nominal energy of 2.5 MeV, 5.0 MeV and 7.0 MeV. *uncertainties provided by ICQU very small E-6

$E_{n,peak}^{calc}$ [MeV]	Beam Current [μA]	$E_{n,peak}^{meas}$ [MeV]	k_{PU}	k_S	Q [μC]	$\Phi_{\text{E, peak}}^{\text{obs}}$ [$\times 10^4 cm^{-2}$]
2.50(03)	0.108	2.589(65)	1.001(40)	1.0000(15)	126.007(11)	10.6310*
	0.540	2.582(63)	1.001(21)	1.0000(21)	336.603(18)	29.2264*
	1.160	2.602(64)	1.001(20)	1.0000(65)	301.773(17)	20.7164*
	2.770	2.580(63)	1.002(11)	1.5786(76)	1041.042(32)	41.6735*
5.00(07)	0.122	5.090(97)	1.002(43)	1.0000(15)	119.385(11)	5.1494*
	0.585	5.053(97)	1.001(37)	1.0000(27)	301.833(17)	12.8517*
	2.570	5.096(98)	1.002(13)	1.0000(36)	1025.865(32)	43.7675*
	5.100	5.054(97)	1.004(10)	1.5265(92)	1554.338(39)	39.5778*
7.00(04)	0.140	7.16(14)	1.002(36)	1.0000(30)	66.4788(82)	4.8182*
	0.593	7.10(13)	1.002(17)	1.0000(25)	331.364(18)	23.3505*
	1.180	7.14(13)	1.002(18)	1.333(10)	256.126(16)	13.3554*
	2.500	7.09(14)	1.004(11)	1.5579(95)	774.990(28)	19.9161*